Volume integral method for the electromagnetic modeling of self-powered current sensors.

Mayra Hernandez Alayeto

THÈSE

Pour obtenir le grade de

DOCTEUR DE L'UNIVERSITÉ GRENOBLE ALPES

École doctorale : EEATS - Electronique, Electrotechnique, Automatique, Traitement du Signal (EEATS)
Spécialité : Génie électrique
Unité de recherche : Laboratoire de Génie Electrique

Méthode intégrale de volume pour la modélisation électromagnétique des capteurs de courant autonomes

Volume integral method for the electromagnetic modeling of self-powered current sensors.

Présentée par :

Mayra HERNANDEZ ALAYETO

Direction de thèse :

Olivier CHADEBEC Responsable équipe MAGE du G2ELab, CNRS	Directeur de thèse
Gerard MEUNIER DIRECTEUR DE RECHERCHE EMERITE, Université Grenoble Alpes	Co-directeur de thèse
Jean-Michel GUICHON Université Grenoble Alpes	Co-encadrant de thèse
Loïc RONDOT INGENIEUR DOCTEUR, Schneider Electric	Co-encadrant de thèse
Matthieu FAVRE INGENIEUR, Schenider Electric	Co-encadrant de thèse

Thèse soutenue publiquement le **9 octobre 2023**, devant le jury composé de :

Olivier CHADEBEC DIRECTEUR DE RECHERCHE, CNRS DELEGATION ALPES	Directeur de thèse
Gerard MEUNIER DIRECTEUR DE RECHERCHE EMERITE, CNRS DELEGATION ALPES	Co-directeur de thèse
Loïc RONDOT INGENIEUR DOCTEUR, Schneider Electric	Examinateur
Christian VOLLAIRE PROFESSEUR DES UNIVERSITES, Ecole Centrale Lyon	Président
Hocine MENANA MAITRE DE CONFERENCES, Université de Lorraine	Examinateur
Edith CLAVEL PROFESSEURE DES UNIVERSITES, Université Grenoble Alpes	Examinatrice
Jean-René POIRIER MAITRE DE CONFERNENCES HDR, TOULOUSE INP	Rapporteur
Didier TRICHET PROFESSEUR DES UNIVERSITES, UNIVERSITE DE NANTES	Rapporteur

Invités :

Jean-Michel GUICHON
MAITRE DE CONFERENCES, Université Grenoble Alpes

Matthieu FAVRE
INGENIEUR, Schenider Electric

Contents

List of Figures

Acknowledgments

Ce travail a été réalisé dans le cadre d'une thèse CIFRE avec le laboratoire de Génie Électrique de Grenoble (G2Elab) et la société Schneider Electric.

Je tiens tout d'abord à remercier les membres du jury : M. Christian VOLLAIRE, professeur des universités au laboratoire Ampère à Lyon, pour m'avoir fait l'honneur de présider mon jury de thèse. M. Jean-René POIRIER, maitre de conférences au laboratoire Laplace et M. Didier TRICHET, professeur des universités à l'université polytechnique de Nantes, merci d'avoir accepté de rapporter cette thèse, de votre lecture attentive et vos commentaires qui ont aidé à l'amélioration de ce manuscrit de thèse. M. Hocine MENANA, maitre de conferences à l'université de Lorraine et Mme Edith CLAVEL, professeure des universités à l'université Grenoble Alpes, en tant qu'examinateur et examinatrice, merci pour toutes vos questions qui étaient très pertinentes et qui ont également contribué à ce manuscrit.

Je voudrais également exprimer ma profonde gratitude à mes cinq encadrants :

- Loïc RONDOT, ingénieur docteur à Schneider Electric, pour son investissement, sa grande didactique scientifique et toutes les conversations, magnétiques et non magnétiques.
- Gérard MEUNIER, directeur de recherche CNRS et professeur émérite de l'université Grenoble Alpes pour sa gentillesse en bienveillance, ainsi que pour m'avoir montré sa passion pour la modélisation électromagnétique.
- Olivier CHADEBEC, directeur de recherche CNRS, pour son apport scientifique et ces explications claires et didactiques.
- Matthieu FAVRE, ingénieur à Schneider Electric, pour sa disponibilité et son approche pragmatique qui m'a appris plein des choses.
- Jean-Michel GUICHON, maitre de conférences à l'université Grenoble Alpes, pour son expertise sur la plateforme MIPSE et ses remarques constructives.

Je souhaite également adresser mes remerciements à Sébastien Buffat, manager de l'équipe capteur de Schneider Electric, pour ses précieux commentaires tout au long de ma thèse et son temps, ainsi que Guillaume Briand pour son aide avec les essais et sa compétence pour prendre des photos, pour le meilleur et pour le pire.

Ensuite, j'aimerais remercier toute l'équipe capteur à Schneider Electric et les personnes autour, qui donnent de la bonne humeur au quotidien avec un esprit positif et pas du tout ironique: Bruno, Jean-Luc, Guillaume, Yvan, José, Cedric, Jiri, Bertrand, Eric, Sylvio, Juliette, Océane, Julien, Aminata et Raphael. Sans oublier Vincent qui a testé et amélioré ma patience pendant ces trois ans.

Et aussi, évidemment, à toute l'équipe au G2elab pour les pauses café et les conversations de tous les jours: Kouceila, Olivier, Antoine, Gauthier, Adrien, Quentin, Diego, Amir, Robin... Avec un grand merci à Bertrand pour son aide avec MIPSE, sa patience et son point de vue au quotidien qui me fait toujours réfléchir.

Je voudrais dédier cette thèse à mes parents Daniel et Rocio, qui m'ont toujours encouragé à faire des études et qui me donnent son support inconditionnel tous les jours, ainsi que mon frère Iván. Et finalement à mon compagnon, Nikunj, pour sa patience et sa bienveillance. Je m'estime très chanceuse de vous avoir à mes cotés.

General introduction

The evolution of the electric world is undergoing a rapid transformation as societies try to achieve a low-carbon strategy introducing green energy sources to lower the pollution. The shift towards a more sustainable and environmentally friendly electric sector is reshaping the way we power our lives. From the increasing adoption of renewable energy technologies such as solar and wind power to the advancement of electric vehicles, the electric world is experiencing a shift. This transition needs our adaptation to these changes, as we strive to build a cleaner and greener future.

In order to be efficient with this transformation, the need of quantifying the energy consumption of the different systems arises. To that aim, the use of measuring devices (sensors) that provide a complete idea of the electricity consumption of an electric installation is necessary.

Moreover, the necessity for our installations to be as compact as possible motivates us to create sensors that can address the mission of measurement and protection simultaneously. This is why measuring sensors are embedded in circuit breakers. Circuit breakers are in every building: houses, apartments, public buildings, factories... their aim is to protect people and goods in case of overcurrent. Their function is simple: interrupt the current flow when an overcurrent is perceived. Nevertheless, its conception is more complex.

Current sensors are crucial elements of circuit breakers. They provide current with two functionalities: obtain a measurement of the current and power other electronic components. Then, if a defect is found when measuring the current, the electronic components can analyse it and they can open the circuit, so that the current is stopped. These sensors are not easy to develop since the different functionalities impose diverse constraints, such as normative constraints (UL for the U.S. and IEC for Europe) or restrictions regarding the accuracy, the current or frequency range in which they should operate and the environment difficulties linked to humidity or temperature.

In order to reduce the conception time of a sensor or to optimize it once it has been marketed, the use of modeling and simulation tools is valuable. This thesis is focused in modeling current sensors of Schneider Electric that are part of circuit breakers. These sensors are composed of two parts: a current transformer to power the other components of the circuit breaker and a Rogowski metering coil to obtain an accurate measurement of

the current.

A first thought to model these sensor could be to use the classical finite element method. This method is able to accurately model the Rogowski metering coil alone. It is also able to model the current transformer isolated. Nevertheless, when both of them are placed together, the mesh needed to accurately represent the phenomena of the system has to be very thin, especially in the air region between the current transformer and the Rogowski metering coil. This happens due to the interference of the current transformer on the Rogowski metering coil, which can change its behaviour. A very thin mesh increases the computation time and memory used to solve the problem, which is not unlimited. In this case, a mesh thin enough to provide accurate results is not always possible, and the precision is compromised.

The Grenoble Electrical Engineering Laboratory (G2Elab) is specialised in the volume integral method, which is an alternative to the finite element method. Its main difference is the absence of a discretization in the air region, meshing only the active parts. This allows to avoid possible problems that arise when an extensive regions of air needs to be meshed.

This thesis is a collaboration of Schneider Electric and G2Elab to develop the volume integral method in order to model the mentioned current sensors. There are a total of four chapters:

- The first chapter introduces the context, dividing it in the industrial challenges, that is to say, the current sensors, and the modeling challenges, that explains the possible modeling tools, choosing the volume integral method.
- The second chapter describes the magnetostatic volume integral formulation developed by [1] which is the foundation of this thesis. A second part in this chapter explains the development that we have made to model thin air gaps within this formulation, given that many of the sensors treated contain thin air gaps and their effect on the sensor is not negligible. The formulation and the air gap model are validated with the current transformer of NSX sensor.
- The third chapter extends the magnetostatic volume integral formulation previously explained to a time-stepping formulation, taking into account the field-circuit coupling. This is done in two different ways: a weak coupling and a strong coupling. These formulations are also validated with the current transformer of NSX sensor.
- Finally, the fourth chapter is a real application case that gives value to the developed formulation. It considers a challenging sensor that has been developed by Schneider Electric, named MTZ sensor. In the previous years we have faced difficulties to have an accurate simulation model of this sensor when using the finite element method. The whole volume integral formulation developed in this thesis is applied to MTZ sensor to obtain precise and reliable simulations that provide extra information of it, corroborating its robustness.

Chapter I

Context: self powered current sensors

Summary

This chapter explains the context of this thesis: the modeling of self-powered current sensors. We first introduce them, explaining their functionality in circuit breakers. We provide an overview of the traditional current sensors to later focus on two of them: current transformers and Rogowski metering coils. Then, the need of models to simulate these sensors is explained, and some tools that can be used to model them are described, focusing on the volume integral method. Finally, the last section details the objectives of this thesis.

I.1 Introduction

Schneider electric is pioneer in the development of current sensors. These sensors are devices that allow to measure the current. They have a wide variety of applications: from detecting defaults in circuit breakers for the **protection** of people and goods to **measure** and **control** the load in building management systems to ensure network efficiency. They also foresee the maintenance of a device and supervise adequately a network that tends to become more complex when the multiplicity of energy sources increases.

In this chapter we explain the context of this thesis: modeling current sensors. To do that, a first part of industrial challenges introduces the functionality of current sensors, their classification and characteristics. Then, a second part with the modeling challenges describes the tools that can be used to model them, mentioning the finite element method and the volume integral method.

I.2 Industrial challenges

Current sensors can be divided into two categories regarding their functionality:

- **Metering sensors.** The main quality of these sensor is their high accuracy in measuring a quantity. The accuracy of a current sensor is certified by an accuracy class, which defines the maximum error that the device could have in a specified range of a given variable for some specific environmental conditions. For instance, regarding the current, class 1 for a reference current $I_b = 25$ A in a current range of 5 % of I_b to I_b means that the error can't be higher to 1 % for a current that is between 1.25 A (5 % of 25A) and 25 A. Data is obtained approximately every second to verify it. This can be extended to other global variables such as the root mean square value of the current or the voltage, the active power or the reactive power, among others. Apart from the accuracy, metering sensors are required to have a good immunity to external electromagnetic sources, meaning that they should not perceive external signals that could perturb their measuring.

- **Protection sensors.** The name of these sensors comes from their functionality: they are made to protect people and goods. They do it by detecting an overcurrent on the system, that could be either a short circuit or an overload. Their main quality is their rapidity to react when a malfunction is found, being able to obtain a measure in roughly a millisecond. They also have to be able to work in difficult climate conditions such as high temperature or high humidity. Furthermore, they are conceived self-powered, which complicates their design, given that this adds many constraints that will be mentioned later. Therefore, two concepts define these sensors: rapidity and self-power.

To have an idea of importance of these sensors on the market, Schneider Electric sells several hundreds of thousands metering sensors per year. Studying and understanding the phenomena behind these current sensors is crucial to be able to develop new sensors and to optimize the existing ones. The latter includes, for instance reducing their volume to

make them more compact or changing some components keeping the functionalities and reducing their cost.

Before diving into the sensors that we will address in this thesis, let us explain the different existing current sensors.

I.2.a The current measurement

In order to measure the current, there exist many sensor families depending on the physical principle used. The traditional current sensors are Rogowski coils, shunts and current transformers [2]. There are other types that obtain the current by measuring the magnetic field with magnetic sensors, such as magnetoresistive sensors, hall effect sensors or fluxgate [3], but they are not the interest of this thesis, therefore we will not get into further details. Let us explain the traditional ones.

I.2.a-i Rogowski sensors

Rogowski sensors are metering sensors for Alternating Current (AC) that provide high accuracy [4]. They play an important role in this thesis, which is why we will explain in detail the different types of Rogowski sensors, their requirements to be accurate and the different manufacturing options.
They consist of a primary conductor with a given current and a coil around it. Depending on their structure, two types of coils can be differentiated, classic and hybrid:

- Classic Rogowski coils are made exclusively of a coil of copper wire with helical shape. There are two ways of making them: the first one is the most simple one, and it consists of going from one point to almost the same point, covering the whole torus shape. The second one covers the form of the Rogowski twice: it first goes from the lead to the end and then it comes back from the end to the lead so that the start and the finish are placed at the same point, this is called counter-wound, Figure I.1, and it is more interesting to have a good immunity of the sensor. The main advantage of these sensors is that they are linear because there is no magnetic core, therefore they have a wide current range. In manufacturing terms, another advantage is that they have an open end that makes it flexible to wrap it around a conductor, which is practical for many applications. Their cost is low given that there is no magnetic material.

- Rogowski hybrid coils differ from classic Rogowki coils in the presence of magnetic material. They form a loop with magnetic sheets that are wedged with the coils (usually two coils and two magnetic parts, Figure I.2a). Their main advantage with respect to the classic ones is the compactness. The drawback of this design is that it is not linear given that the magnetic material can saturate. Moreover, the link between the magnetic sheets and the coils has to be done carefully, and often compensation turns have to be considered at the extremities of the coils to balance the gap between the coil and the magnetic sheet. Figure I.2b shows the Rogowski

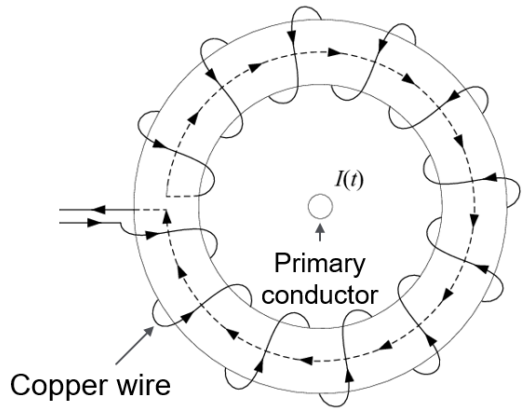

Figure I.1: Classic Rogowski sensor representation, image extracted from [7].

hybrid sensor PowerTag designed by Schneider Electric, formed by two magnetic sheets and two coils that have a shield.

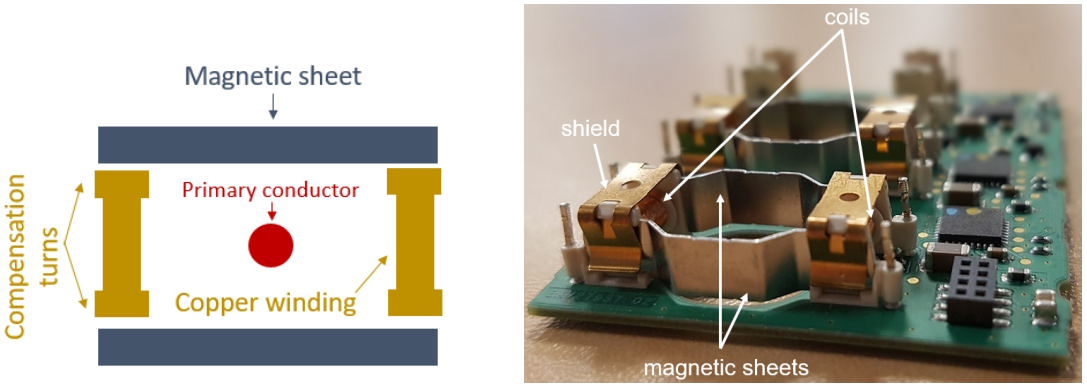

(a) General representation. (b) PowerTag.

Figure I.2: Rogowski hybrid sensors.

Often, Rogowski sensors are not placed alone, but inside a system with other components. The requirements for accurate and robust Rogowski sensors are the following:

- High gain. It is important to have high gain of the sensor to send the information perceived to the electronic components that will process it. If there is not enough gain, then they cannot analyse it. This can be achieved with an abundant number of turns forming the coil.

- Low crosstalk. The aim of Rogowski metering sensors is to measure the current perceived, but it is important to avoid signals that are out of the Rogowski, such as conductors that could be part of another components that are placed next to it. This is the reason why the hybrid sensor PowerTag (Figure I.2b) has a shielding around its coils. We say that the crosstalk is low when the external signals interfere the measuring of the Rogowski in less than 1 %.

- Low off-centre. A Rogowski sensor provides the current accurately if the primary conductor is placed at the centre of it. This is straightforward for classic Rogowski

coils with a circular shape, but it might not be that easy for hybrid Rogowski sensors that have a different topology, which is not always symmetric. Furthermore, when designing a sensor in a circuit breaker, there are other position constraints coming from different elements that might force a position of the primary conductor that is not centred. It is then important to ensure that the off-centre of the primary conductor doesn't change the measuring of the sensor. Ideally, the off-centre value obtained should be inferior to 1 %.

- Linearity. For the case of hybrid Rogowski sensors in which there is a magnetic material, it is essential to ensure a wide current range in which the material provides a linear response to avoid possible problems that come from the saturation.

To ensure the low crosstalk and off-centre it is crucial to have winding regularity [6]. This is fairly important when there are other elements around the Rogowski, because if there are more turns on one side than on the other, the imbalance might disturb other components as well as the sensor measurement. Winding regularity is simple in theory but it is not that easy when manufacturing a Rogowski coil with, for instance, 2000 turns (Figure I.3b), in which turns overlap and they might slide and change the position.

Now, regarding the manufacturing options, there are different alternatives:

- Only with a copper coil that is winded around a plastic piece. This is straightfoward when the coil follows a segment (I.3a) but it is not simple to do the winding when it follows a circular shape (Figure I.3b), because the machine used to create the winding needs to pass through the center to do the turns. Furthermore, the inner radius of the coil is different to the external radius, which might affect the tension or stress of the wire, as well as the square section of the coil.

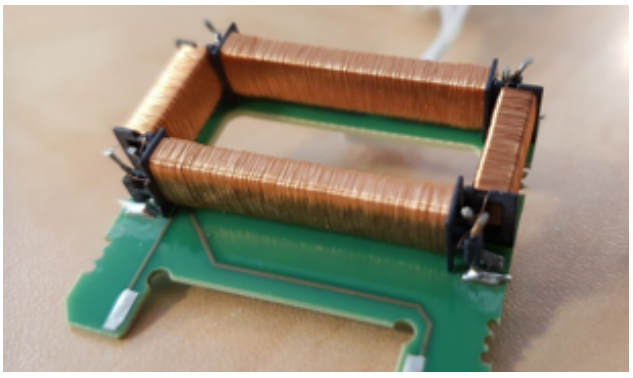

(a) Line classic Rogowski.

(b) Circular classic Rogowski.

Figure I.3: Copper coil manufacturing.

- A winding printed on a PCB, Figure I.4, which allows to measure the current with very few copper turns that are printed tracks on a PCB, being linear, simple an efficient.

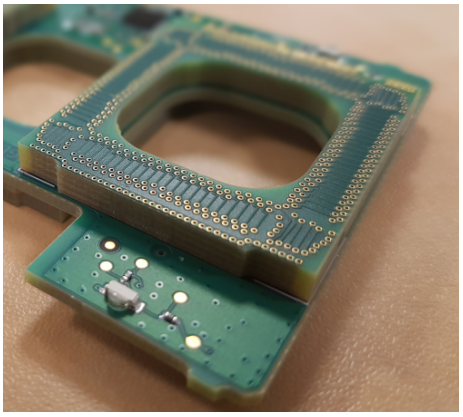

Figure I.4: Rogowski coil printed on PCB

- Plastronics or MID (Model Interconnect Device), which is a piece of plastic with an additive in which a laser traces tracks that are filled with copper, being this copper the winding of the Rogowski coil. This manufacturing option is still in development.

Finally, for any Rogowski sensor the current is computed following:

$$\mathrm{I}(t) = C \int e(t)\mathrm{d}t \tag{I.1}$$

where I is the current, $e(t)$ is the voltage produced by the coil and C is a constant that depends on the number of turns, the area of the smallest loop, the vacuum permeability and the length of the winding.

I.2.a-ii Shunt resistor sensors

Shunt resistor sensors are based on Ohm's law, where the voltage drop across the shunt is proportional to the current going through it. Therefore the current is computed following:

$$\mathrm{I}(t) = \frac{\mathrm{U}(t)}{R} \tag{I.2}$$

where R is the resistance and $\mathrm{U}(t)$ is the voltage.

The shunt resistor is chosen to have low resistance so that the circuit is barely affected (Figure I.5 shows a shunt resistor sensor for a circuit breaker, with a resistance of $5\mu\Omega$.), but enough to measure a voltage drop. Their simplicity makes them reliable and of low cost. They can be used for AC and Direct Currents (DC) applications.

I.2.a-iii Current transformer sensors

Current transformer sensors are based on the transformer principle, converting high primary current into lower secondary current [5]. It is composed of a primary winding (n_p turns), a secondary winding (n_s turns) and a magnetic core, Figure I.6. The core is often made of silicon steel, nickel iron or nanocrystalline and the windings are made of copper wire. Ideally, the current on the secondary winding (I_s) is proportional to the current

Figure I.5: Shunt resistor sensor.

imposed on the primary winding (I_p) on a wide current range, therefore I_s is computed following the equation:

$$I_p(t) = \frac{n_s}{n_p} I_s(t). \tag{I.3}$$

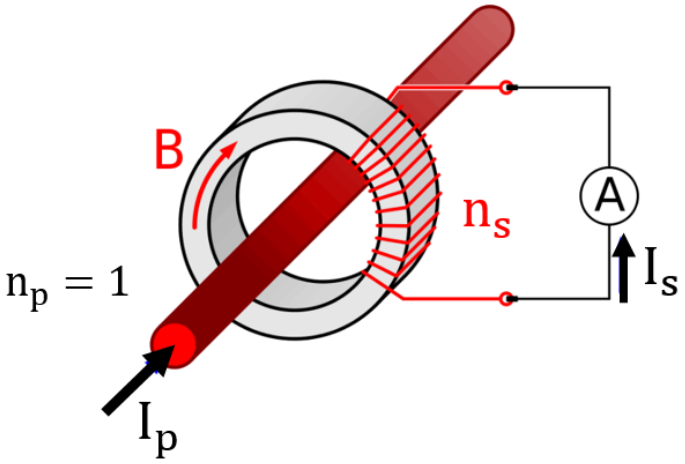

Figure I.6: Current transformer representation, extracted from [1].

Their main advantage is that they are not very sensitive to the off-centre of the primary coil and to the external fields that there could exist. Their main drawback occurs when the current is so high that it saturates the magnetic core, then the hysteresis phenomenon decreases its accuracy until the material is demagnetized. Furthermore, there are iron losses caused by eddy currents.

All the mentioned current sensors: Rogowski, shunt and current transformers need a source of power for the primary conductor, which can be either external or they can be self-powered with another sensor. Conventionally, to ensure the protection, the idea of an external power supply is not appreciated, being self-powered sensors the preferred option, which is the topic of the next section.

[1] https://en.wikipedia.org/wiki/Current_transformer

I.2.b Difficulties for self-powered sensors

In order to have an autonomous system, having a self-powered sensor is essential. This is very valuable when the application is related to protection, such as circuit breakers, where self-powered sensors provide an extra layer of security, which is corroborated by the international norm IEC 60947-2.
Self-powered sensors are sensors that don't require an external power supply. They are powered, for instance, by a current or voltage loop. In general, we refer to Current Transformers (CT), Figure I.7.

Figure I.7: Current transformer.

Let us notice that they differ from the measuring CT explained before in their functionality, for the latter the most important requirement is to ensure the relation $I_p n_p = I_s n_s$ for a wide current range to measure the current, whereas for self-powered CT the key is to avoid an external source of power and to provide energy to other components of the system. Therefore, the size and number of turns of the coils has to be carefully chosen to provide enough energy.

The two main difficulties arising in self-powered sensors are: supplying enough power to other components of the system and limiting the power carefully to avoid overloading the sensor, which could lead to burning the secondary coil.

Once we have seen the current sensors context, let us specify and explain more thoroughly the ones that we will address in this thesis.

I.2.c Current sensors of interest

In this thesis, we focus on current sensors that are embedded in a circuit breaker and have a double functionality: ensuring the protection with a fast measurement of the current; and a high accuracy metering function. We say that a measurement is fast when it is computed in less than a millisecond and that the accuracy is high when it has less than 1% of error. Furthermore, to go one step further in the protection, they have to be

self-powered. To this aim, we consider sensors that are composed of two parts: a **current transformer** (self-powered) and a **metering sensor of Rogowski type** (protection and metering) as Figure I.8 shows.

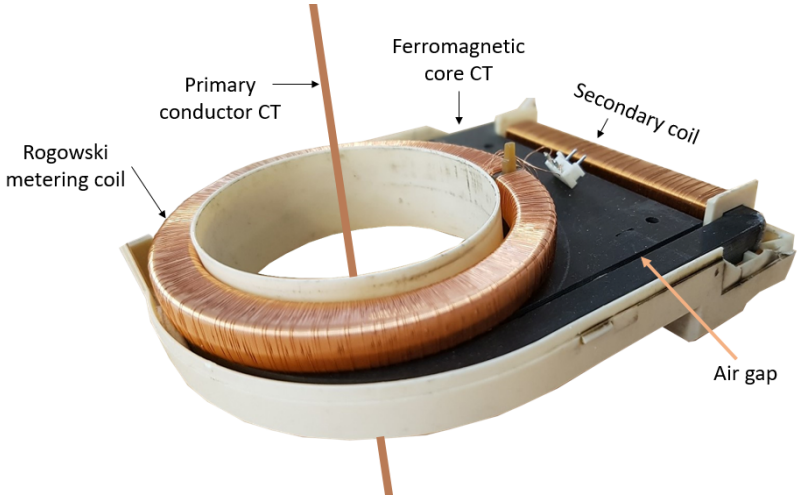

Figure I.8: Current sensor with composed of a CT and a metering coil.

In order to design these type of sensors, there are many features and difficulties to take into account:

- Obtain an accurate measurement of the current with the Rogowski coil, avoiding that the CT interferes in the measure, which is not simple because the Rogowski coil and the CT are placed next to each other.
- Provide enough power to other electronic components. This is done by the CT in different ways: increasing the section of the core to have more amount of electromagnetic material, considering more turns on the secondary coil or changing the core material to another one with higher permeability. It is important to have a fast response of the circuit breaker, because if the Rogowski coil detects fast an overcurrent but there is not enough power on the electronic components, the circuit breaker cannot open the circuit.
- Apart from ensuring enough power, the CT has to avoid overloading the electronic components, which would lead to burning them. This could be done increasing the volume of the secondary coil with a higher number of turns.
- Be able to mechanically conceive both CT and Rogowski together, taking into account other constraints of the device, for instance, the space available, that could be limited if there is a need of compactness.

An example of a Schneider Electric sensor with these characteristics is NSX (Figure I.9), where the current transformer and the Rogowski coil are assembled together. Let us get into further depth about this sensor. The ferromagnetic core is made of silicon steel sheets to reduce eddy currents. The Rogowski coil is made of copper and it has square shape, making a loop with four straight segments that are connected. This configuration

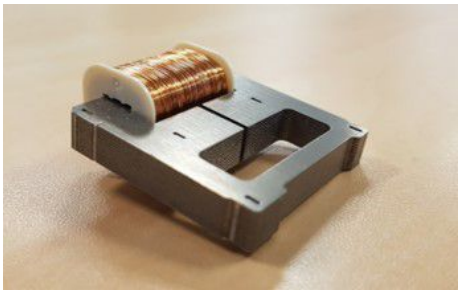

(a) Current transformer

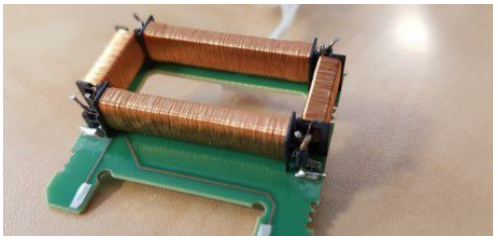

(b) Rogowski coil

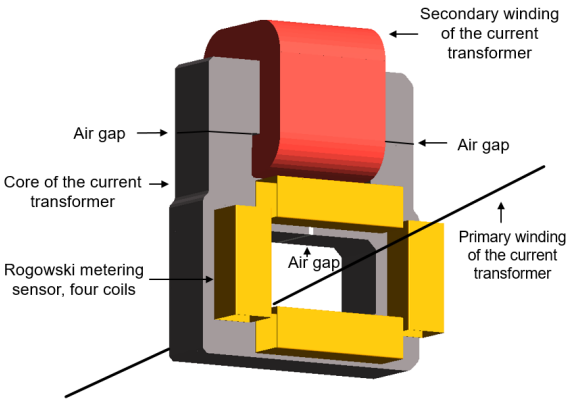

(c) Simulation model assembling both parts

Figure I.9: NSX sensor.

is not easy to manufacture because the winding machine has to keep the same tension on the wire all along the process and the squared shape of the section with right angles makes it hard to keep it homogeneous. The connection between the four segments is smoothed with some extra compensation turns on the ends of each segment. There are three air gaps in the ferromagnetic core: a large air gap that is created by design in the middle to force the magnetic flux to make a loop following the external border of the geometry and two other air gaps that are much thinner, which arise from welding two parts of the magnetic core in order to be able to introduce the secondary coil. This sensor will be used lately in chapter 2 and 3 to validate the developments of this thesis.

Electromagnetic modeling and simulation is a highly valuable tool that helps to understand how these sensors work and fully control the electromagnetic phenomena around them. This leads to the scientific challenges of the thesis that are not yet reached today with classic methods: realistic electromagnetic simulations of the sensors of Schneider Electric that are embedded in a circuit breaker.

I.3 Modeling challenges

Electromagnetic modeling and simulation is key to develop the desired sensors. There are three main advantages:

- It is easier to understand the phenomena because it allows to create a model, change

the parameters as needed and obtain a result in few minutes or hours to know the validity and limits of a feature.

- It helps to save time in the prototype phase of a product. Indeed, without a simulation model a new prototype has to be created each time a feature has to be tested. Simulation helps to obtain results of the feature reducing the number of prototypes, which accelerates the design and reduces the cost.

- It allows to have a model that can help to optimize the sensor once it is released, for instance simplifying its geometry, changing a material to another one with different properties, making it more compact or reducing its cost.

Nowadays, there are many electromagnetic simulation software that provide the tools to model and simulate low frequency electromagnetic devices, sensors included: Altair Flux, Ansys Maxwell or COMSOL among others. Most of these are based on the well-known finite element method.

I.3.a The traditional method and its weakness

The most popular method to solve low frequency electromagnetic problems is the **Finite Element Method** (FEM). It allows to solve partial differential equations (such as Maxwell's equations) by subdividing the space of study into smaller parts called finite elements.

This method was introduced in the 1940s [8] [9] and it has been largely studied by the scientific and engineering community in order to develop accurate formulations and optimize calculations. It has many advantages:

- It allows to solve numerous types of electromagnetic problems: electrostatic, magnetostatic, quasi-static and coupled circuit-field among others.

- Any type of material can be considered: homogeneous and non homogeneous, isotropic and anisotropic, linear and nonlinear materials.

- The matrices arising from FEM are sparse: the interaction between the elements is given for those that are close to each other but not for those that are far.

In general, it is an efficient method to solve Maxwell's equations and it provides accurate results. Nevertheless, for some specific cases there are some limitations, for example, for the computation of magnetic flux through coils that are placed in the air. This limitation is linked to the mesh of the problem. The FEM needs a mesh of the active region of study (magnetic, conductor, dielectric...) and the air around to capture the electromagnetic behaviour in the air that might impact the rest of the domain. For instance, in the case of the described sensors there is a need of accuracy on the air elements next to the metering coil where the magnetic flux is computed, then the mesh has to be refined to increase the number of elements and it has to be adapted to the shape of the coil, which is not always feasible. But as the number of mesh elements increases, so does the matrix describing the problem, which raises the computational load.

This mesh limitation in the air region complicates the computation of the magnetic flux through metering coils of the sensors previously explained, composed of a current transformer and a Rogowski metering coil. As a matter of fact, the FEM can accurately model the current transformer alone, or the Rogowski metering coil alone. Nevertheless, when they are together separated by a low distance, a very thin mesh is needed to capture the effect of the current transformer on the Rogowski metering coil, which creates a large number of unknowns in the system describing the problem. This becomes too expensive computationally, and the accuracy is compromised.

In order to solve the mesh limitation given to obtain accurate results of the magnetic flux through coils that are in the air, which endangers the accuracy of our metering sensors, we propose the use of the volume integral method.

I.3.b The alternative method and its strength

An alternative to the FEM is the use of the **Volume Integral Method** (VIM). It is part of integral methods, which only need to mesh the active regions, avoiding to mesh the air around them and providing in general accurate results with a coarse mesh. The accuracy of this method is very competitive when the volume of the air involved in the problem is high compared to the volume of the active region.

Integral methods appeared in the 1970s with the Magnetic Moment Method (MMM), which is based on uniform magnetization on each element, formalized by Harrington [10] and tested on academic codes such as GFUN [11] or RADIA [12]. There are other integral methods, such as the boundary element method (BEM), which is limited to linear materials, for instance for electrostatic problems [13]. Another integral method is the Partial Element Equivalent Circuit (PEEC) for the magnetoharmonic case, which takes into account capacitive or even propagative effects [14].
These methods are appealing in terms of accuracy given the huge reduction of unknowns: only the active domains are meshed, meaning volume elements for MMM and PEEC and surface elements for BEM.

The main drawback is that the matrices arising from these methods are fully populated because, contrary to the FEM in which the matrices only take into account the interaction between two elements that are next to each other, in the VIM all the interactions between elements are considered. This translates in complexity $O(n^2)$ for matrix operations such as products and in intensive memory RAM storage on the computer. Another difficulty is the presence of singular Green kernels in the matrix system terms arising from the problem, for which integration strategies have to be adopted.

Those are the reasons why integral methods weren't widely employed until last decade, when two main improvements changed their popularity:

1. Matrix compression algorithms to deal with fully populated matrices. For instance, Fast Multipole Method (FMM) [15] or Hierarchical matrices (H-matrices) such as Adaptive Cross Approximation (ACA) [16] or Hybrid Cross Approximation (HCA)

[18]. They reduce the matrix complexity of matrix-vector products from $O(n^2)$ to $O(nlogn)$, shortening efficiently the computation time and reducing the RAM memory space needed.

2. Advanced integral formulations, either H-conforming based, for instance, on the magnetic scalar potential [19, 20] or B-conforming based on the magnetic induction [1].

In this thesis we focus on the volume integral method because only the active regions have to be discretized, avoiding to mesh the air and for its accuracy as well as its versatility for nonlinear materials. It will provide precision in the computation of the magnetic flux through coils that are surrounded by air, as it is the case of Rogowski metering coils.

The scientific challenge consists in proving that the desired sensors can be modeled using the volume integral method while obtaining high accuracy in the calculation of the magnetic flux through in the air (metering coils). To achieve this, the model needs to keep a good description of the nonlinear behaviour of the material, the field-circuit coupling and the self-powered functionality.

Within the VIM there could be many different formulations, depending on the physical quantity that is approximated on the mesh elements: B-conforming or H-conforming; and depending on the shape functions used: edge or facet base functions. We choose a B-conforming formulation because these type of formulation usually have a better convergence rate than H-conforming ones for nonlinear problems [24]. Facet based functions will be considered following the encouraging results of the thesis of Vinh Le-Van [21].

The new developments are built over MIPSE library, which is the acronym of *Modeling of Interconnected Power SystEms*. It is created and developed at G2Elab and it is used for numerical simulation dedicated to electromagnetism of low and medium frequency.

I.4 Objectives of the thesis

The objective of this thesis is to develop a simulation tool that allows to **model the current sensors** previously shown in section I.2.c, composed of a current transformer and a Rogowski metering sensor, and consequently have the full simulation description. These sensors have to be accurate and self-powered. We need this tool to provide accuracy in the computation of the magnetic flux through metering coils that are in the air and to be robust with the rest of the elements: nonlinear behaviour, field-circuit coupling and self-powered aspect.

We aim at developing the tool using the **volume integral method**, given that it is a good candidate to obtain accuracy in the computation of the flux through metering coils. Nevertheless, we also have to make sure that we can use the volume integral method for the other requirements of the sensor that ensure the protection and the self-power function. In this thesis, we focus on the following aspects:

- First, create a basis model, which is a magnetostatic case for linear and nonlinear materials.
- Then, take into account thin air gaps, because they arise in almost every sensor, particularly when two ferromagnetic materials are welded, and they affect the current transformer. Thin air gaps are not easy to model because a very thin mesh is needed to accurately perceive its effect. We will propose an alternative to this that does not need to mesh the air gap as a volume element but as a surface element with a numerical treatment.
- Obtain an accurate computation of the magnetic flux through coils that are in the air to ensure that the metering coil makes its function correctly.
- Finally, in order to have a more realistic model, we will describe the extension of the magnetostatic case to a time stepping (transient) field-circuit coupled formulation incorporating the previous features: the presence of thin air gaps and nonlinear materials.

Chapter II

Volume integral method for nonlinear magnetostatic problems

Summary

This chapter has two parts, the first one details a magnetostatic volume integral formulation used to simulate current sensors. This formulation is B-conforming and it is based on the discretization of the induction in facet-shape functions and a Galerkin projection. The second part develops a method to model thin air gaps withing the previously explained formulations. The thin air gaps are treated as surface regions with a numerical treatment instead of volume regions. The validation of both parts is done with NSX current sensor.

II.1 Introduction

In order to develop new sensors and to improve them, electromagnetic modeling and simulation are particularly useful tools. Electromagnetism phenomena are understood through Maxwell's equations, therefore a library that solves these partial differential equations is needed. In this chapter we will consider the magnetostatic case, meaning that there is no time variable on the equations and there is no circuit coupling.

The magnetostatic volume integral formulation for nonlinear problems, B-conforming and based on facet functions as in [1] will be explained, having special emphasis in how the magnetic flux through coils is computed. An application to NSX sensor (Fig. I.9) comparing it with another simulation software is then shown. The aim of this formulation is to be practical for devices such as current sensors, and a frequent feature appearing in this devices is the presence of air gaps, therefore the second part of this chapter will be focused on the development of an air gap model using the previous formulation. It will also be applied to an academic case and NSX sensor.

II.2 VIM formulation

Let us consider a problem formed by a ferromagnetic non conductive region Ω_m defined by a magnetic permeability $\mu(\mathbf{H})$, source regions Ω_c associated to current densities $\mathbf{j}_\mathrm{c}$ such as conductor coils and the air encompassing the previous regions as Fig. II.1 shows. Before explaining the volume integral formulation, let us introduce Maxwell's equations.

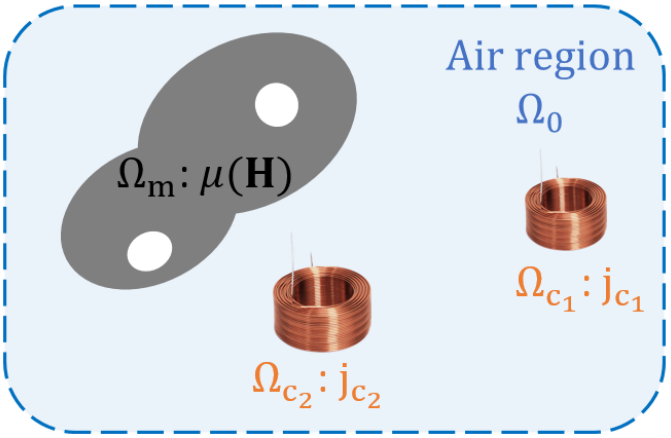

Figure II.1: General magnetostatic problem.

II.2.a Maxwell's equations for magnetostatic problems and constitutive law

Maxwell's equations are the foundation of electromagnetism, they were published in 1861. The macroscopic equations in continuous, local form under magnetostatic assumptions are the following:

– Gauss's law for magnetism:

$$\nabla \cdot \mathbf{B} = 0 \tag{II.1}$$

– Ampere's law:

$$\nabla \times \mathbf{H} = \mathbf{j}_c \tag{II.2}$$

where $\mathbf{B}$ is the magnetic flux density (T), $\mathbf{H}$ is the magnetic field strength (A/m) and $\mathbf{j}_c$ is the electric current density (A/m^2).
$\mathbf{B}$ and $\mathbf{H}$ are linked by the constitutive equation. Without considering permanent magnetization (no magnetic coercivity) and for isotropic materials, their relation is given by:

$$\mathbf{B} = \mu(\mathbf{H})\mathbf{H} \tag{II.3}$$

where $\mu(\mathbf{H})$ is expressed in H/m and $\mu(\mathbf{H}) = \mu_0\mu_r(\mathbf{H})$, being μ_0 the vacuum permeability and μ_r the relative permeability that is specific to each material. It can also be expressed as:

$$\mathbf{H} = \nu(\mathbf{B})\mathbf{B} \tag{II.4}$$

where $\nu(\mathbf{B})$ is the inverse of the permeability.
The magnetization $\mathbf{M}$ (A/m) is defined as $\mathbf{B} = \mu_0(\mathbf{H} + \mathbf{M})$, therefore:

$$\mathbf{M} = (\nu_0 - \nu(\mathbf{B}))\mathbf{B} \tag{II.5}$$

where ν_0 is the inverse of the vacuum permeability, also called reluctivity.

We aim at solving the system of equations formed by eq. (II.1) and eq. (II.2) using the constitutive equation. We will then obtain the value of $\mathbf{B}$ that will allow to compute other global values such as the magnetic flux through coils.

II.2.b Magnetostatic VIM formulation

$\mathbf{H}$ can be decomposed by the sum of two terms, the source field $\mathbf{H_0}$ created by source currents and the reduced field $\mathbf{H_r}$ created by the ferromagnetic materials:

$$\mathbf{H} = \mathbf{H_0} + \mathbf{H_r}. \tag{II.6}$$

The source field verifies $\nabla \times \mathbf{H_0} = \mathbf{j}$, therefore given Ampere's law, eq. (II.2), $\nabla \times \mathbf{H_r} = \mathbf{0}$. Then, a reduced magnetic scalar potential φ_r can be written as:

$$\mathbf{H_r} = -\nabla\varphi_\mathbf{r} \tag{II.7}$$

where

$$\varphi_r = \frac{1}{4\pi}\int_\Omega \mathbf{M} \cdot \nabla(\frac{1}{r})\mathrm{d}\Omega \tag{II.8}$$

and r is the distance between the integration point and the observation point. Applying this expression of $\mathbf{H_r}$ on eq. (II.6) we obtain:

$$\mathbf{H} = \mathbf{H_0} - \nabla\varphi_\mathbf{r}. \tag{II.9}$$

Now, using the definition of the reduced magnetic scalar potential:

$$\mathbf{H} = \mathbf{H_0} - \nabla \left(\frac{\mathbf{1}}{\mathbf{4}\pi} \int_{\mathbf{\Omega}} \mathbf{M} \cdot \nabla(\frac{\mathbf{1}}{r}) \mathrm{d}\mathbf{\Omega} \right). \tag{II.10}$$

This is the basis equation of the reasoning. Let us explain the formulation choice to continue.

II.2.c Formulation choice

Equation (II.10) is the basis equation of many integral formulations. For instance, defining the magnetization, a formulation of the magnetic moment method can be developed [23]. There are also two other types of formulations, H-conforming and B-conforming:

- H-conforming formulations verify strongly Ampere's law, eq. (II.2), and weakly Gauss's law for electromagnetism, eq. (II.1). They are widely studied in the literature and they can be based on the interpolation of $\mathbf{H}$ [26], the reduced magnetic scalar potential φ_r or the total magnetic scalar potential φ [27, 28]. Let us note that the reduced potential will experience a connexity problem for simply connected domains that is usually solved with a magnetic cut.

- B-conforming formulations verify strongly Gauss's law, eq. (II.1), and weakly Ampere's law, eq. (II.2) and they are less studied in the literature. They can be based on the interpolation of induction $\mathbf{B}$ [1] or the magnetic vector potential $\mathbf{A}$ [21, 22], such that $\mathbf{B} = \nabla \times \mathbf{A}$.

For this thesis, we choose a B-conforming formulation based on induction $\mathbf{B}$ using facet shape functions. The main reason for this is that at G2Elab we have already worked with this type of formulation and we have more experience with it. Another reason is that the convergence for nonlinear problems is usually better for B-conforming formulations than for H-conforming ones [24].
In this chapter the formulation for the magnetostatic case as it has been developed in [1] will be explained, and as a second stage, in chapter 3, we will show that this formulation can be extended to the transient case, taking into account the field-circuit coupling.

Let us explain the facet-shape functions before getting into the development of the formulation.

II.2.c-i Facet-shape functions

Facet-shape functions are key in the development of the formulation because they will be used to create an interpolation of induction $\mathbf{B}$ and to apply a Galerkin projection. It is then important to fully understand these functions and their properties, which are distinctive of the formulation.

To introduce facet-shape functions, let us consider a tetrahedron which is part of the mesh of a domain, with vertices v_1, v_2, v_3 and v_4, let x a point belonging to the tetrahedron, then for each vertex v_1, v_2, v_3 and v_4 there is a nodal function $\lambda_{v_i}(x)$ that designates the

weight of the barycenter of x in the tetrahedron, with value 1 at the corresponding vertex v_i and zero at the other vertices. λ_{v_i} is then a continuous piece-wise function verifying:

$$\begin{cases} x = \sum_i \lambda_{v_i}(x) x_i \\ \sum_i \lambda_{v_i} = 1 \end{cases} \tag{II.11}$$

Now, let us focus on the facet formed by vertices v_1, v_2 and v_3 that we call f, its facet-shape function w_f (or Whitney 2-form [34] function) is defined by:

$$\mathrm{w}_f = 2(\lambda_{v_1}\nabla\lambda_{v_2} \times \nabla\lambda_{v_3} + \lambda_{v_2}\nabla\lambda_{v_3} \times \nabla\lambda_{v_1} + \lambda_{v_3}\nabla\lambda_{v_1} \times \nabla\lambda_{v_2}). \tag{II.12}$$

In general, facet-shape functions $\mathbf{w}_j$ verify two properties:

$$\mathbf{w}_j \cdot \mathbf{n}_j = \pm\frac{1}{S_j} \tag{II.13}$$

$$\nabla \cdot \mathbf{w}_j = \pm\frac{1}{V_{E_j}}, \tag{II.14}$$

where $\boldsymbol{n}_j$ is the normal vector to the surface of facet j, S_j is the surface of facet j and V_{E_j} is the volume of element E in which facet j is placed. The sign is defined with the orientation of the normal vector, which can be incoming or outgoing. We define this orientation depending on the position of the facet:

- For external facets, the normal vector has positive orientation if the normal vector is outgoing.
- For internal facets, the normal vector has positive orientation if it goes from the volume element with lower index to the volume element with higher index, given that all volume elements have an index number assigned.

For instance, for two elements such as the ones represented in Figure II.2, the normal on the external facet i of element E_2 (Fig. II.2a) is positive because it is outgoing, therefore:

$$(\mathbf{w}_i \cdot \boldsymbol{n}_i)|_{E_2} = +\frac{1}{S_i} \qquad (\nabla \cdot \mathbf{w}_i)|_{E_2} = +\frac{1}{V_{E_2}}.$$

The normal represented on the internal facet j that is shared with the two elements is positive for the shared facet belonging to E_1 and negative for the share facet belonging to E_2, hence:

$$(\mathbf{w}_j \cdot \boldsymbol{n}_j)|_{E_1} = +\frac{1}{S_j} \qquad (\nabla \cdot \mathbf{w}_j)|_{E_1} = +\frac{1}{V_{E_1}}.$$

$$(\mathbf{w}_j \cdot \boldsymbol{n}_j)|_{E_2} = -\frac{1}{S_j} \qquad (\nabla \cdot \mathbf{w}_j)|_{E_2} = -\frac{1}{V_{E_2}}.$$

As a remark, it is important to note that for a given mesh element, for instance a tetrahedron, for a chosen facet i with facet-shape function $\mathbf{w}_i$, Figure II.3, as mentioned before $\mathbf{w}_i \cdot \boldsymbol{n}_i = \frac{1}{S_i}$ for facet i, but for the normal vector of the three remaining facets j of the tetrahedron $\mathbf{w}_i \cdot \boldsymbol{n}_j = 0$.

Let us notice that each facet shape function $\mathbf{w}_j$ is defined piecewise on each facet element.

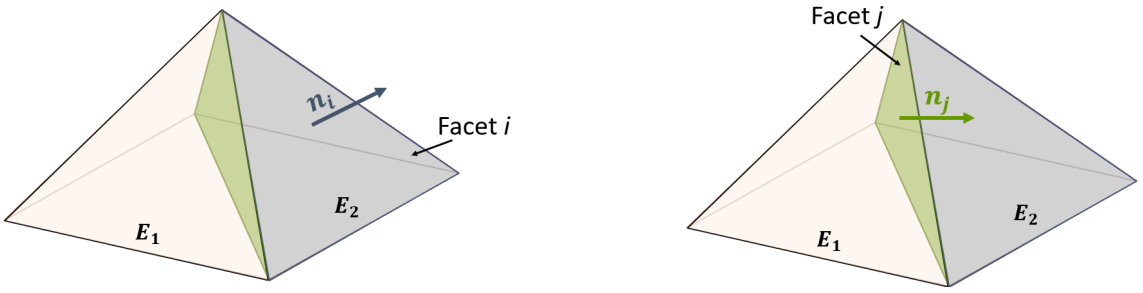

(a) External facet. (b) Internal facet.

Figure II.2: Facets representation.

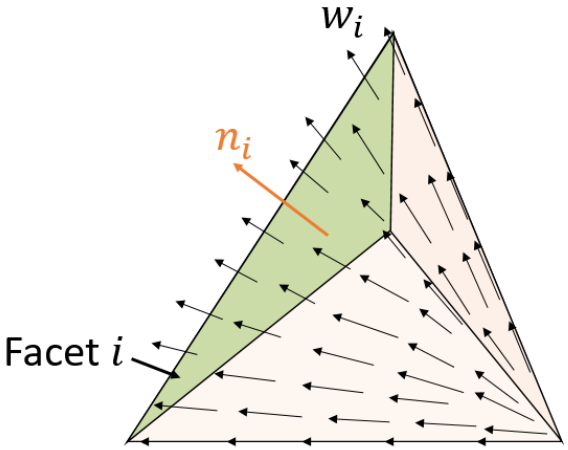

Figure II.3: w_i facet-shape function representation of a tetrahedron.

II.2.c-ii Discretization and interpolation

Once the facet shape functions have been introduced, let us create a discretization of the ferromagnetic domain Ω_m with boundary Γ subdividing it into volume elements, we call it primal mesh. Let N_f be the number of facet elements of the mesh.

An interpolation of the magnetic induction $\mathbf{B}$ with facet elements is made such that:

$$\mathbf{B} = \sum_{j=1}^{N_f} \mathbf{w}_j \Phi_j \tag{II.15}$$

where $\mathbf{w}_j$ are facet-shape functions of the primal mesh and Φ_j is the magnetic flux across facet j. This interpolation ensures the continuity of magnetic flux between two adjacent elements. Let us remark that the unknown of the matrix system that we will create to define the problem will be Φ_j, the flux crossing each facet.

II.2.c-iii Galerkin projection and internal system

Coming back to the basis equation (II.9), the constitutive equation is applied to obtain:

$$\nu(\mathbf{B})\mathbf{B} = \mathbf{H_0} - \nabla\varphi_\mathbf{r}. \tag{II.16}$$

Then, the Galerkin method is used to project it on the magnetic region using as test functions the same facet-shape functions $\mathbf{w}_i$ employed for the interpolation of induction $\mathbf{B}$, obtaining

$$\int_{\Omega_\mathrm{m}} \mathbf{w}_i \cdot \nu(\mathbf{B})\mathbf{B}\mathrm{d}\Omega_\mathrm{m} = \int_{\Omega_\mathrm{m}} \mathbf{w}_i \cdot \mathbf{H_0}\mathrm{d}\Omega_\mathrm{m} - \int_{\Omega_\mathrm{m}} \mathbf{w}_i \cdot \nabla\varphi_r \mathrm{d}\Omega_\mathrm{m}. \tag{II.17}$$

This procedure allows to project on tests functions instead of a more simple collocation method that projects on points, which has shown more accuracy [35]. Let us analyse the last term more in detail. Using the divergence theorem and the properties of facet-shape functions we have:

$$\int_{\Omega_\mathrm{m}} \mathbf{w}_i \cdot \nabla\varphi_r \mathrm{d}\Omega_\mathrm{m} = \int_{\Gamma_i} \varphi_r \mathbf{w}_i \cdot \mathbf{n}\mathrm{d}\Gamma_i - \int_{\Omega_\mathrm{m}} \varphi_r \nabla \cdot \mathbf{w}_i \mathrm{d}\Omega_\mathrm{m}. \tag{II.18}$$

Now, we can differentiate two cases, depending on the position of facet i:

1. **If facet i is in the interior** of the domain Ω_m the surface integral vanishes given that the facet is shared by two volume elements E_j and E_k with $j < k$ and the normal vector of the two elements has opposite sign. Hence, we write:

$$\int_{\Omega_\mathrm{m}} \mathbf{w}_i \cdot \nabla\varphi_r \mathrm{d}\Omega_\mathrm{m} = \int_{\Omega_{E_k}} \varphi_r \nabla \cdot \mathbf{w}_i \mathrm{d}\Omega_{E_k} - \int_{\Omega_{E_j}} \varphi_r \nabla \cdot \mathbf{w}_i \mathrm{d}\Omega_{E_j} \tag{II.19}$$

   where Ω_{E_j} is the volume element E_j that is in the ferromagnetic region Ω_m. Using the property of facet functions (II.14), the previous expression can be written as:

$$\int_{\Omega_\mathrm{m}} \mathbf{w}_i \cdot \nabla\varphi_r \mathrm{d}\Omega_\mathrm{m} = \frac{1}{V_{E_k}} \int_{\Omega_{E_k}} \varphi_r \mathrm{d}\Omega_{E_k} - \frac{1}{V_{E_j}} \int_{\Omega_{E_j}} \varphi_r \mathrm{d}\Omega_{E_j}. \tag{II.20}$$

   We notice that $\frac{1}{V_{E_k}} \int_{\Omega_{E_k}} \varphi_r \mathrm{d}\Omega_{E_k}$ represents the average reduced scalar potential of element E_k, that we denote as $\overline{\varphi}_{r_{E_k}}$, thus:

$$\int_{\Omega_m} \mathbf{w}_i \cdot \nabla\varphi_r \mathrm{d}\Omega_\mathrm{m} = \overline{\varphi}_{r_{E_k}} - \overline{\varphi}_{r_{E_j}} = \Delta\overline{\varphi}_{r_{int_i}} \tag{II.21}$$

   where subscript int_i means that the facet i belongs to the interior of the domain Ω_m. Then, $\Delta\overline{\varphi}_{r_{int_i}}$ represents the difference of the average reduced scalar potential of two volume elements that share facet i, which is in the interior of the domain.

2. **If facet i is a boundary facet** that belongs to volume element E_j, meaning that it is on the boundary of Ω_m, the surface integral doesn't vanish. Using the two facet properties (II.13) and (II.14) we write:

$$\int_{\Omega_\mathrm{m}} \mathbf{w}_i \cdot \nabla\varphi_r \mathrm{d}\Omega_\mathrm{m} = \frac{1}{S_i} \int_{\Gamma_i} \varphi_\mathrm{r} \mathrm{d}\Gamma_i - \frac{1}{V_{E_j}} \int_{\Omega_{E_j}} \varphi_\mathrm{r} \mathrm{d}\Omega_{E_j} = \overline{\varphi}_{r_{\Gamma_i}} - \overline{\varphi}_{r_{E_j}} = \Delta\overline{\varphi}_{r_{b_i}} \tag{II.22}$$

   where $\overline{\varphi}_{r_i}$ is the average reduced scalar potential of facet i and subscript b_i means that the facet i is at the boundary of the ferromagnetic region. Then, $\Delta\overline{\varphi}_{r_{b_i}}$ represents the difference of the average reduced scalar potential between the boundary facet i and the volume element to which facet i belongs.

After considering the two possible facet positions, the last term of eq. (II.17) can be expressed as:

$$\int_{\Omega_\mathrm{m}} \mathbf{w}_i \cdot \nabla\varphi_r \mathrm{d}\Omega_\mathrm{m} = \begin{cases} \Delta\overline{\varphi}_{r_{int_i}} & \text{if } i \in \Omega_\mathrm{m} \\ \Delta\overline{\varphi}_{r_{b_i}} & \text{if } i \in \Gamma. \end{cases} \tag{II.23}$$

Let us now take into account all the terms of eq. (II.17). Considering the interpolation of $\mathbf{B}$ on it and eq. (II.23) on the left hand side, we can write (II.17) in the following matrix form:

$$\mathbf{R_m}\Phi + \begin{pmatrix} \Delta\overline{\varphi}_{r_{int_i}} \\ \Delta\overline{\varphi}_{r_{b_i}} \end{pmatrix} = \mathbf{U}^{\mathrm{H}_0} \tag{II.24}$$

where Φ is the vector containing the magnetic flux through facets, $\mathbf{R}$ is a finite element matrix defined as

$$\mathrm{R_m}_{ij} = \int_{\Omega_\mathrm{m}} \mathbf{w}_i \cdot \nu(\mathbf{B}) \mathbf{w}_j \mathrm{d}\Omega_\mathrm{m} \tag{II.25}$$

$i = 1, 2, ..., N_f$, $j = 1, 2, ..., N_f$ and $\mathbf{U}^{\mathrm{H}_0}$ is a vector coming from the source term

$$\mathbf{U}^{\mathrm{H}_0} = \int_{\Omega_\mathrm{m}} \mathbf{w}_i \cdot \mathbf{H_0} \mathrm{d}\Omega_\mathrm{m} \tag{II.26}$$

$i = 1, 2, ..., N_f$. The system (II.24) shows the interactions given in the ferromagnetic region and within its boundary without taking into account the air, we call it the internal system.

II.2.c-iv Equivalent electric circuit approach and external system

Let us consider an equivalent electric circuit approach creating a dual mesh of the primal one previously explained. Then, as Fig. II.4 shows:

- The branches of the dual mesh are the facets of the primal mesh.
- The nodes of the dual mesh are the elements of the primal mesh.

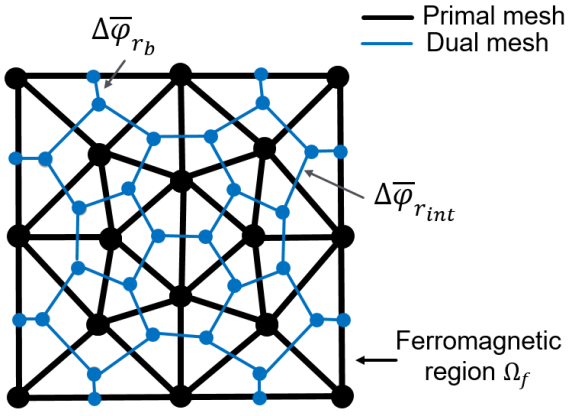

Figure II.4: Primal and dual mesh representation of a square domain in 2D.

With the equivalent circuit approach, the internal system (II.24) can be seen differently, being $\mathbf{R}$ an internal reluctance matrix for the magnetic material, $\Delta\overline{\varphi}_{r_{int_i}}$ and $\Delta\overline{\varphi}_{r_{b_i}}$ potential differences and $\mathbf{U}^{\mathrm{H}_0}$ a source term. We notice that the unknowns of the system, Φ_j that we defined previously as the magnetic flux across facet j correspond to the flux on the branches of the dual mesh.

The final step is to take into account the contribution in the air region. Instead of meshing the air, a common agreement in integral methods is to consider an outer node called infinity node in which we set a null magnetic scalar potential. This infinity node is linked to the border elements Γ of the ferromagnetic region.

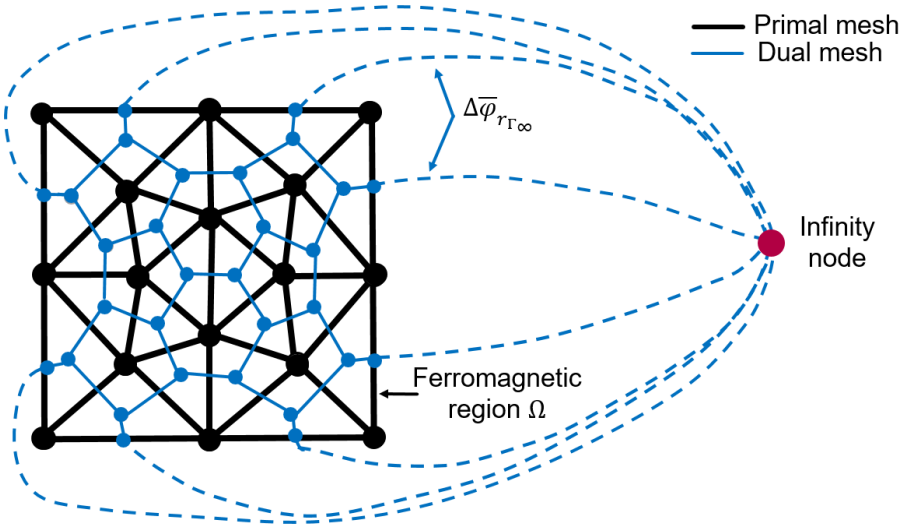

Figure II.5: Primal and dual mesh representation of a square domain in 2D with the infinity node.

Given that the average reduced scalar potential at the infinity node is null, the difference of the average reduced scalar potential between a boundary facet i and the infinity node writes:

$$\Delta\overline{\varphi}_{r_{\Gamma_i\infty}} = \overline{\varphi}_{r_{\Gamma_i}} - \overline{\varphi}_{\infty} = \int_{\Gamma_i} \frac{\varphi_r}{S_i} \mathrm{d}\Gamma_i. \tag{II.27}$$

Using (II.5) and eq. (II.8), φ_r can be expressed as

$$\varphi_r = \sum_{\Omega_E \in \Omega} \frac{1}{4\pi} \int_{\Omega_E} (\nu_0 - \nu_E(\mathbf{B}))\mathbf{B} \cdot \nabla \left(\frac{1}{r}\right) \mathrm{d}\Omega_E, \tag{II.28}$$

where Ω_E is each of the mesh volume elements. Now, injecting the expression of φ_r in eq.(II.27) and assuming a constant reluctance per element we have:

$$\Delta\overline{\varphi}_{r_{\Gamma_i\infty}} = -\frac{1}{4\pi} \int_{\Gamma_i} \frac{1}{S_i} \left[\sum_{\Omega_E \in \Omega_\mathrm{m}} \delta\nu_j \int_{\Omega_E} \mathbf{B} \cdot \nabla \left(\frac{1}{r}\right) \mathrm{d}\Omega_E \right] \mathrm{d}\Gamma_i, \tag{II.29}$$

where $\delta\nu_j$ is the difference of the reluctance of element E to which facet j belongs and the

vacuum reluctance. Using the divergence theorem on the inner integral

$$\Delta\overline{\varphi}_{r_{\Gamma_i\infty}} = -\frac{1}{4\pi}\int_{\Gamma_i}\frac{1}{S_i}\left[\sum_{j=1}^{N_f}\left(\delta\nu_j\int_{\Gamma_j}\mathbf{B}\cdot\mathbf{n}\left(\frac{1}{r}\right)\mathrm{d}\Gamma_j\right)\right]\mathrm{d}\Gamma_i. \tag{II.30}$$

Finally, applying the interpolation of induction $\mathbf{B}$ and the fact that $\mathbf{w_j}\cdot\boldsymbol{n_j} = \frac{1}{S_j}$ we obtain:

$$\Delta\overline{\varphi}_{r_{\Gamma_i\infty}} = -\frac{1}{4\pi}\int_{\Gamma_i}\frac{1}{S_i}\left[\sum_{j=1}^{N_f}\left(\frac{\delta\nu_j}{S_j}\int_{\Gamma_j}\frac{1}{r}\mathrm{d}\Gamma_j\right)\Phi_j\right]\mathrm{d}\Gamma_i. \tag{II.31}$$

The latter expression can be written in matrix form as:

$$\Delta\overline{\varphi}_{r_{\Gamma_\infty}} + \mathbf{P_m}\Phi = 0 \tag{II.32}$$

where $\mathbf{P_m}$ is what we call a volume integral matrix, which is associated to the border facets and containing the magnetic flux leakage. With the previously mentioned assumption of constant reluctance per element $\mathbf{P_m}$ writes:

$$\mathrm{P_m}_{ij} = \frac{\delta\nu_j}{4\pi}\frac{1}{S_i}\frac{1}{S_j}\int_{\Gamma_i}\int_{\Gamma_j}\frac{1}{r}\mathrm{d}\Gamma_i\mathrm{d}\Gamma_j \tag{II.33}$$

with $i = 1, 2, ..., N_{f_{EXT}}$ the number of external facets and $j = 1, 2, ..., N_f$ all the facets. We will explain the dimension of $\mathbf{P_m}$ in the next section.

System (II.32) shows the interactions given between the boundary of the ferromagnetic region and the infinity point, we call it external system. Let us remark that matrix $\mathbf{P_m}$ not only provides the link between external branches of a ferromagnetic region and the infinity point, but it also shows the connection between external facets of two different ferromagnetic regions, in case there is more than one.

II.2.c-v The resulting matrix system

The final matrix system of this magnetostatic volume integral formulation is the sum of the contributions of the internal, eq. (II.24), and external branches, eq. (II.32), obtaining the equivalent electric circuit system:

$$(\mathbf{R_m} + \mathbf{P_m})\Phi + \Delta\overline{\varphi} = \mathbf{U}^{\mathrm{H}_0} \tag{II.34}$$

where

$$\mathrm{R_m}_{ij} = \int_{\Omega_\mathrm{m}}\mathbf{w}_i\cdot\nu(\mathbf{B})\mathbf{w}_j\mathrm{d}\Omega_\mathrm{m}, \tag{II.35}$$

$$\mathrm{P_m}_{ij} = \frac{\delta\nu_j}{4\pi}\frac{1}{S_i}\frac{1}{S_j}\int_{\Gamma_i}\int_{\Gamma_j}\frac{1}{r}\mathrm{d}\Gamma_i\mathrm{d}\Gamma_j, \tag{II.36}$$

$$\Delta\overline{\varphi} = \begin{pmatrix}\Delta\overline{\varphi}_{r_{int}}\\ \Delta\overline{\varphi}_{r_b} + \Delta\overline{\varphi}_{r_{\Gamma_\infty}}\end{pmatrix}, \tag{II.37}$$

$$\mathbf{U}^{\mathrm{H}_0} = \int_{\Omega_m}\mathbf{w}_i\cdot\mathbf{H_0}\mathrm{d}\Omega_\mathrm{m}, \tag{II.38}$$

and Φ is the unknown, the magnetic flux crossing the facets of the primal mesh, corresponding to the branches of the dual mesh. Let us remark that the boundary branches are merged with the branches going to the infinity point, that we call external branches, obtaining the primal and dual mesh that Figure II.6 shows.

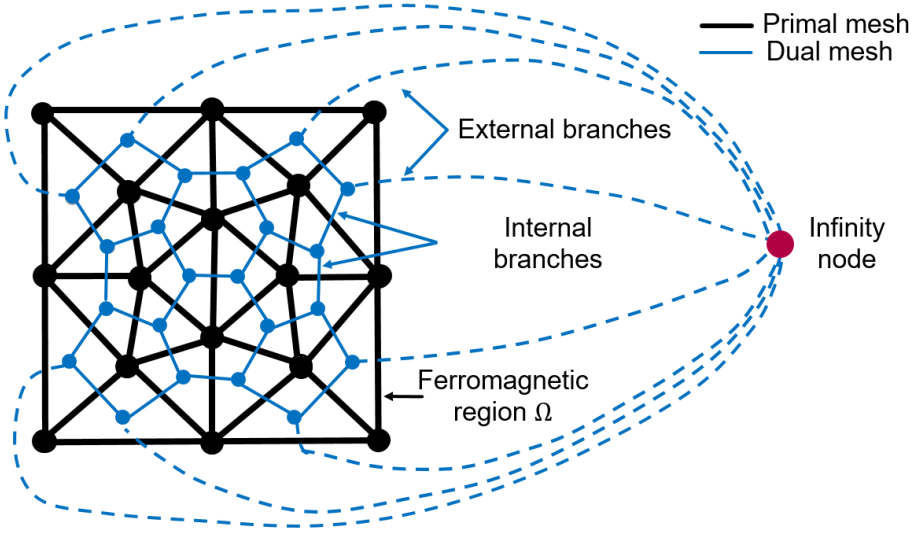

Figure II.6: Primal and dual mesh representation of a square domain in 2D merging the boundary and infinity branches.

Regarding the dimmension of the matrices:

- $\mathbf{R_m}$ is a finite element matrix, square of size $N_f \times N_f$ and sparse.
- $\mathbf{P_m}$ is a volume integral matrix that is rectangular and fully populated, of size $[N_{f_{EXT}} \times N_{f_{INT}}]$, $N_{f_{EXT}}$ is the number of external branches and $N_{f_{INT}}$ is the number of internal branches.
- $\Delta\overline{\varphi}$ is the difference of potential on the branches of the dual mesh and it is a vector of size N_f that contains the internal branches, the boundary branches and the branches going to the infinity point.
- $\mathbf{U}^{\mathrm{H_0}}$ is a source term, which is a vector of size N_f.

Figure II.7 shows the dimension of the matrices of system (II.34) for nonlinear problems. For linear problems, a simplification can be done on matrix $\mathbf{P_m}$ because the reluctivity of two elements of a linear material is the same, therefore the jump of reluctivity $\delta\nu_j$ that is a factor in matrix $\mathbf{P_m}$ is 0, and all the terms of the internal branches are null. Then, the size of matrix $\mathbf{P_m}$ is $[N_{f_{EXT}} \times N_{f_{EXT}}]$ plus the branches between regions that have different reluctivity (if there are), for which we add a block of size $[N_{f_{EXT}} \times N_{f_{BET}}]$, where $N_{f_{BET}}$ is the number of branches between regions. Figure II.8 shows this structure.

For the resolution, system (II.34) is solved with a circuit solver through the equivalent electric circuit approach, using either Kirchhoff's voltage law or Kirchhoff's current law.

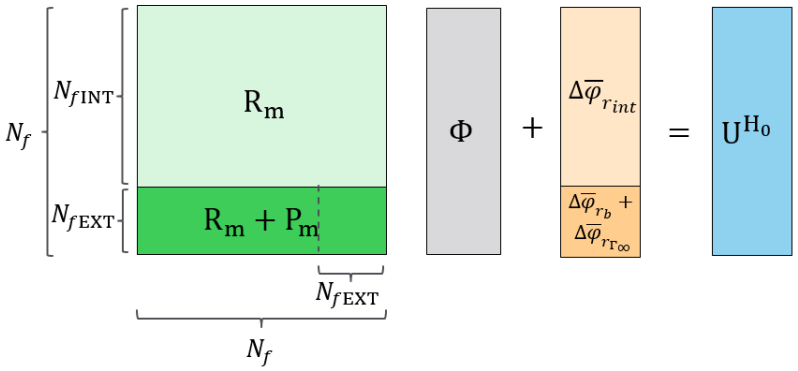

Figure II.7: Representation of the matrices dimension for system (II.34), nonlinear case.

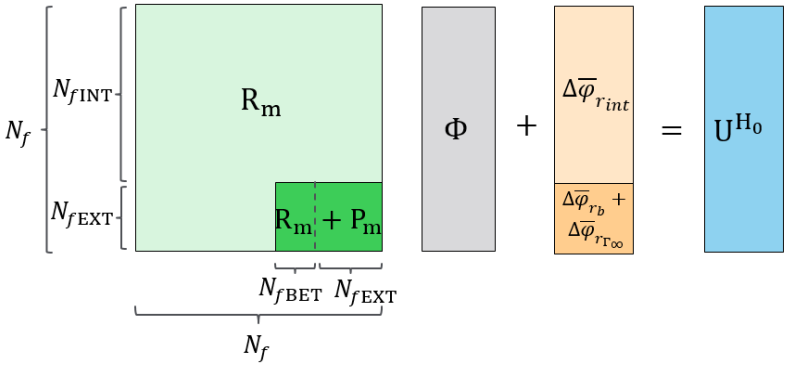

Figure II.8: Representation of the matrices dimension for system (II.34), linear case.

Let us introduce Kirchhoff's voltage law for this case. It states that the directed sum of the potential differences around a closed loop is zero, therefore

$$\mathbf{M_I} \Delta\overline{\varphi}_r = 0 \tag{II.39}$$

where $\mathbf{M_I}$ is the incidence matrix showing the link between the independent loops and the circuit branches of size $N_f \times N_l$, being N_l the number of independent loops of the problem and

$$\mathbf{M_I}_{ij} = \begin{cases} \pm 1 & \text{if branch } j \text{ is in loop } i \\ 0 & \text{otherwise} \end{cases} \tag{II.40}$$

The sign of 1 depends on the orientation of the branch in the loop. Then, with graph theory we can find the independent loops on the mesh using tree and co-tree techniques that need the topological description of the circuit. The size of $\mathbf{M_I}$ is [the number of independent loops, number of independent branches], such as the one shown in Figure II.9 for the 2D example previously presented. Taking this into account, the magnetic flux through the branches can be decomposed as:

$$\Phi = \mathbf{M_I}^{\mathrm{T}} \Phi_{\mathrm{l}} \tag{II.41}$$

where $\mathbf{M_I}^{\mathrm{T}}$ is the transpose of the incidence matrix $\mathbf{M_I}$ and Φ_l is the flux of the independent loops.

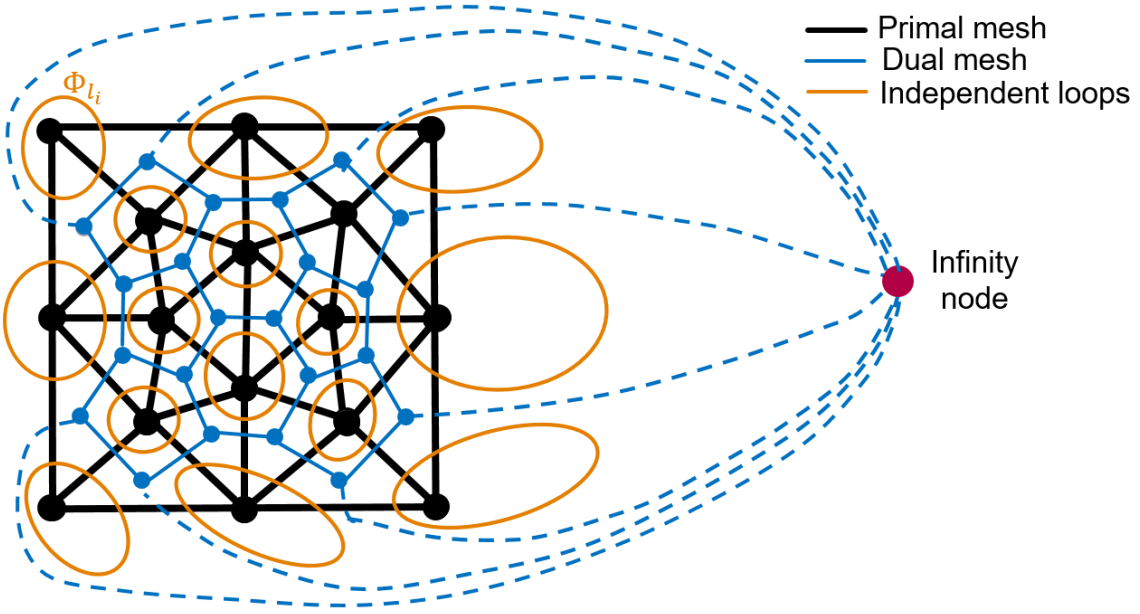

Figure II.9: Kirchhoff's voltage independent loops for a 2D case.

Using equations (II.39) and (II.41), system (II.34) writes:

$$\mathbf{M_I}(\mathbf{R_m} + \mathbf{P_m})\mathbf{M_I}^{\mathrm{T}}\Phi_{\mathrm{l}} = \mathbf{M_I}\mathbf{U}^{\mathrm{H_0}}. \tag{II.42}$$

We remark that this procedure ensures the free divergence of $\mathbf{B}$, given that the circuit representation allows to write:

$$\nabla \cdot \mathbf{B} = \nabla \cdot (\sum_{i=1}^{N_f} \mathbf{w}_i \Phi_i) = \sum_{i=1}^{N_f} \nabla \cdot (\mathbf{w}_i \Phi_i) = \frac{1}{V_E} \sum_{i=1}^{N_f} \Phi_i \tag{II.43}$$

Verifying any of the two Kirchhoff's rules $\sum_{\mathrm{i=1}}^{\mathrm{N_f}} \Phi_{\mathrm{i}} = 0$ holds, therefore $\nabla \cdot \mathbf{B} = 0$.

In practice, the resolution of system (II.42) is carried out with a Generalized Minimal RESidual (GMRES) iterative solver. For the nonlinear case, an additional imbricated Newton-Raphson (NR) loop is considered. To do that, the computation of the jacobian matrices is needed:

- The jacobian contribution of $\mathbf{R_m}$ matrix is expressed as:

$$J(\mathrm{R_m}_{ij}) = \int_{\Omega_{\mathrm{m}}} \mathbf{w}_i \cdot \left[\frac{\partial \mathbf{H}}{\partial \mathbf{B}}\right] \mathbf{w}_j \mathrm{d}\mathbf{\Omega}_{\mathrm{m}} \tag{II.44}$$

  where J is the jacobian and $\left[\frac{\partial \mathbf{H}}{\partial \mathbf{B}}\right]$ is the tensor containing the partial derivative of each component of $\mathbf{H}$ with respect to each component of $\mathbf{B}$ [25].

- The jacobian contribution of $\mathbf{P_m}$ matrix would be very time consuming to compute at each iteration. Contrary to the case of $\mathbf{R_m}$, $\mathbf{P_m}$ matrix does not depend strongly on $\mathbf{B}$. This happens because of the reluctivity jump $\delta\nu$ present in its expression, for which there are two cases, either $\delta\nu = (\nu_{E_1} - \nu_{E_2})$ for two adjacent elements E_1

and E_2, which is a very low value; or $\delta\nu = \nu_{E_b} - \nu_0$, where E_b is an element on the boundary, and it that case ν_0 is the dominant term. Then the dependency of $\mathbf{P_m}$ matrix on $\mathbf{B}$ is very low and we approximate the contribution of the jacobian of $\mathbf{P_m}$ by itself, without any further computation:

$$J(\mathbf{P_m}) \approx \mathbf{P_m}. \tag{II.45}$$

To summarize, until now we have found the matrix system for a B-conforming formulation based on the induction and we have used an equivalent electric circuit approach that allows to solve the system with Kirchhoff's current or voltage rule that ensures the free divergence of the induction. Finally, we have explained how to deal with nonlinear problems computing the jacobian matrices. Now, let us provide various strategies to perform some specific computations.

II.2.d Other considerations of the VIM facet formulation

There are some additional considerations to take into account to solve system (II.42), making this formulation more efficient and reducing the computation time:

- Starting from the computation of $\mathbf{P_m}$,

$$\mathrm{P_m}_{ij} = \frac{\delta\nu_j}{4\pi}\frac{1}{S_i}\frac{1}{S_j}\int_{\Gamma_i}\int_{\Gamma_j}\frac{1}{r}\mathrm{d}\Gamma_i\mathrm{d}\Gamma_j, \tag{II.46}$$

  where we supposed a constant reluctance assumption per element. This assumption is already true for simplex elements, which is the case of tetrahedrons. It is not the case of hexahedrons, but again, since the dominant term of $\mathbf{P_m}$ matrix for the reluctivity jump $\delta\nu = (\nu_{E_b} - \nu_0)$ is ν_0, the fact of assuming a constant reluctivity per element is not very significative.

- Let us notice that $\mathbf{P_m}$ has a singularity on Green's function. It is important to be careful with the computation of the numerical integration, for which there are two options:

  1. The external integral is computed numerically using Gauss points and the internal one is computed with the analytical integration [40, 41].
  2. The external integral is computed numerically using Gauss points and the internal one is computed numerically as well but taking different Gauss points (shifted Gauss points).

  In general, the first option provides better results, because the shifted Gauss points could be very close to each other. For the nonlinear case, thanks to the assumption of constant reluctivity per element, $\mathbf{P_m}$ matrix is computed only once, being updated at each Newton-Raphson iteration without re-computing the terms.

- Another remark regarding $\mathbf{P_m}$ matrix is to notice that $\delta\nu_j$ is null for internal elements of a ferromagnetic region that is composed of a linear material. Furthermore, if the problem that we are considering has only one ferromagnetic region and it is

linear, then $\mathbf{P_m}$ will be a square matrix as we can see on Fig. II.8 that shows the representation of the matrices dimensions.

- Given a mesh, there are multiple possibilities to construct the incidence matrix $\mathbf{M_I}$ to apply Kirchhoff's voltage law [38, 39]. Then, the number of unknowns of the system is the number of independent loops of the mesh. The computation time of the system also depends on how the independent loops are created. Let us note that this process can also be carried out with Kirchhoff's current law.

- In order to speed the computations, a matrix compression technique can be used, such as the Fast Multiple Method (FMM) [15], Adaptive Cross Approximation (ACA) [16] or Hybrid Cross Approximation (HCA) [18] on matrix $\mathbf{P_m}$. To do that, the use on an iterative solver is compulsory, in our case of GMRES type, and it is accelerated with a LU type preconditioner on matrix $\mathbf{R_m}$ as in [36], which is included in the code using MUMPS library [37].

Once we know how to solve the matrix system defining the problem and we have taken into account these considerations to speed up the computations, let us explain how the solution Φ is used for the computation of other variables.

II.2.e Extraction of the induction at each point

The value of the flux through each facet of the mesh Φ_i is obtained by solving system (II.34). Now, to obtain the induction $\mathbf{B}$ on all the domain, there are some calculations to do.

For a point p in the interior of the ferromagnetic regions, induction $\mathbf{B}$ is computed simply by using the interpolation formula that we have explained previously:

$$\mathbf{B}(p) = \sum_{j=1}^{N_f} \mathbf{w}_j(p)\Phi_j(p) \tag{II.47}$$

For a point q that is not in the ferromagnetic region we can compute the value of $\mathbf{H}$ field and use the constitutive relation (II.4) to obtain the induction $\mathbf{B}$. Following equation (II.9) we have:

$$\mathbf{H}(q) = -\nabla_q(\varphi_r) + \mathbf{H}_0(q). \tag{II.48}$$

We saw in eq. (II.8) the expression of φ_r:

$$\varphi_r = \sum_{\Omega_E \in \Omega_\mathrm{m}} \frac{1}{4\pi} \int_{\Omega_E} \mathbf{M} \cdot \nabla \left(\frac{1}{r}\right) \mathrm{d}\Omega_E,$$

taking into account that $\nabla \cdot \mathbf{M} = 0$ at each element given that $\nabla \cdot \mathbf{B} = 0$ and a constant permeability per mesh element, the following expression holds:

$$\nabla \cdot \left(\frac{1}{r}\mathbf{M}\right) = \nabla\left(\frac{1}{r}\right) \cdot \mathbf{M} + \frac{1}{r}\nabla \cdot \mathbf{M} = \nabla\left(\frac{1}{r}\right) \cdot \mathbf{M} = \mathbf{M} \cdot \nabla\left(\frac{1}{r}\right). \tag{II.49}$$

Then, the divergence theorem can be applied to φ_r, obtaining:

$$\varphi_r(q) = \frac{1}{4\pi} \sum_{j=1}^{N_f} \int_{\Gamma_j} \delta \mathrm{M}_{nj} \left(\frac{1}{r} \right) \mathrm{d}\Gamma_j \tag{II.50}$$

that is to say, the integral over all the facets elements Γ_j, where M_{nj} is the magnetization difference between the two volume elements E_1 and E_2 that share facet j, having $\delta \mathrm{M}_{nj} = \mathrm{M}_{nE1} - \mathrm{M}_{nE2} = (\nu_{E2} - \nu_{E1}) \mathbf{B} \cdot \boldsymbol{n}$ where $\boldsymbol{n}$ is the outgoing normal from E_1. Since in equation (II.50) only $\frac{1}{r}$ depends on point q, we can write the gradient of φ_r as follows:

$$\nabla_q \varphi_r(q) = \frac{1}{4\pi} \sum_{j=1}^{N_f} \int_{\Gamma_j} \delta \mathrm{M}_{nj} \left(\nabla_q \frac{1}{r} \right) \mathrm{d}\Gamma_j = \sum_{j=1}^{N_f} \frac{1}{4\pi} \int_{\Gamma_j} \delta \mathrm{M}_{nj} \left(-\frac{\boldsymbol{r}}{r^3} \right) \mathrm{d}\Gamma_j. \tag{II.51}$$

Finally, injecting the latter expression (II.51) in (II.48), the value of $\mathbf{H}$ in q is given by:

$$\mathbf{H}(q) = \frac{1}{4\pi} \sum_{j=1}^{N_f} \int_{\Gamma_j} \delta \mathrm{M}_{nj} \left(-\frac{\boldsymbol{r}}{r^3} \right) \mathrm{d}\Gamma_j + \mathbf{H}_0(q). \tag{II.52}$$

If the ferromagnetic region is composed of an isotropic linear material, then $\delta \mathrm{M}_{nj} = 0$ for the facets in the ferromagnetic region, and the only facets considered in the sum of the previous expression are the external facets of the regions.

Once we have $\mathbf{H}(q)$, given that q is in the air, the value of the induction $\mathbf{B}$ at q is:

$$\mathbf{B}(\mathrm{q}) = \mu_0 \mathbf{H}(\mathrm{q}). \tag{II.53}$$

II.2.f Magnetic flux computation through coils

The value of the induction at each point is now known. For the post-treatment of the solution, we focus on the computation of the magnetic flux through coils, given that it is the measurement of interest for the current sensors application, which will ensure their accuracy. To have a precise computation we will use the result of [42] which states that given a coil Ω_{c_k} for $k = 1, 2, ..., N_c$ where N_c is the number of coils, the magnetic flux through a coil k is computed by:

$$\begin{aligned} \Phi_{\Omega_{c_k}} = \int_{\Omega_{c_k}} \mathbf{j}_{\mathbf{c}_k} \cdot \mathbf{A} \mathrm{d}\Omega_{c_k} = \int_{\Omega_{c_k}} \mathbf{j}_{\mathbf{c}_k} \cdot \mathbf{A_0} \mathrm{d}\Omega_{c_k} + \int_{\Omega_{c_k}} \mathbf{j}_{\mathbf{c}_k} \cdot \mathbf{A_m} \mathrm{d}\Omega_{c_k} \overset{[42]}{=} \\ \frac{\mu_0}{4\pi} \int_{\Omega_{c_k}} \mathbf{j}_{\mathbf{c}_k} \left(\sum_{l=1}^{N_c} \mathrm{I}_l \int_{\Omega_{c_l}} \frac{\mathbf{j}_{\mathbf{c}_l}}{r} \mathrm{d}\Omega_{c_l} \right) \mathrm{d}\Omega_{c_k} + \mu_0 \int_{\Omega_{\mathrm{m}}} \mathbf{h}_{\mathbf{c}_k} \cdot \mathbf{M} \mathrm{d}\Omega_{\mathrm{m}} \end{aligned} \tag{II.54}$$

where $\mathbf{j}_{\mathbf{c}_k}$ is the current density produced by coil k with an imposed current of 1 A, $\mathbf{h}_{\mathbf{c}_k}$ is the magnetic field generated by coil k with 1 A in vacuum, which can be obtained with Biot-Savart law, $\mathbf{A}$ is the magnetic vector potential, $\mathbf{A_0}$ and $\mathbf{A_m}$ are the magnetic vector potential generated by coils in vacuum and in magnetic regions respectively, I_l is the current flowing in coil l and r is the distance between the integration point in coils and the computation point of the vector potential. Let us notice that the two terms to compute (final expression of (II.54)) are fairly different:

1. The first term has a double integral over the coil regions, therefore a mesh of the coils is needed. For the inner integral, there are analytical formulas if the coil is circular [40, 41, 43, 44, 45]. If it is not circular, a mesh of the coil can be created with for example hexahedra or tetrahedra, and assuming that j_{0_k} is uniform at each mesh element, there are also analytical expressions to compute the inner integral. For the outer integral in general there is no analytical formula and a numerical integration is needed.

2. The second term is integrated over the magnetic region, and the definition of the coil is used to evaluate $\mathbf{h}_{\mathbf{c}_k}$.

We remark that when a coil is not encircled by a magnetic circuit the first term has more impact than the second one, and its computation is very precise, using analytical expressions for the inner integral. This is where the volume integral method shows its potential compared to the finite element method, because the finite element method would compute the magnetic flux through coils with an integral over the mesh elements that are around the coils, which has to be very thin to obtain good accuracy, but the mesh of the air around a coil is a vast area and a thin mesh would take long computation time.

II.2.g NSX sensor application

To validate the magnetostatic linear and nonlinear volume integral formulation, we consider NSX sensor, previously presented in I.2.c.

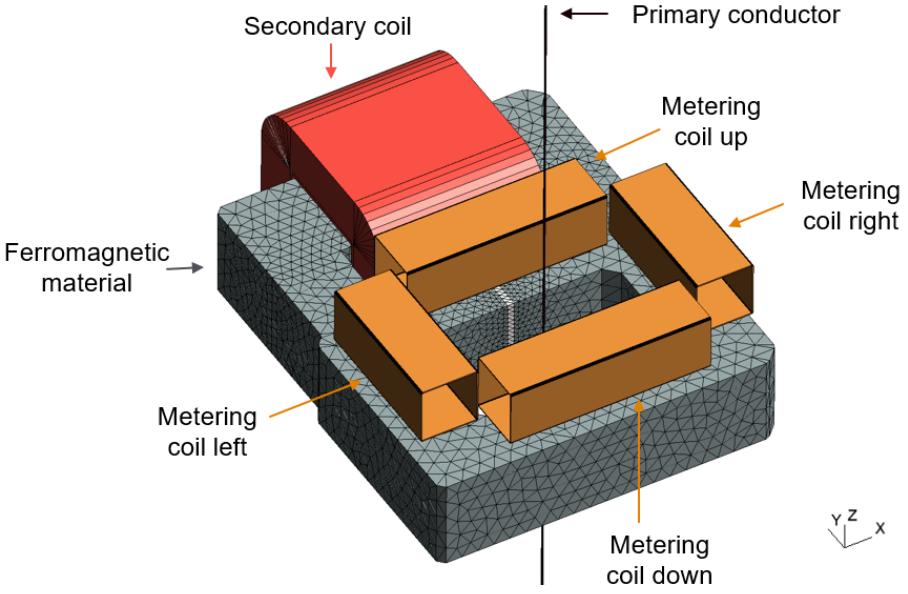

Figure II.10: NSX simulation model, meshed with 46 000 volume elements.

It is a current transformer with a metering coil on top of it, divided in four parts. The current transformer has a ferromagnetic region with a large air gap in the middle, a primary coil and a secondary coil, as shown in Fig. II.10. The two thin air gaps are not considered in this application. We aim at computing the magnetic flux through the

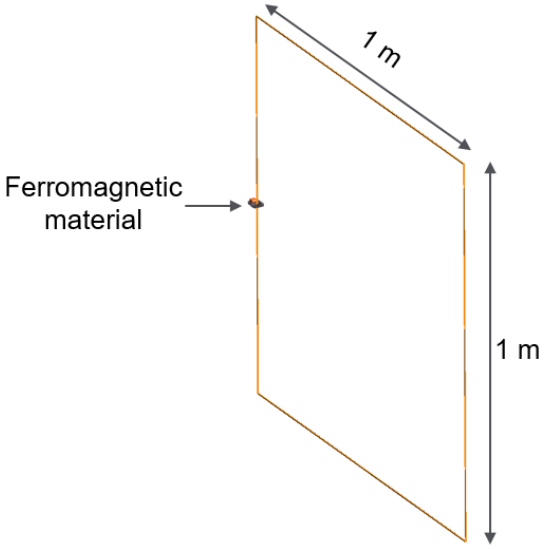

Figure II.11: Primary conductor dimension of NSX sensor.

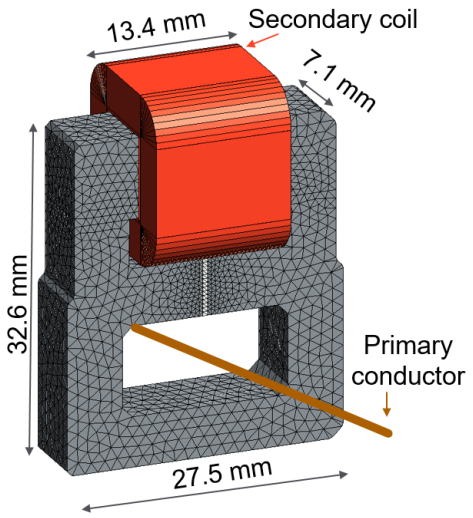

Figure II.12: Dimension of NSX sensor.

secondary coil and through the four parts of the metering coil.
Regarding the characteristics and parameters of the model:

- For the ferromagnetic region, two cases are considered with different materials. The first case is an isotropic linear material with μ_r =1000 and the second one is a nonlinear material following an isotropic analytic saturation of arc tangent type with two coefficients: μ_r =1000 and saturation magnetization = 1.2 T.

- The primary conductor has imposed current of 1 A for the linear case and for the nonlinear case we consider a set of imposed currents {0.1, 0.5, 1, 2, 5, 10, 20, 50, 100, 200} A. It is defined as a closed loop of dimension 1 meter times 1 meter. Its large length avoids the return of the conductor to have an effect on the ferromagnetic region (Figure II.11).

- The secondary coil has 980 turns and no imposed current.

- The four parts composing the metering coil have 825 turns each, making 3300 turns in total. They are called down, up, right and left as in Figure II.10. There is no current imposed on them.

- The main dimension of the sensor are shown in Figure II.12.

The result of our implementation of the VIM is compared with the commercial software Flux3D of Altair [30], which is based on FEM. Let us show the results for the linear case and the nonlinear case separately.

Linear case

To test the linear material, we have created four different meshes with 12000, 24000, 46000 and 96000 elements to perceive the convergence of the mesh. For VIM the number

of mesh elements given corresponds to the number of elements of the ferromagnetic region (the current transformer in this case, CT), for FEM the number of mesh elements given also corresponds to the elements of the ferromagnetic region, but there are many more elements meshing the air around the ferromagnetic region, which don't exist in VIM case. For a given mesh we compute the relative difference between FEM and VIM as

$$\text{relative difference} = \frac{\text{abs}(\text{valueFEM} - \text{valueVIM})}{\text{valueVIM}},$$

where abs denotes the absolute value. Figure II.13 shows the flux through the secondary coil for FEM and VIM with their relative difference. We see that the results get closer as the number of mesh elements increases: for a mesh of 46000 the relative difference is 0.38% whereas for 96000 elements the relative difference is inferior to 0.1%. Both methods converge at the same ratio approximately.

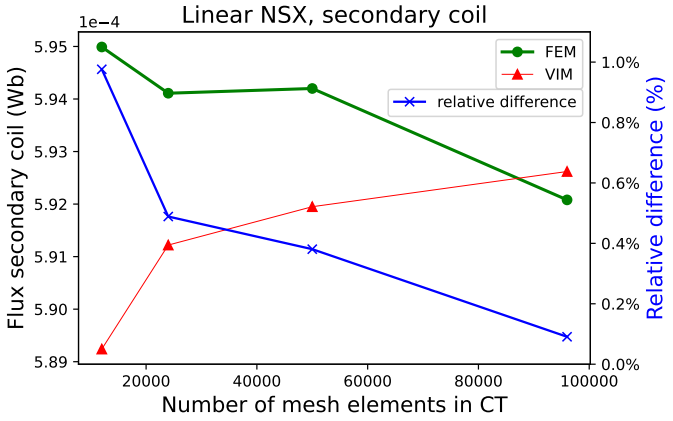

Figure II.13: Mesh convergence for linear material computing the flux through the secondary coil.

Figures II.14a and II.14b show the flux through up and down metering coils and through right and left metering coils repectively for each of the four different meshes of 12000, 24000, 46000 and 96000 elements. Values obtained for down and right metering coils are negative but we have represented them as positive to have a narrower scale on the y axis that allows to appreciate better the differences between FEM and VIM. At a first glimpse we see that left and right coils provide results that are quite similar given that NSX sensor is symmetric with respect to x-axis. We notice that VIM results are homogeneous for the four metering coils (horizontal lines) whereas FEM results vary with the number of mesh elements, meaning that VIM converges for a coarse mesh.

Figure II.14 shows the relative difference between FEM and VIM for each of the four parts of the metering coil. We see that the difference is higher for a coarse mesh, and it gets lower as the number of mesh elements increases, for instance the metering coil right has 18.6% of relative difference for a mesh of 12000 elements and 2.63% for a mesh of 96000 elements. The lowest relative difference is obtained for a mesh of 96000 elements, having 2.63%, 2.64%, 3.27% and 4.30% for the left, right, down and up coil respectively. We conclude that VIM is more stable to compute the flux through the metering coil of NSX sensor.

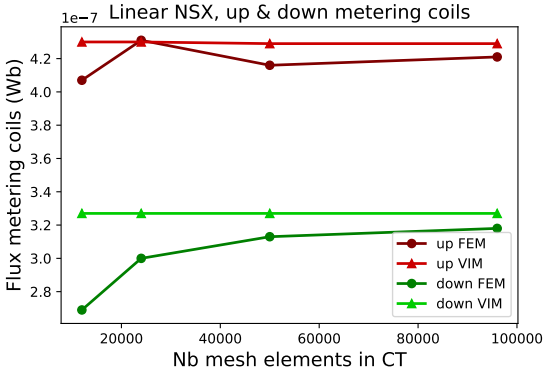

(a) Flux through up and down metering coils.

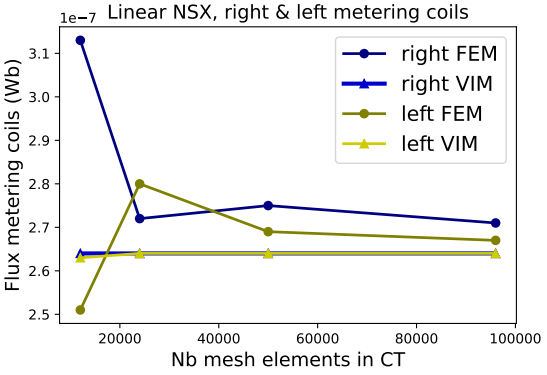

(b) Flux through right and left metering coils.

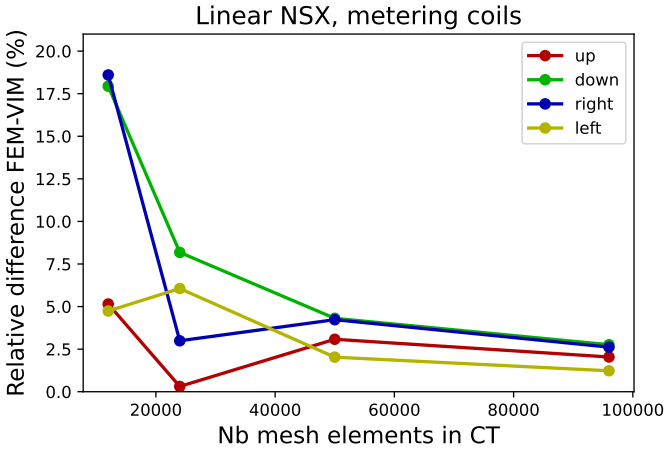

(c) Relative difference between FEM and VIM for all the metering coils.

Figure II.14: Mesh convergence for linear material with the flux through the metering coils.

Given these results, we validate the magnetostatic linear model, where we have seen two different types of coils:

- For coils that are around a magnetic material VIM and FEM show similar results, with a relative difference inferior to 0.1% on the secondary coil of NSX with a mesh of 96000 elements.

- For coils that have a higher contribution of the magnetic flux in the air, as it is the case of the metering coils, VIM shows more stable results for all the meshes shown.

Nonlinear case

For the nonlinear material we have selected the mesh previously presented with 96000 elements because it is the one that provides better results. The computation of the flux through the secondary coil is shown in Figure II.15 for imposed currents {0.1, 0.5, 1, 2, 5, 10, 20, 50, 100, 200, 500} A on the primary coil.

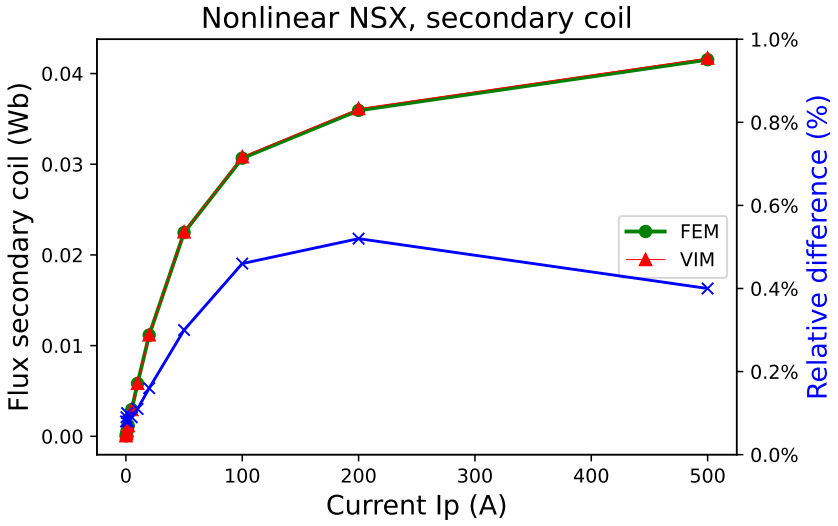

Figure II.15: NSX results for nonlinear material, secondary coil.

The relative difference obtained between FEM and VIM on the flux through the secondary coil is inferior to 0.6%.

The flux through each of the four metering coils with FEM and VIM are given in Figure II.16a. We notice again that left and right coils show almost the same flux because of the x-axis symmetry. We also notice that the metering coil doesn't show a high saturation effect, this occurs because when computing the flux of these coils, the contribution of the part that is in the air, first term of eq. (II.54), is much higher than the contribution of the magnetic circuit.

In Figure II.16b we can see the relative difference between FEM and VIM for the four metering coils, obtaining values in the range $[0, 3.5]\,\%$. The magnitude of these values is consistent with the ones obtained in the linear case for a mesh of 96000 elements.

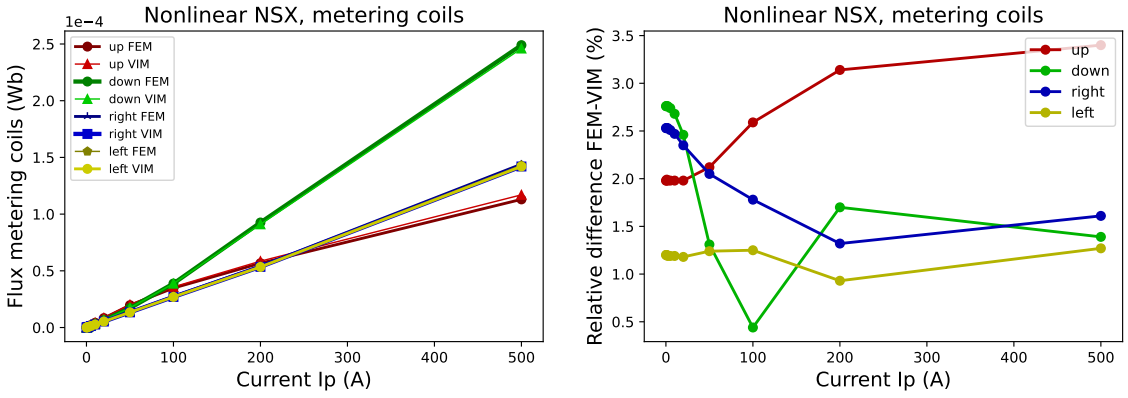

(a) Flux through metering coils.

(b) Relative difference between FEM and VIM.

Figure II.16: NSX results for nonlinear material, metering coils.

We then validate the magnetostatic nonlinear model, having again two cases:

- For coils that are placed around the ferromagnetic material, the relative difference between FEM and VIM is inferior to 0.6%.

- For coils that have a higher contribution of the magnetic flux in the air as it is the case of the metering coils, the relative difference between FEM and VIM is higher, obtaining the convergence for VIM but less accurate results for FEM.

II.3 Thin air gaps model for magnetostatic VIM

When modeling ferromagnetic devices, a popular feature is the presence of air gaps. We distinguish two types of air gaps: the ones that are very thin, arising for instance when two ferromagnetic parts are welded; and large air gaps that are thicker. An air gap will be classified as thin or large depending on the dimension of the device that is part of, for example, in our sensors of a few centimeters of length and width, a thin air gap would be of a thickness inferior to 50 μm and a large air gap would have a thickness of a few millimeters.

Thin and large air gaps usually have a different purpose. In general, thin air gaps are a side effect that occurs when positioning the secondary winding of the current transformer: the ferromagnetic region is formed by two pieces in order to insert the secondary coil and then the two pieces are welded to close the region, creating an air gap where the welding has been made. Large air gaps are different and they are often created consciously to force the magnetic flux to go in a specific direction. In any case, the presence of air in these regions changes the electromagnetic behaviour therefore it is important to have a specific numerical treatment for them. In terms of modeling, large air gaps don't cause many troubles, nevertheless, thin air gaps do due to the proximity of the two air gap faces. In this section, we focus on modeling thin air gaps.

Since we are using the VIM method and we don't necessarily need to mesh the air region, there are two options to model a thin air gap: the first one is to not mesh the air gap, but the proximity of the two air gap faces leads to inaccurate integral computations of Green's kernel, eq. (II.36). The second option is to mesh the air gap as a volume element, this case is more accurate than not meshing the air gap but it also leads to difficult integral calculations on the mesh elements of the air gap due to the proximity of the two air gap faces and to the elongated shape mesh elements that model the air gap.

We propose an alternative to model thin air gaps, which consists in meshing the air gap as a face region and apply a numerical treatment that depends on the thickness of the air gap. This alternative avoids the numerical difficulty that arises when the air gap is not meshed. It also allows to prevent the difficult integrals computation that arise when meshing it as a volume element. The three air gap mesh options are shown in Figure II.17 for the case of a ferromagnetic region with an air gap and a coil.

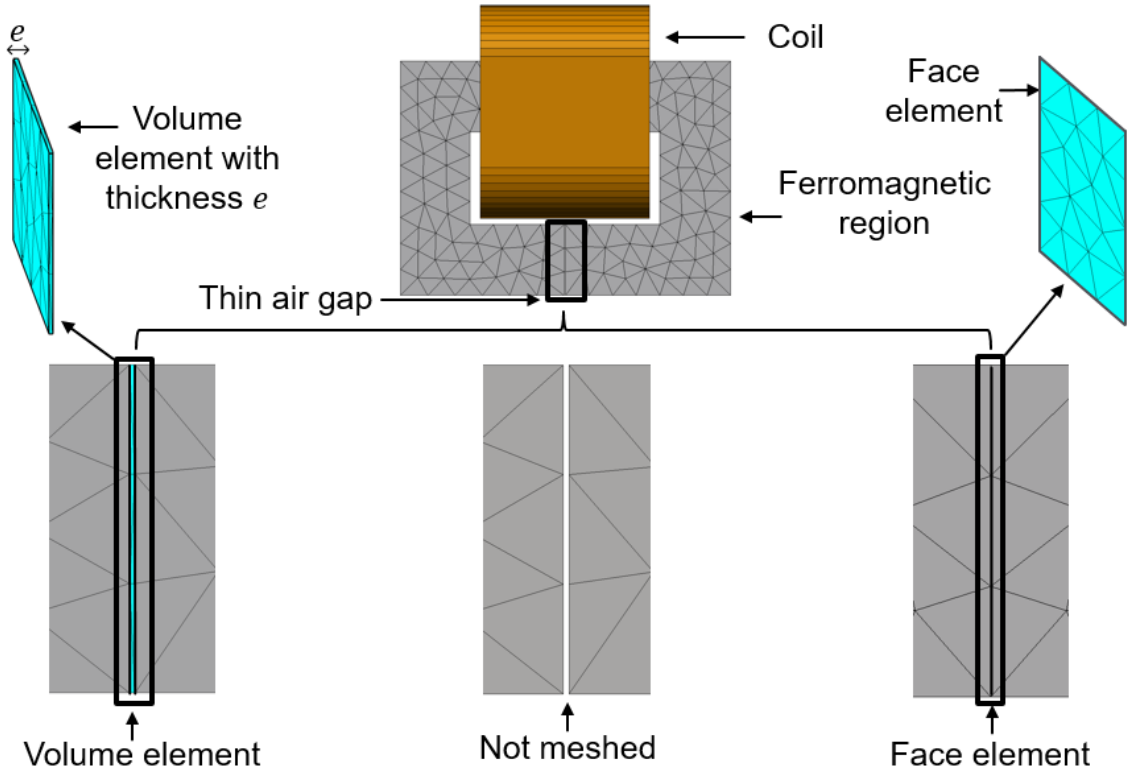

Figure II.17: Air gap mesh options.

II.3.a Face air gap model development

In order to consider that the air gap is a face region instead of a volume region, let us consider the following assumptions:

1. The thickness of the air gap is small compared to the dimension of the ferromagnetic region.
2. There is no lateral flux leakage from the face of the air gap to the air.
3. Flux inside the air gap has perpendicular direction to the air gap. This occurs because the vacuum permeability is much lower than the ferromagnetic region permeability and the thickness of the air gap is small.

Figure II.18 shows the mesh difference when considering the air gap as a volume element and as a face element.

The air gap modeling strategy will be made adding the air gap contribution to matrices $\mathbf{R_m}$ and $\mathbf{P_m}$ of system (II.34). For the finite element matrix $\mathbf{R_m}$, a reluctance on the branches i that cross the air gap is added, expressed by $\frac{\mu_0 e}{S_i}$, therefore for branches i that belong to the air gap we have

$$\mathrm{R}_{\mathrm{m}_{ij}} = \int_{\Omega_\mathrm{m}} \mathbf{w}_i \cdot \nu(\mathbf{B}) \mathbf{w}_j \mathrm{d}\Omega_\mathrm{m} + \frac{\mu_0 e}{S_i}, \tag{II.55}$$

where e is the thickness of the air gap and S_i the surface of element i. It can also be seen as the reluctance of a parallelepiped of surface S_i and depth e. The contribution of the

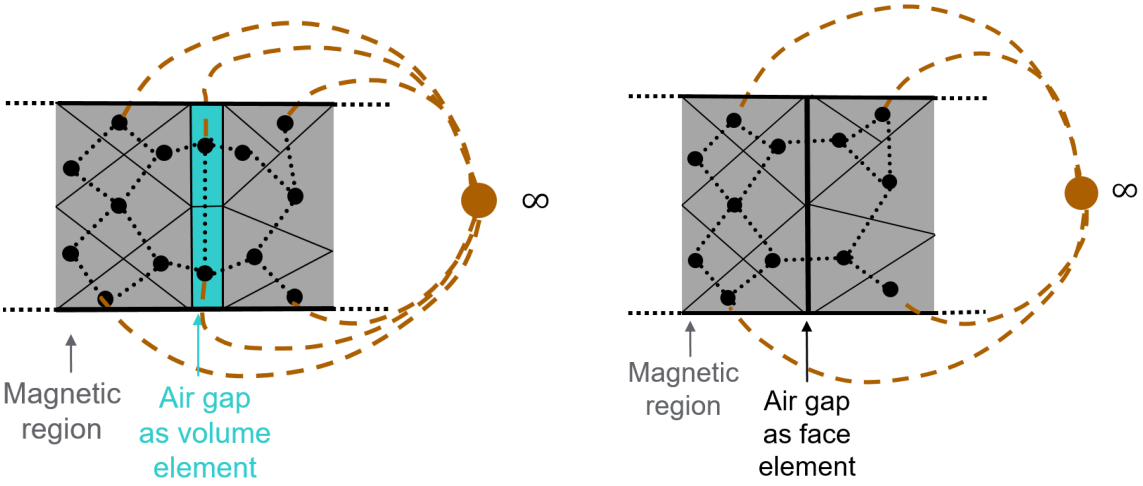

Figure II.18: Equivalent magnetic circuit of a region with an air gap as a volume element (left) and as a face element (right).

volume integral matrix $\mathbf{P_m}$ is more elaborated: we consider that the air gap is defined by two parallel faces Γ_1 and Γ_2 separated by a distance e and we aim at obtaining the link between a branch crossing Γ_1 face and a branch crossing Γ_2 face (Fig. II.19). We name the evaluation between these two branches $\mathrm{P}_{\mathrm{m}_{i,\Gamma 12_j}}$:

$$\begin{aligned}\mathrm{P}_{\mathrm{m}_{i,\Gamma 12_j}} = \frac{1}{4\pi}\int_{\Gamma_i}\frac{1}{S_i}\int_{\Gamma 1_j}\frac{1}{S_j}(\nu_1-\nu_0)\frac{1}{r_1}\mathrm{d}\Gamma 1_j\mathrm{d}\Gamma_i - \\ \frac{1}{4\pi}\int_{\Gamma_i}\frac{1}{S_i}\int_{\Gamma 2_j}\frac{1}{S_j}(\nu_2-\nu_0)\frac{1}{r_2}\mathrm{d}\Gamma 2_j\mathrm{d}\Gamma_i\end{aligned} \tag{II.56}$$

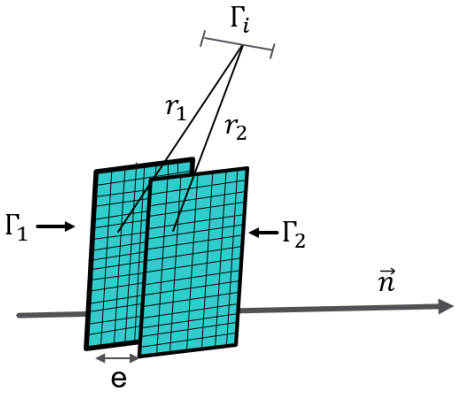

Figure II.19: Two parallel faces defining the air gap.

where $i = 1, 2, ..., N_b$ are the boundary elements of the ferromagnetic region, therefore Γ_i are external branches going to the infinity point and $\Gamma 1_j$ and $\Gamma 2_j$ are the facet elements j that are on face Γ_1 and Γ_2 respectively. Minus sign between the two terms arises from the orientation of the faces, going from Γ_1 to Γ_2 by agreement. ν_1 and ν_2 are the magnetic

reluctivity on face Γ_1 and Γ_2. Let us express the reluctivity as:

$$\nu_1 = \overline{\nu} + \frac{\delta\nu}{2} \qquad\qquad \nu_2 = \overline{\nu} - \frac{\delta\nu}{2} \tag{II.57}$$

where $\overline{\nu} = \frac{\nu_1+\nu_2}{2}$ and $\delta\nu = \nu_1 - \nu_2$. Then rearranging the terms, eq. (II.56) reads:

$$\begin{aligned} \mathrm{P}_{\mathrm{m}_{i,\Gamma_{12_j}}} &= \frac{1}{4\pi}\int_{\Gamma_i}\frac{1}{S_i}\frac{\delta\nu}{2}\frac{1}{S_j}\Big[\int_{\Gamma_{1_j}}\frac{1}{r_1}\mathrm{d}\Gamma_{1_j} + \int_{\Gamma_{2_j}}\frac{1}{r_2}\mathrm{d}\Gamma_{2_j}\Big]\mathrm{d}\Gamma_i - \\ &\frac{1}{4\pi}\int_{\Gamma_i}\frac{1}{S_i}(\overline{\nu}-\nu_0)\frac{1}{S_j}\Big[\int_{\Gamma_{1_j}}\frac{1}{r_1}\mathrm{d}\Gamma_{1_j} - \int_{\Gamma_{2_j}}\frac{1}{r_2}\mathrm{d}\Gamma_{2_j}\Big]\mathrm{d}\Gamma_i = \mathrm{A} - \mathrm{B}. \end{aligned} \tag{II.58}$$

Let us comment the latter equation. It shows the link between two faces that are in front of each other, and it would appear in the two unsatisfying air gap modelizations explained before: if the air gap is not meshed and if it is meshed with volume elements. When the air gap is thin, then distances r_1 and r_2 are almost identical, and the difference that is in brackets in each of the two terms can lead to inaccuracy. The difference between the two cases is that if the air gap is not meshed, the inaccuracy is given on both matrices $\mathbf{R_m}$ and $\mathbf{P_m}$, whereas if the air gap is meshed as a volume element, the inaccuracy is only given on matrix $\mathbf{P_m}$.
For the face air gap model, we will do a numerical approximation of each of the two terms of eq. (II.58).

1. First term: we use a Taylor expansion on r_1 and r_2 such that

   $$\frac{1}{r_1} + \frac{1}{r_2} = \frac{2}{r} + \varepsilon(\mathrm{O}^2) \approx \frac{2}{r},$$

   then we write the first term as:

   $$\mathrm{A} = \frac{1}{4\pi}\int_{\Gamma_i}\frac{1}{S_i}\int_{\Gamma_j}\frac{1}{S_j}\frac{\delta\nu}{r}\mathrm{d}\Gamma_j\mathrm{d}\Gamma_i. \tag{II.59}$$

2. Second term: we use $\nabla(\frac{1}{r})\cdot\boldsymbol{n} = \frac{\mathrm{d}}{\mathrm{d}\boldsymbol{n}}(\frac{1}{r}) \approx \lim_{e\to 0}\frac{\frac{1}{r_1}-\frac{1}{r_2}}{\mathrm{e}}$, to obtain

   $$\frac{1}{r_1} - \frac{1}{r_2} \approx \mathrm{e}\nabla(\frac{1}{r})\cdot\boldsymbol{n},$$

   then we write the second term as:

   $$\mathrm{B} = \frac{1}{4\pi}\int_{\Gamma_i}\frac{1}{S_i}\int_{\Gamma_j}(\overline{\nu}-\nu_0)\frac{1}{S_j}\mathrm{e}\nabla(\frac{1}{r})\cdot\boldsymbol{n}\mathrm{d}\Gamma_j\mathrm{d}\Gamma_i. \tag{II.60}$$

Assembling both terms, we have:

$$\mathrm{P}_{\mathrm{m}_{i,\Gamma_{12_j}}} = \frac{1}{4\pi}\int_{\Gamma_i}\frac{1}{S_i}\int_{\Gamma_j}\frac{1}{S_j}\frac{\delta\nu}{r}\mathrm{d}\Gamma_j\mathrm{d}\Gamma_i + \frac{1}{4\pi}\int_{\Gamma_i}\frac{1}{S_i}\int_{\Gamma_j}(\overline{\nu}-\nu_0)\frac{1}{S_j}\mathrm{e}\nabla(\frac{1}{r})\cdot\boldsymbol{n}\mathrm{d}\Gamma_j\mathrm{d}\Gamma_i. \tag{II.61}$$

Let us notice that the first term of $\mathrm{P}_{\mathrm{m}_{i,\Gamma_{12_j}}}$ is $\mathbf{P}_{\mathbf{m}_{ij}}$ obtained in the magnetostatic formulation without considering air gaps, eq. (II.36), being the second term the additional

contribution of the air gaps. This new contribution describing the air gap will be added to $\mathbf{P_m}$ matrix in the terms that represent the branches crossing the air gaps.

Therefore, the face air gap model is composed of two contributions, one on matrix $\mathbf{R_m}$ and another in matrix $\mathbf{P_m}$. We remark that when the thickness of the air gap is small, the correction of matrix $\mathbf{R_m}$ can be enough to capture the air gap behaviour. Nevertheless, when the air gap is thicker, it is important to consider correction of matrix $\mathbf{P_m}$ too.

II.3.b Applications

In order to validate the face air gap model we will present two applications, an academic case and NSX sensor previously shown. We will compare the results of the face air gap model with the volume air gap model.

II.3.b-i Academic case

The academic case is composed of a ferromagnetic region with an air gap and a coil around the region as Figure II.20 shows. A current is imposed on the coil and the result will be the computation of the magnetic flux through the same coil. The aim is to compare the results obtained for different air gaps thicknesses with the face air gap model and with the volume air gap model.
Regarding the characteristics of the model:

- There will be two different material cases, a linear one with an isotropic linear material with $\mu_r = 1000$ and a second case with a nonlinear material that follows an isotropic analytical saturation of arc tangent type defined by two coefficients: $\mu_r = 1000$ and magnetization saturation of 1.2 T.

- The coil will have an imposed current of 1 A for the linear case and a set of currents $\{0.001, 0.01, 0.05, 0.1, 0.2\}$ A for the nonlinear case.

- The air gap widths tested will be of 20 μm and 50 μm.

- There will be three models, the air gap face model including the contribution of matrices $\mathbf{R_m}$ and $\mathbf{P_m}$ (called VIM face RP), the air gap face model only including the contribution of matrix $\mathbf{R_m}$ (called VIM face R) and the air gap volume model (called VIM volume). Since we don't have a reference, we will compare VIM face RP with VIM volume and VIM face R with VIM volume.

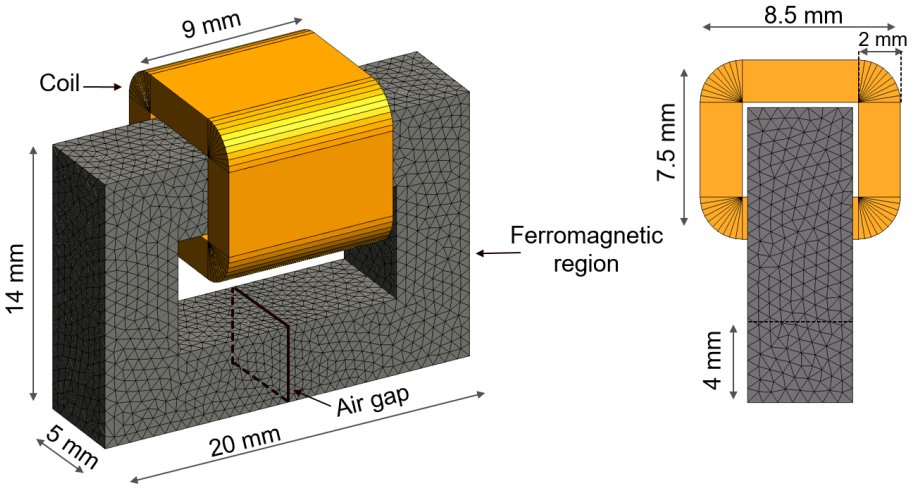

Figure II.20: Geometry of the academic case with a mesh of 40 000 elements.

The convergent mesh chosen has 40000 elements as Figure II.20 shows.
For the **linear case**, the flux through the coil for air gaps of thickness 20 μm and 50 μm and without air gap is given in Figure II.21a. We see that the flux decreases as the air gap thickness increases, which is logical because the air gap hampers the flux route through the ferromagnetic region and it disperses in the air.

Figure II.21b shows the relative difference between VIM volume and VIM face RP; and between VIM volume and VIM face R depending on the air gap thickness. We notice that both relative differences increase as the air gap gets thicker, where the VIM face RP model has less relative difference with VIM volume method than the VIM face R with VIM volume. This result suggest that VIM face RP is more accurate than VIM face R, as expected because we haven't considered one of the terms.

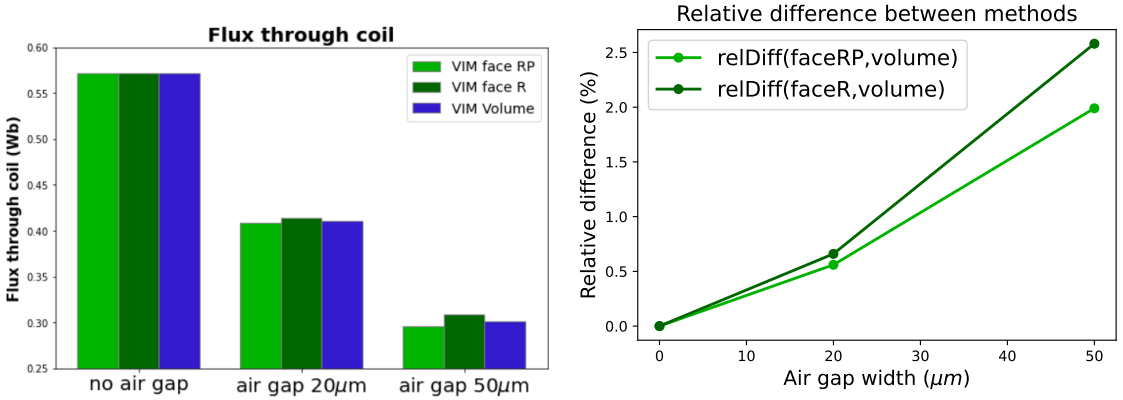

(a) Flux through coil.

(b) Relative difference between methods.

Figure II.21: Air gap results of the academic case, linear.

For the **nonlinear case**, the flux through the coil imposing the currents {0.001 , 0.01, 0.05, 0.1, 0.2} A for air gaps of thicknesses 20 μm and 50 μm and without air gap is given in Figure II.22a. We notice that without air gap the flux obtained is higher, and as the

air gap thickness increases the flux obtained is lower, obtaining less flux for an air gap of 20 μm of thickness and even less for an air gap of 50 μm. We also notice that the more the material saturates, the less impact the air gap has, obtaining values that are quite different for the two air gap thicknesses if the current is $\{0.001$, 0.01, 0.05, 0.1$\}$ A and a smaller difference between thicknesses when the imposed current is 0.2 A, for which the material is very saturated. The three methods provide results that are quite similar for each of the air gap thicknesses as we can see in Figure II.22a in which the three methods are overlapped (the three green lines and all the three blue lines are overlapped).

In order to notice the difference between methods for each of the two air gap thickness, Figure II.22b represents the relative difference between VIM volume method and VIM face RP method and between VIM volume method and VIM face R method. We see that the difference is higher for an air gap of 50 μm than for an air gap of 20 μm because the thicker the air gap, the less accurate the air gap method. We also notice that VIM face RP method is closer to VIM volume method than VIM face R, suggesting that VIM face RP is more accurate than VIM face R, as expected.

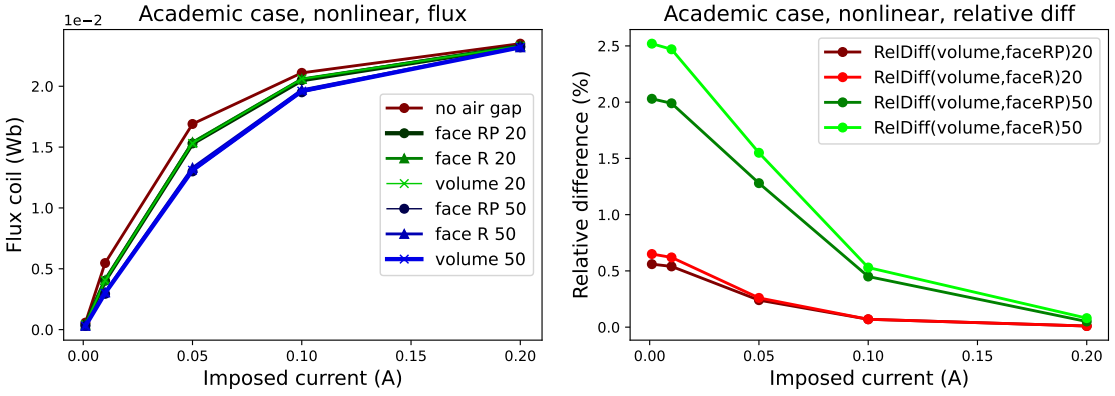

(a) Flux through coil.

(b) Relative difference between methods.

Figure II.22: Air gap results of the academic case, nonlinear.

II.3.b-ii NSX sensor

A second application for the air gap model is NSX sensor. As explained before, this sensor has three air gaps: two thin ones arising when two parts of the magnetic region are welded to be able to insert the secondary coil (Fig. II.23) and a large air gap that is consciously designed to force the electromagnetic flux to flow along A loop and not B loop represented in Fig. II.24.

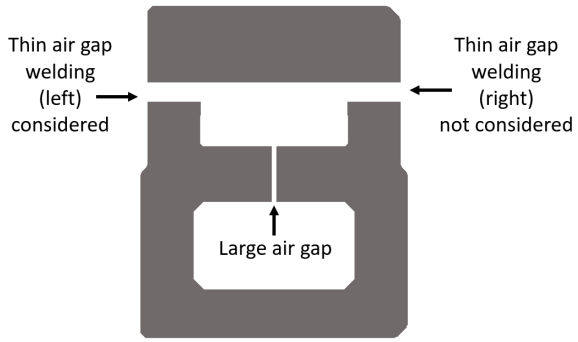

Figure II.23: NSX current transformer before welding to insert the secondary coil.

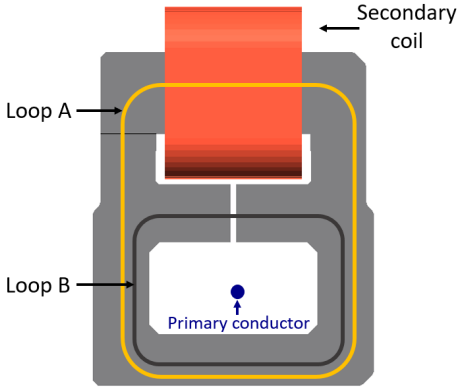

Figure II.24: NSX loop A forced by the large air gap.

The large air gap, with thickness 500 μm, is too large to apply the thin air gap development and it is simply meshed as a volume region of air, with no specific treatment. Some other considerations of this application are:

- We will study two different material cases, a linear one with an isotropic linear material of $\mu_r = 1000$ and a second case with a nonlinear material that follows an isotropic analytical saturation of arc tangent type defined by two coefficients: $\mu_r = 1000$ and magnetization saturation of 1.2 T.

- For simplicity, we will only consider the primary conductor and the secondary coil, which are enough to show the air gap effect, omitting the Rogowski coil.

- The primary conductor will have an imposed current of 1 A for the linear case and 100 A for the nonlinear case, for which the material is already saturated (as we have shown previously testing the magnetostatic formulation in Figure II.15).

- Three air gap thicknesses will be tested: 20 μm, 30 μm and 50 μm.

- Similarly to the academic case, we will run three models: VIM face RP, VIM face R and VIM volume, comparing VIM face RP with VIM volume and VIM face R with VIM volume.

- Calculations are done with a mesh of 46000 elements on the ferromagnetic region. An example of the air gap mesh when it is modeled as a volume element is shown in Figure II.25 for 50 μm of thickness, having 545 mesh elements.

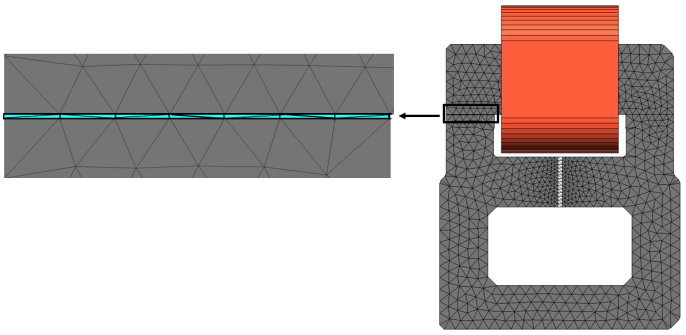

Figure II.25: NSX, air gap meshed as a volume region of thickness 50 μm.

For the **linear case**, the flux through the secondary coil imposing 1 A on the primary conductor is shown in Figure II.26a. We notice that the thicker the air gap, the more difference between models. Figure II.26b shows that the relative difference between VIM Face R and VIM volume is higher than the one between VIM RP and VIM volume, suggesting that VIM face RP is more accurate than VIM face R. The relative difference between methods increases as the air gap thickness does, having for instance a relative difference between VIM face RP and VIM Volume of 0.27 % for an air gap of 20 μm of thickness and 0.89 % for an air gap of 50 μm.

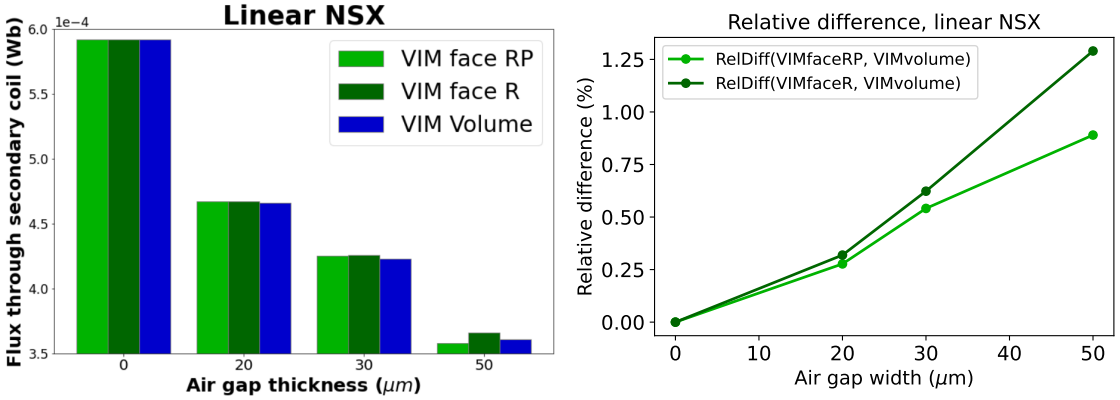

(a) Flux through secondary coil.

(b) Relative difference between methods.

Figure II.26: Linear results for NSX thin air gap

We repeat the same process for the **nonlinear material** obtaining the flux through the secondary coil in Figure II.27a and the relative difference between methods in Figure II.27b. We notice that the difference between methods is higher as the thickness of the air gap increases because one of the assumptions of the thin air gap model is that the thickness is small, and as it gets larger, the model is less accurate. For instance, the relative difference between VIM face RP and VIM volume is 0.13 % for an air gap of 20 μm and it increases to 0.55 % for an air gap of 50 μm.

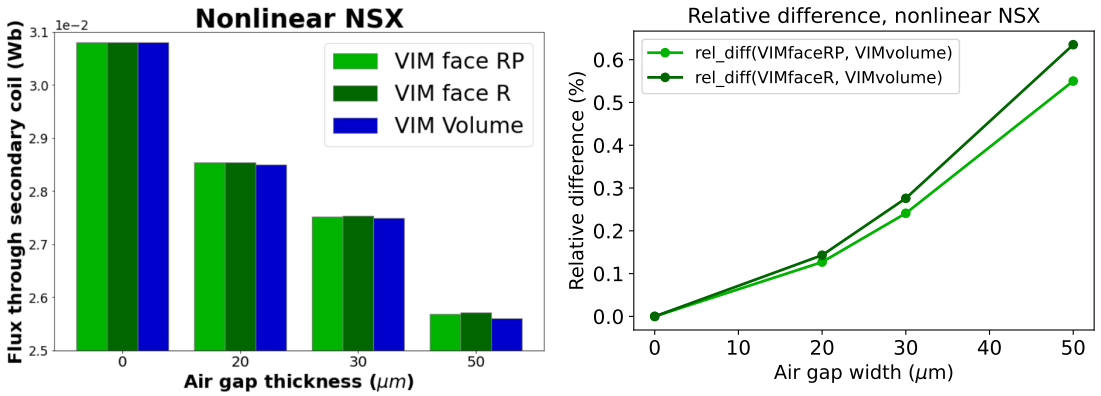

(a) Flux through secondary coil.

(b) Relative difference between models.

Figure II.27: Nonlinear results for NSX thin air gap

II.4 Conclusion

This chapter presents the magnetostatic volume integral formulation that is the basis of this thesis. The choice of a B-conforming formulation using facet elements is explained and the formulation is developed using an equivalent electric circuit approach. The matrix system of a general problem is shown on eq. (II.34) and it is formed of two main matrices that we name $\mathbf{R_m}$ and $\mathbf{P_m}$. $\mathbf{R_m}$ matrix holds the links between the internal elements of the ferromagnetic region and it is a finite element method matrix, which is sparse. $\mathbf{P_m}$ matrix provides the modelization of the flux exiting the magnetic material to the air, and it is fully populated. Then, the method used to compute the magnetic flux through coils is shown. The formulation is applied to the current transformer of NSX sensor and it is compared to the results of a FEM software. This application demonstrates that the developed formulation is suitable for the current sensor application that we needed, providing accuracy in the computation of the magnetic flux through coils.

The second part of the chapter is centred in modeling air gaps using the previously explained formulation, more precisely thin air gaps, which are difficult to model as a volume element given its narrow thickness. The concept behind the suggested approach is to mesh the air gaps as a face element and use a numerical procedure to prevent meshing it as a volume element. The method translates in adding a contribution to $\mathbf{R_m}$ and $\mathbf{P_m}$ matrices on the branches that cross the air gap. Then, two applications to an academic case and to the current transformer of NSX sensor are exhibited, comparing the face air gap model with the volume air gap model. The results show that the face air gap model is accurate for thin air gaps, but the thicker the air gap is, the less accurate the model happens to be, which is natural given the assumptions.

As a summary of these two parts, this chapter shows that we can model and obtain accurate results of current sensors for magnetostatic phenomena with nonlinear materials and air gaps.

Chapter III

Time stepping volume integral formulations for nonlinear field-circuit coupled problems

Summary

This chapter develops two different time stepping volume integral formulations for nonlinear field-circuit coupled problems. The first one is a weak coupling formulation in which the magnetic field and the circuit are treated separately in the time stepping process. For this case two algorithms are explained, one for linear materials and another one for nonlinear materials. The second formulation is a strong coupling formulation in which the magnetic field and the circuit equations are written together obtaining a system that treats both simultaneously and it is adapted to include circuit lumped elements. Both formulations are validated on NSX current sensor.

III.1 Introduction

Modeling the Rogowski metering coil isolated requires only the use of a magnetostatic volume integral method shown in chapter 2. However, this metering sensor interacts with other elements that require transient models. This is particularly important in the case of self-powered sensors, as we place a current transformer next to the Rogowski coil. Then, the secondary coil of the current transformer is linked to an external circuit and it is necessary to determine the currents flowing in this secondary coil. These currents have an impact on the operation of the current transformer and also on the whole current sensor formed by the Rogowski metering coil and the current transformer.

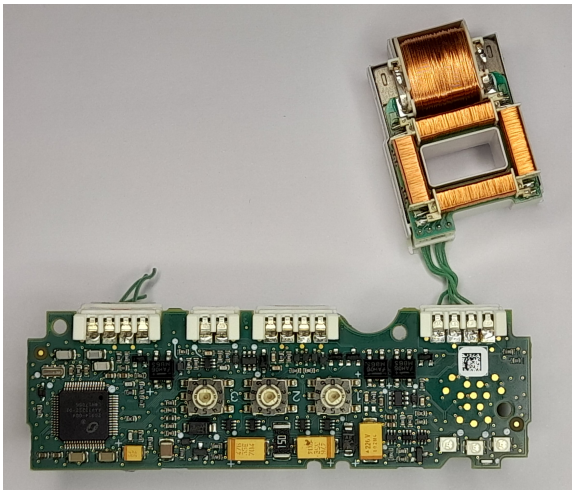

Figure III.1: NSX sensor connected to a PCB.

To account for this, there are two different possible scenarios:

1. **Harmonic regime**.
   Many harmonic formulations have already been developed using the VIM [52], for instance the Partial Element Equivalent Circuit (PEEC) that allows to analyse electromagnetic devices such as busbars, PCBs or integrated circuit interconnects. PEEC was introduced by A. E. Ruehli [51] and it has been extended to be used in conductive regions [55], for dielectric materials [56] and for magnetic ones [57]. Other applications include thin conductive shells coupled with external circuits [54] or inductive coupling in a transmission line right-of-way [58]. Nevertheless, the harmonic formulations have some limitations, being the main drawback that they cannot be applied to nonlinear problems. In addition, they can only be used for a source of sinusoidal waves. Therefore, they allow to simulate the current sensors that we are treating for low current and sinusoidal sources, without saturation of the material, but they don't model the nonlinear behaviour for higher current.

2. **Time-domain regime**.
   These methods are more time consuming than harmonic ones, since (at least) one

resolution of the system defining the problem has to be done at each time step. Their advantage is that they can be used in a wide variety of situations, such as considering nonlinear materials or sources of any shape (not limited to sinusoidal waves as it is the case of the harmonic regime). Unfortunately, the bibliography of time stepping formulations using the VIM is very limited. Indeed, it wasn't until a few years ago that the increase of memory and power of the computers, the advanced formulations and the matrix compression algorithms allowed to further develop the VIM, and static and harmonic regimes have been the main research focus the recent years. To our knowledge, there is no VIM formulation developed to deal with field-circuit coupling using a time stepping strategy.

In this chapter we extend the magnetostatic volume integral formulation of the previous chapter to a time stepping one for nonlinear non conductive ferromagnetic materials.

This will allow to obtain transient simulations of the current sensors of interest. We present the development of two methods:

1. The first one is a **weak field-circuit coupling**, meaning that the magnetic field simulation and the circuit one are treated as separate systems in the time stepping process. It is specifically adapted to current transformers, and well adapted to linear materials.

2. The second one is a **strong field-circuit coupling** which is a more general method where the field and circuit equations are written together to form an equation system, consequently they are solved simultaneously. It also allows to consider more elements in the external circuit such as voltage sources or resistive circuit elements.

Both methods are explained and validated with NSX sensor.

III.2 General problem definition

A generic problem is composed of the following elements: ferromagnetic non conductive regions Ω_{m} defined by a magnetic permeability $\mu(\mathbf{H})$ and inductive coils Ω_{c} characterized by a current density $\mathbf{j_c}$ that are split in two categories: those with a current flowing through them and the ones linked to an external circuit coupled with lumped elements such as current sources, voltage sources or resistive circuit elements. Figure III.2 shows a representation of it.

The formulation is based on the time dependant Maxwell's equations, let us state them.

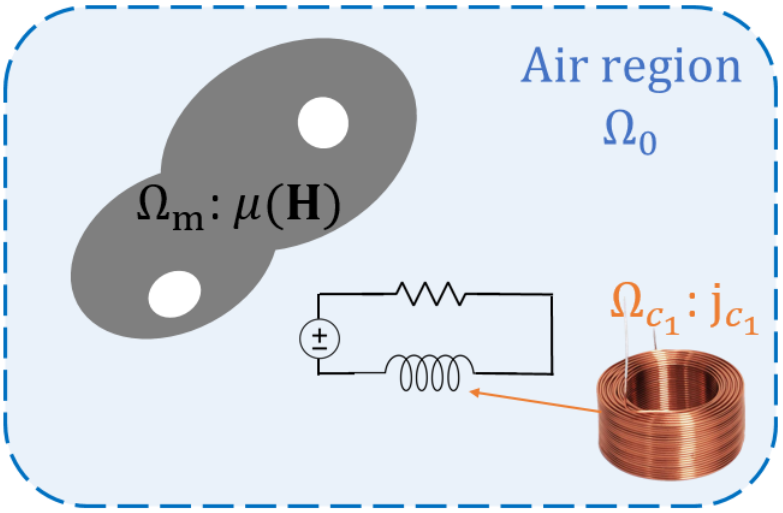

Figure III.2: Representation of a general problem definition for strong field-circuit coupling.

III.2.a Time dependant Maxwell's equations and constitutive law

The time dependant macroscopic Maxwell's equations in differential form are the following:

– Gauss's law:

$$\nabla \cdot \mathbf{D} = \rho \tag{III.1}$$

– Ampere's law:

$$\nabla \times \mathbf{H} = \mathbf{j}_c + \frac{\partial \mathbf{D}}{\partial t} \tag{III.2}$$

– Gauss's law for electromagnetism:

$$\nabla \cdot \mathbf{B} = 0 \tag{III.3}$$

– Maxwell's-Faraday's law:

$$\nabla \times \mathbf{E} = -\frac{\partial \mathbf{B}}{\partial \mathrm{t}} \tag{III.4}$$

where $\mathbf{D}$ is the electric displacement field (C/m^2),
ρ is the electric charge density (C/m^3),
$\mathbf{H}$ is the magnetic field (A/m),
$\mathbf{j}_c$ is the electric current density (A/m^2),
$\mathbf{B}$ is the magnetic field (T) and
$\mathbf{E}$ is the electric field (V/m).

In our case, we do not consider electric displacement field, therefore $\mathbf{D} = 0$. Furthermore, we only work with non conductive regions, being only magnetic.
The magnetic field part of the formulation will use the static equations:

$$\begin{cases} \nabla \times \mathbf{H} = \mathbf{j}_c \\ \nabla \cdot \mathbf{B} = 0. \end{cases} \tag{III.5}$$

whereas the circuit part will consider Maxwell's-Faraday's law.

The constitutive law allows to write a relation between the magnetic field $\mathbf{H}$ and the magnetic induction $\mathbf{B}$. We consider the coercive field to obtain the following relation:

$$\mathbf{H}(\mathbf{B}) = \nu(\mathbf{B})\mathbf{B} + \mathbf{H_c} \tag{III.6}$$

where ν is the reluctivity of the material and $\mathbf{H_c}$ is the coercive field of the magnetic materials.

III.3 Weak field-circuit coupling

This case is specifically designed to be used in the field-circuit coupling of a current transformer with a core, a primary conductor and a secondary coil, which is our case of interest to model current sensors. We have only developed it for the situation in which the secondary coil has an external circuit with a resistance R as Figure III.3 shows for a specific current transformer. We consider that the primary conductor is a current source, and that the current flowing through it is not perturbed by the secondary coil. The development is based on the magnetostatic formulation of chapter 2 and it depends on the nature of the material, that can be linear or nonlinear.

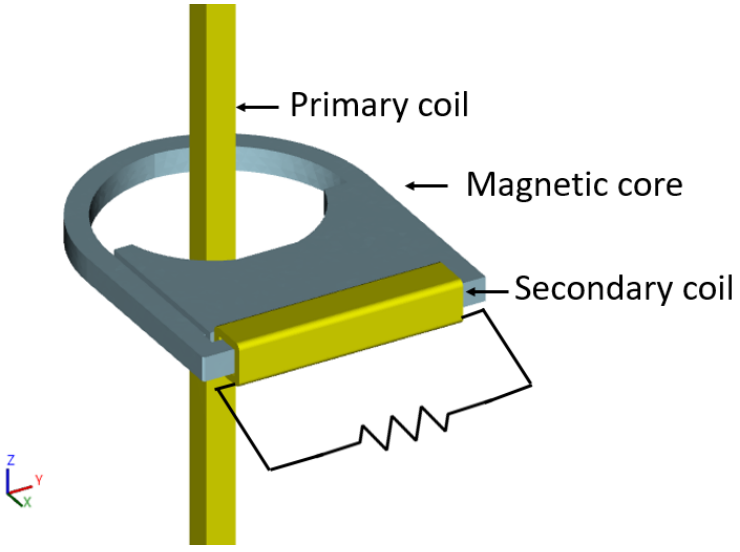

Figure III.3: Example of a case to apply the weak field-circuit coupling formulation.

III.3.a Weak field-circuit coupling for linear materials

Let us consider a ferromagnetic core with a linear material. The idea is to obtain the current through the secondary coil I_s given that there is a field-circuit coupling with the primary conductor in which there is an imposed current I_p that is known.
The time variable t is observed in a simulation time range $[0, T]$ divided in N intervals of the same length Δt: $t = [t_0, t_1, ..., t_N] = [0, \Delta t, 2\Delta t, 3\Delta t, ..., N\Delta t]$.

For linear materials, the magnetic flux through the secondary coil Ω_c is computed as:

$$\Phi_{\Omega_c} = M_p \mathrm{I}_p + M_s \mathrm{I}_s \tag{III.7}$$

where

$$M_p = \Phi_{\Omega_c}|_{\mathrm{I}_p=1;\mathrm{I}_s=0} \qquad M_s = \Phi_{\Omega_c}|_{\mathrm{I}_p=0;\mathrm{I}_s=1} \tag{III.8}$$

that is to say, the magnetic flux through the coil given that the primary current I_p is 1 A and the secondary current I_s is 0 A; or 0 A on the primary current and 1 A on the secondary current respectively. These two values can be computed only one time for the whole simulation and they can be used at each step, multiplying them by I_p and I_s to compute the flux through the coil. The magnetic flux is computed using the VIM magnetostatic formulation explained in chapter 2.

Given Faraday's law, the voltage induced in the secondary coil is $e = -\frac{\mathrm{d}\Phi_{\Omega_c}}{\mathrm{d}t}$. Now, applying Ohm's law to the circuit of the secondary coil:

$$R\mathrm{I}_s^t = -\frac{\mathrm{d}\Phi_{\Omega_c}}{\mathrm{d}t} \approx -\frac{\Phi_{\Omega_c}^t - \Phi_{\Omega_c}^{t-1}}{\Delta t} = -\frac{M_p \mathrm{I}_p^t + M_s \mathrm{I}_s^t - \Phi_{\Omega_c}^{t-1}}{\Delta t} \tag{III.9}$$

where the superscript t indicates that the function is evaluated at time step t for $t = t_1, ..., t_N$ and $t - 1 = t - \Delta t$. The resistance R is the sum of the resistance component of the circuit and the resistance of the winding of the secondary coil. Finally, the current of the secondary coil at time step t is approximated by:

$$\mathrm{I}_s^t \approx -\frac{M_p \mathrm{I}_p^t - \Phi_{\Omega_c}^{t-1}}{\Delta t R + M_s} = -\frac{M_p \mathrm{I}_p^t - (M_p \mathrm{I}_p^{t-1} + M_s \mathrm{I}_s^{t-1})}{\Delta t R + M_s}. \tag{III.10}$$

Let us notice that this is an explicit formula given that I_p^t, M_p and M_s are known and the value of I_s^{t-1} has been computed in the previous time step. The latter expression (III.10) is the one that we have coded to obtain the secondary current. A pseudocode is presented in Algorithm 1.

Algorithm 1 weak field-circuit coupling for linear materials

Require: I_p
  $t \leftarrow t_0$
  $\mathrm{I}_s^{t_0} \leftarrow 0$
  $\Phi_{\Omega_\mathrm{c}}^{t_0} \leftarrow \Phi_{\Omega_\mathrm{c}}(\mathrm{I}_p^{t_0}, 0)$
  $M_p \leftarrow \Phi_{\Omega_\mathrm{c}}(1, 0)$
  $M_s \leftarrow \Phi_{\Omega_\mathrm{c}}(0, 1)$
  $t \leftarrow t_1$
  while $t \leq T$ **do**
    $\mathrm{I}_s^t = -\frac{M_p \mathrm{I}_p^t - (M_p \mathrm{I}_p^{t-1} + M_s \mathrm{I}_s^{t-1})}{\Delta t R + M_s}$
    $t \leftarrow t + \Delta t$
  end while
  return I_s^t for $t = \{t_0, t_1, ..., t_N\}$

This is the method used for linear materials. Let us now introduce the development made for nonlinear materials.

III.3.b Weak field-circuit coupling for nonlinear materials

The previous method is not valid for nonlinear materials given that the computation of the magnetic flux through the secondary coil cannot be computed following (III.7) when the ferromagnetic materials saturate. This section develops a weak field-circuit coupling formulation for nonlinear materials.

Let us start with Ohm's and Faraday's law:

$$R\mathrm{I}_s^t = -\frac{\mathrm{d}\Phi_{\Omega_\mathrm{c}}}{\mathrm{d}t}. \tag{III.11}$$

The Newton-Raphson method is considered, defining a residual Res as:

$$\mathrm{Res}(\mathrm{I}_s^{t,i}) = R\mathrm{I}_s^{t,i} + \frac{\Phi_{\Omega_\mathrm{c}}^{t,i}(\mathrm{I}_p^t, \mathrm{I}_s^{t,i}) - \Phi_{\Omega_\mathrm{c}}^{t-1}(\mathrm{I}_p^{t-1}, \mathrm{I}_s^{t-1})}{\Delta t}, \tag{III.12}$$

where the superscript t refers to the time step, the superscript i corresponds to the Newton-Raphson nested loop and the magnetic flux Φ_{Ω_c} through the secondary coil is computed using the magnetostatic VIM formulation developed in chapter 2. Now, for the Newton-Raphson method we have to write:

$$\left.\frac{\partial \mathrm{Res}(\mathrm{I})}{\partial \mathrm{I}}\right|_{\mathrm{I}=\mathrm{I}_s^{t,i-1}} (\mathrm{I}_s^{t,i} - \mathrm{I}_s^{t,i-1}) = -\mathrm{Res}(\mathrm{I}_s^{t,i-1}). \tag{III.13}$$

The partial derivative of the residual is computed as:

$$\left.\frac{\partial \mathrm{Res}(\mathrm{I})}{\partial \mathrm{I}}\right|_{\mathrm{I}=\mathrm{I}_s^{t,i-1}} = R + \frac{1}{\Delta t}\left.\frac{\partial \Phi_{\Omega_\mathrm{c}}(\mathrm{I})}{\partial \mathrm{I}}\right|_{\mathrm{I}=\mathrm{I}_s^{t,i-1}}. \tag{III.14}$$

Then, using the expression of the derivative (III.14) and the definition of the residual (III.12) in (III.13), the Newton-Raphson expression reads:

$$\left(R+\frac{1}{\Delta t}\frac{\partial\Phi_{\Omega_c}(\mathrm{I})}{\partial \mathrm{I}}\bigg|_{\mathrm{I}=\mathrm{I}_s^{t,i-1}}\right)(\mathrm{I}_s^{t,i}-\mathrm{I}_s^{t,i-1})=-\left(R\mathrm{I}_s^{t,i-1}+\frac{\Phi_{\Omega_c}^{t,i-1}-\Phi_{\Omega_c}^{t-1}}{\Delta t}\right). \tag{III.15}$$

In order to compute $\frac{\partial\Phi_{\Omega_c}(\mathrm{I})}{\partial \mathrm{I}}\Big|_{\mathrm{I}=\mathrm{I}_s^{t,i-1}}$, we consider an approximation with the previous step with respect to i, having:

$$\frac{\partial\Phi_{\Omega_c}(\mathrm{I})}{\partial \mathrm{I}}\bigg|_{\mathrm{I}=\mathrm{I}_s^{t,i-1}}=\frac{\Phi_{\Omega_c}^{t,i-1}-\Phi_{\Omega_c}^{t,i-2}}{\mathrm{I}_s^{t,i-1}-\mathrm{I}_s^{t,i-2}}. \tag{III.16}$$

Injecting the latter expression in (III.15), the Newton-Raphson expression is written:

$$\left(R+\frac{1}{\Delta t}\frac{\Phi_{\Omega_c}^{t,i-1}-\Phi_{\Omega_c}^{t,i-2}}{\mathrm{I}_s^{t,i-1}-\mathrm{I}_s^{t,i-2}}\right)(\mathrm{I}_s^{t,i}-\mathrm{I}_s^{t,i-1})=-\left(R\mathrm{I}_s^{t,i-1}+\frac{\Phi_{\Omega_c}^{t,i-1}-\Phi_{\Omega_c}^{t-1}}{\Delta t}\right). \tag{III.17}$$

Finally, isolating the secondary current at time step t and iteration i:

$$\boxed{\mathrm{I}_s^{t,i}=\mathrm{I}_s^{t,i-1}-\frac{\mathrm{Res}(\mathrm{I}_s^{t,i-1})}{\mathrm{B}}} \tag{III.18}$$

where

$$\mathrm{Res}(\mathrm{I}_s^{t,i-1})=R\mathrm{I}_s^{t,i}+\frac{\Phi_{\Omega_c}^{t,i-1}-\Phi_{\Omega_c}^{t-1}}{\Delta t}, \tag{III.19}$$

$$\mathrm{B}=R+\frac{1}{\Delta t}\frac{\Phi_{\Omega_c}^{t,i-1}-\Phi_{\Omega_c}^{t,i-2}}{\mathrm{I}_s^{t,i-1}-\mathrm{I}_s^{t,i-2}}. \tag{III.20}$$

The latter expression provides the current flowing through the secondary coil when there is a field-circuit coupling with a resistance and the magnetic core has nonlinear behaviour. A pseudocode is shown in Algorithm 2.

In order to obtain a better convergence rate, a line search strategy is considered [63]. For each $\mathrm{I}_s^{t,i}$, the line search value $\mathrm{I}_s^{t,i*}$ is computed such that

$$\mathrm{I}_s^{t,i*}=\mathrm{I}_s^{t,i-1}+\alpha\Delta\mathrm{I}_s^{t,i}=\mathrm{I}_s^{t,i-1}+\alpha(\mathrm{I}_s^{t,i}-\mathrm{I}_s^{t,i-1}) \tag{III.21}$$

for three values of α that are equidistant $\alpha=\{1/3,2/3,1\}$, keeping as $\mathrm{I}_s^{t,i}$ the $\mathrm{I}_s^{t,i*}$ value obtained with the α that minimizes more the residual (III.12). To speed the computations, the same α obtained is used for the next four i iterations.

As a final remark, we have imposed that the Newton-Raphson method has converged when the difference between two consecutive i iterations is inferior to 10^{-10}.

An application case is considered to test the accuracy of the two models explained for weak field-circuit coupling.

Algorithm 2 weak field-circuit coupling for nonlinear materials

Require: $\mathrm{I_p}$
  $t \leftarrow t_0$
  $i \leftarrow 0$
  $\epsilon \leftarrow 10^{-10}$
  $\mathrm{I}_s^{t_0}, \mathrm{I}_s^{t_1,0}, \mathrm{I}_s^{t_1,1} \leftarrow 0$
  $\Phi_{\Omega_c}^{t_0} \leftarrow \Phi_{\Omega_c}(\mathrm{I}_p^0, 0)$
  $\Phi_{\Omega_c}^{t_1,0}, \Phi_{\Omega_c}^{t_1,1} \leftarrow 0$
  while $t \leq T$ **do**
    while $(\mathrm{I}_s^{t,i} - \mathrm{I}_s^{t,i-1}) \geq \epsilon$ **do**
      Find $\mathrm{I}_s^{t,i+1}$ with expression (III.18)
      $i \leftarrow i + 1$
    end while
    $t \leftarrow t + \Delta t$
  end while
  return I_s^t for $t = \{t_0, t_1, ..., t_N\}$

III.3.c Application to NSX current sensor

Let us apply the weak field-circuit coupling method developed for linear and nonlinear materials to NSX current sensor. To validate the models, we will compare them with the software Flux3D of Altair that also implements a field-circuit coupling, which will be the reference.

Regarding NSX model, we consider the current transformer, given that the secondary coil is connected to a circuit and there will be field-circuit coupling and we do not keep the Rogowski metering coil for this test.

The secondary coil has an external circuit with a resistance of 63 Ω as shown in Figure III.4, it is there that the field-circuit coupling will arise.

The characteristics of the model are the following:

- The ferromagnetic region follows an isotropic linear material of μ_r =1000 for the linear case and an isotropic analytic saturation of arc tangent type with two coefficients μ_r =1000 and saturation magnetization = 1.2 T for the nonlinear case.
- The primary conductor has imposed current of $\mathrm{I}_p = 300\sin(2\pi f t)$, where f is the frequency, which we set to 50 Hz, and t is the time. This conductor is again defined as a closed loop of dimension 1 meter times 1 meter as explained in the magnetostatic case for simulation accuracy purposes (Figure II.11), to avoid to perceive the return of the conductor.
- The secondary coil has 980 turns and no imposed current. It is linked to an external circuit that has a resistance of 63 Ω.
- The output is the current through the secondary coil.

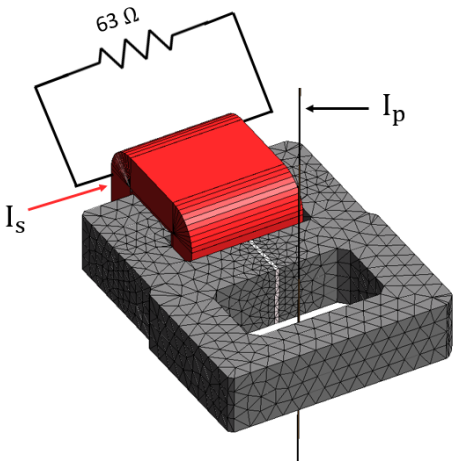

Figure III.4: weak field-circuit coupling model for NSX, mesh 12000 elements.

The mesh considered for this simulation is the most coarse that we showed in the magnetostatic case, which consists in 12000 elements. We have chosen this mesh to have the same for the weak coupling of the linear and nonlinear case, and it is the simulation time of the nonlinear case that limits the mesh, although for the linear case computations are considerably faster. The simulation is made for 3 time periods, and given that the frequency is 50 Hz, the time interval of the simulation is $t \in [0, 0.6]$. We use a fixed time step of $\Delta t = 0.0004$ s, therefore there are 150 time steps in total, 50 per period.

Figure III.5 shows the result for the **linear material**, providing the current through the secondary coil for the explained parameters. The black line represents the reference and the green line displays the developed method called VIM weak which stands for VIM weak field-circuit coupling, both of them correspond to the left y-axis. The blue line shows the difference between the two methods for each point divided over the maximum value of the reference, and it is linked to the right y-axis.

We see that the difference between the methods is inferior to 0.6 %, which validates the weak field-circuit coupling model for linear materials. Regarding the computation time, the implemented model is remarkably fast, taking 50 seconds, given that it only needs two resolutions of the system for the whole transient simulation. The reference took 2h 10 minutes because it solves the system defining the problem at each time step.

We conclude that the weak field-circuit coupling method is accurate in the results and it is much faster than the reference. However, it is restricted to problems with the topology defined in Figure III.3.

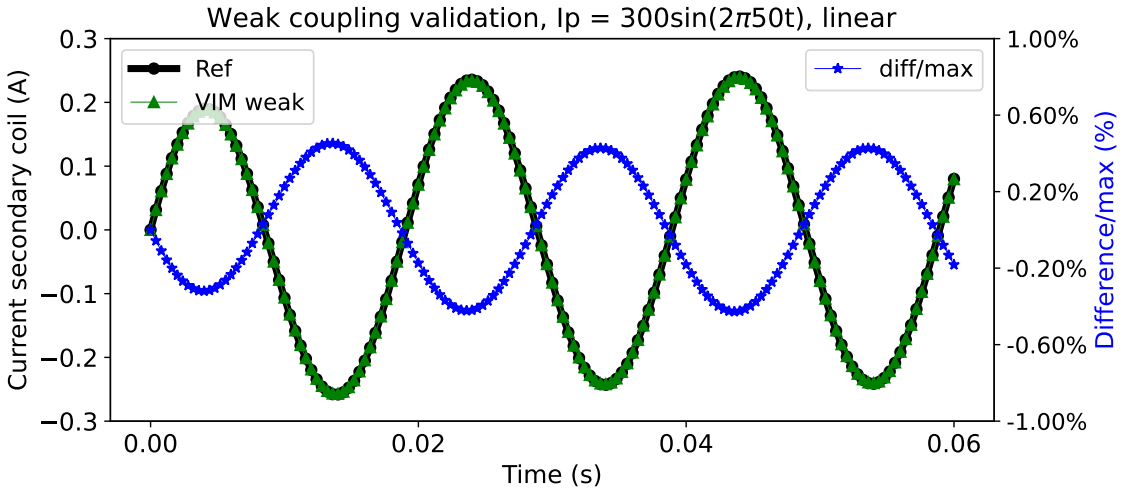

Figure III.5: Weak field-circuit coupling model validation for NSX, linear case.

The validation of the weak field-circuit coupling for **nonlinear materials** is shown in Figure III.6. Again, on the left y-axis the reference is represented with a black line and our developed method, called VIM weak, in green. On the right y-axis we plot the difference point by point divided over the maximum value of the reference, in blue.

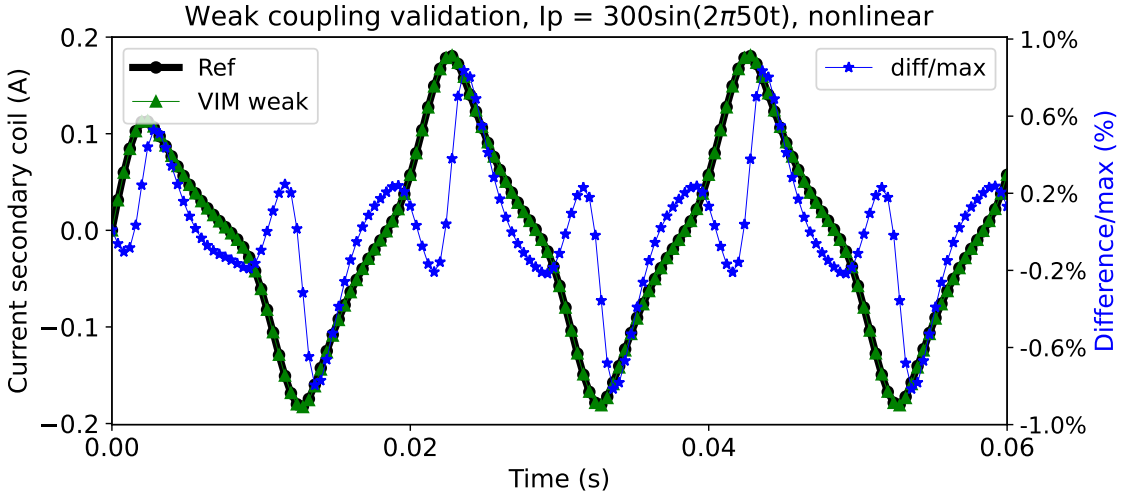

Figure III.6: Weak field-circuit coupling model validation for NSX, nonlinear case.

This difference over the maximum is inferior to 1 %, which validates the model. Nevertheless, in terms of computation time, the difference between the methods is not negligible. The reference took 45 hours whereas our implemented method took 70 hours. This is partially due to the multiple evaluations needed for the line search strategy, which could be optimized to reduce the time. In conclusion, the weak VIM field-circuit coupling is validated with the reference given the low difference between both methods, but the computation time is considerably longer.

As summary, two methods for the weak field-circuit coupling have been developed, one for linear materials and another one for nonlinear materials. When tested on a current transformer, they have both shown accuracy, obtaining less than 1 % difference with respect to the reference. Nevertheless, in terms of time, only the linear case is efficient, reducing considerably the computation time of the reference.

Once the weak field-circuit coupling has been explained, let us describe the strong one.

III.4 Strong field-circuit coupling

The strong field-circuit coupling method allows to write a system with both the magnetic field and the circuit equations to solve them together. This method has been developed in a more general setting that the weak field-circuit coupling previously presented, being adapted to include more elements in the external circuit, such as voltage sources or capacitors.

III.4.a Time stepping field-circuit coupled formulation for volume regions with circuit coils

This formulation is the assembly of two different types of equations:

1. The equations defining the contribution of the magnetic field.
2. The equations describing the contribution of the electric circuit, linking the currents and the voltages of the coils.

Each of them is explained separately to after gather them in a system.

III.4.a-i Magnetic field contribution

Let us start decomposing $\mathbf{H}$ by the reduced field generated by the ferromagnetic materials $\mathbf{H_r}$ and the magnetic field created by the circuit coils $\mathbf{H_b}$:

$$\mathbf{H} = \mathbf{H_r} + \mathbf{H_b}. \tag{III.22}$$

A reduced magnetic scalar potential φ_r can be written as:

$$\mathbf{H_r} = -\nabla\varphi_\mathbf{r}. \tag{III.23}$$

Thus, the magnetic field can be expressed as:

$$\mathbf{H} = -\nabla\varphi_\mathbf{r} + \mathbf{H_b}. \tag{III.24}$$

The magnetic field created by circuit coils $\mathbf{H_b}$ can be discretized:

$$\mathbf{H_b} = \sum_k \mathbf{h_{b}}_k \mathbf{I_{b}}_k \tag{III.25}$$

where $\mathbf{h_{b}}_k$ is the magnetic field created by coil k with current 1 A and $\mathbf{I_{b}}_k$ is the current flowing on coil k.

Now, a discretization of the ferromagnetic domain is considered, subdividing it into N_v volume elements that form the primal mesh and N_f facet elements, which correspond to the number of branches of the dual mesh (Figure III.7). Then, facet-shape functions associated to that mesh (as explained in section II.2.c-i) are taken, and induction $\mathbf{B}$ is discretized with these functions $\mathbf{w}_j$ such that:

$$\mathbf{B} = \sum_{j=1}^{N_f} \mathbf{w}_j \Phi_j \tag{III.26}$$

where Φ_j is the magnetic flux across facet j, which corresponds to the branches of the dual mesh.

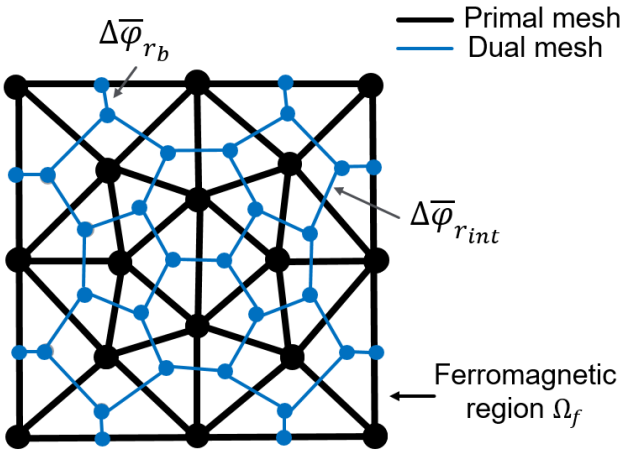

Figure III.7: Primal and dual mesh of a ferromagnetic region with the infinity node.

Making use of the constitutive relation and the discretization of $\mathbf{B}$ on equation (III.24):

$$\nu(\mathbf{B}) \sum_{j=1}^{N_f} \mathbf{w}_j \Phi_j = -\nabla\varphi_\mathbf{r} + \mathbf{H_b} - \mathbf{H_c}. \tag{III.27}$$

where we remind that $\mathbf{H_c}$ is the coercive field of the magnetic materials.

For the contribution of the **internal branches**, let us project the latter equation with facet-shape functions $\mathbf{w}_i$ (Galerkin projection) as we did in the magnetostatic case in chapter 2, the discretization of $\mathbf{H_b}$ and the strategy followed in section II.2.c-iii for $\nabla\varphi_\mathbf{r}$ to obtain:

$$\mathbf{R_m}\Phi + \mathbf{L_{mb}}\mathbf{I_b} = \Delta\overline{\varphi}_r + \mathbf{U}^{\mathbf{H_c}} \tag{III.28}$$

where

$$\mathrm{R}_{\mathrm{m}_{ij}} = \int_{\Omega_\mathrm{m}} \mathbf{w}_i \cdot \nu(\mathbf{B}) \mathbf{w}_j \mathrm{d}\Omega_\mathrm{m}, \tag{III.29}$$

$$\mathrm{L}_{\mathrm{mb}_{ik}} = -\int_{\Omega_m} \mathbf{w}_i \cdot \mathbf{h}_{\mathbf{b}_k} \mathrm{d}\Omega_\mathrm{m}, \tag{III.30}$$

$$\Delta\overline{\varphi}_r = \begin{pmatrix} \Delta\overline{\varphi}_{r_{int}} \\ \Delta\overline{\varphi}_{r_b} \end{pmatrix} \tag{III.31}$$

is the average potential difference between two elements that are inside the magnetic region (int) or between an internal element and a boundary element (b) and $\mathbf{U}^{\mathrm{H_c}}$ is a term coming from the coercive field

$$\mathbf{U}_i^{\mathrm{H_c}} = -\int_{\Omega_\mathrm{m}} \mathbf{w}_i \cdot \mathbf{H_c} \mathrm{d}\Omega_\mathrm{m}. \tag{III.32}$$

The system has to be completed to consider **the contribution of the flux exiting the magnetic region**, going to the infinity point (Figure III.8).

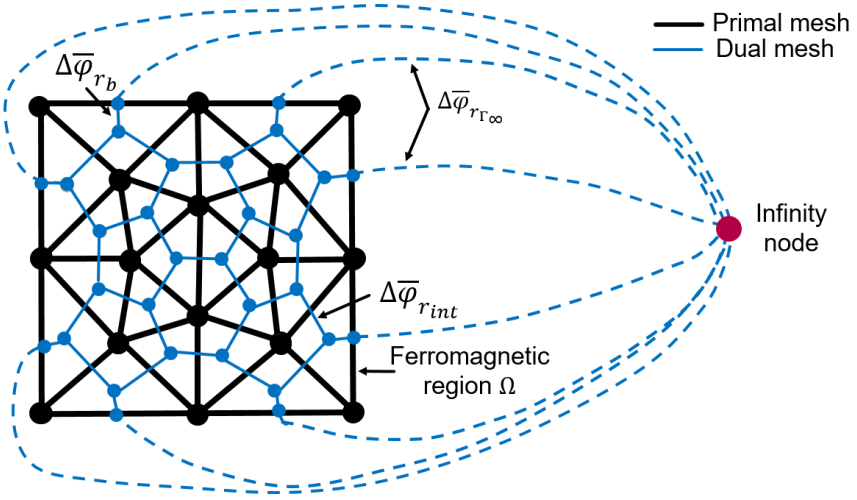

Figure III.8: Primal and dual mesh of a ferromagnetic region with the infinity node.

To that aim, we write the magnetic potential φ_r in terms of the magnetization $\mathbf{M}$:

$$\varphi_r = \frac{1}{4\pi}\int_{\Omega_\mathrm{m}} \mathbf{M} \cdot \nabla\left(\frac{1}{r}\right) \mathrm{d}\Omega_\mathrm{m}, \tag{III.33}$$

where r is the distance between the evaluation point of φ_r and the integration point in Ω_m. Let us assume a constant reluctivity per mesh element to be able to use the divergence theorem on the previous equation. Then, taking into account that the magnetization is defined as $\mathbf{B} = \mu_0(\mathbf{H}+\mathbf{M})$, it can be expressed by $\mathbf{M} = (\nu_0 - \nu(\mathbf{B}))\mathbf{B} + \mathbf{H_c}$, and an approximation of φ_r can be written using the divergence theorem on the first part of the equation:

$$\varphi_\mathrm{r} \approx \frac{1}{4\pi}\sum_j \int_{\Gamma_\mathrm{j}} \frac{\delta\nu_j \mathbf{B}\cdot\mathbf{n}}{r}\mathrm{d}\Gamma_j + \frac{1}{4\pi}\int_{\Omega_\mathrm{m}} \mathbf{H_c}\cdot\nabla\left(\frac{1}{r}\right)\mathrm{d}\Omega_\mathrm{m}, \tag{III.34}$$

where $\delta\nu_j$ is the reluctivity difference of the two elements that share facet j or $(\nu_j - \nu_0)$ if facet j belongs to the border of the ferromagnetic region. Using the definition of the magnetic flux passing through a surface of area S_j, φ_r approximation reads:

$$\varphi_\mathrm{r} \approx \frac{1}{4\pi}\sum_j \int_{\Gamma_j} \frac{1}{S_j}\frac{\delta\nu_j}{r}\mathrm{d}\Gamma_j\Phi_j + \frac{1}{4\pi}\int_{\Omega_\mathrm{m}} \mathbf{H_c}\cdot\nabla\left(\frac{1}{r}\right)\mathrm{d}\Omega_\mathrm{m}. \tag{III.35}$$

Then, assuming null potential at the infinity node, the average potential of the external facets that are going to the infinity point, named $\overline{\varphi}_{r_{\Gamma_i\infty}}$, is computed by:

$$\overline{\varphi}_{r_{\Gamma_i\infty}} = \frac{1}{S_i}\int_{\Gamma_{ext}} \varphi_r \mathrm{d}\Gamma_{ext}, \tag{III.36}$$

where the over line means average and Γ_{ext} refers to the external branches, which are the ones going from the border of the magnetic region to the infinity point, Fig. III.8.
The potential difference between the average potential of the external facets in matrix form reads:

$$\Delta\overline{\varphi}_{r_{\Gamma_i\infty}} = \mathbf{P_m}\Phi + \mathrm{U^I} \tag{III.37}$$

where

$$\mathrm{P_{m}}_{ij} = \frac{1}{4\pi}\int_{\Gamma_{ext_i}} \frac{1}{S_i}\left(\int_{\Gamma_j}\frac{1}{S_j}\frac{\delta\nu_j}{r}\mathrm{d}\Gamma_j\right)\mathrm{d}\Gamma_i, \tag{III.38}$$

$$\mathrm{U}_i^{\mathrm{I}} = \frac{1}{4\pi}\int_{\Gamma_{ext_i}} \frac{1}{S_i}\left(\int_{\Omega_\mathrm{m}} \mathbf{H_c}\cdot\nabla\left(\frac{1}{r}\right)\mathrm{d}\Omega_\mathrm{m}\right)\mathrm{d}\Gamma_i. \tag{III.39}$$

Let us notice that matrix $\mathbf{P_m}$ links the external branches with the rest of the branches, it has rectangular shape and it is similar to the one obtained in the magnetostatic case.

Finally, **combining the contribution of the internal branches and the branches linked to the infinity point**, the general system for the magnetic field contribution writes:

$$\boxed{\mathbf{R_m}\Phi + \mathbf{P_m}\Phi + \mathbf{L_{mb}}\mathbf{I_b} = \Delta\overline{\varphi}_\mathrm{r} + \mathbf{U_m}} \tag{III.40}$$

where

$$\Delta\overline{\varphi}_r = \begin{pmatrix} \Delta\overline{\varphi}_{r_{int}} \\ \Delta\overline{\varphi}_{r_b} + \Delta\overline{\varphi}_{r_{\Gamma_i\infty}} \end{pmatrix}, \tag{III.41}$$

$$\mathbf{U_m} = \mathbf{U^{H_c}} + \begin{pmatrix} \mathbf{0} \\ \mathbf{U^I} \end{pmatrix} \tag{III.42}$$

the contribution of the branches going from the interior of the magnetic region to a boundary element have been added with the branches going from the boundary to the infinity point. This is the reason why we see on the vector $\Delta\overline{\varphi}_r$ the sum of $\Delta\overline{\varphi}_{r_b}$ and $\Delta\overline{\varphi}_{r_{\Gamma_i\infty}}$, finally having the mesh representation of Figure III.9, which merges the boundary and infinity point branches, calling them external branches.

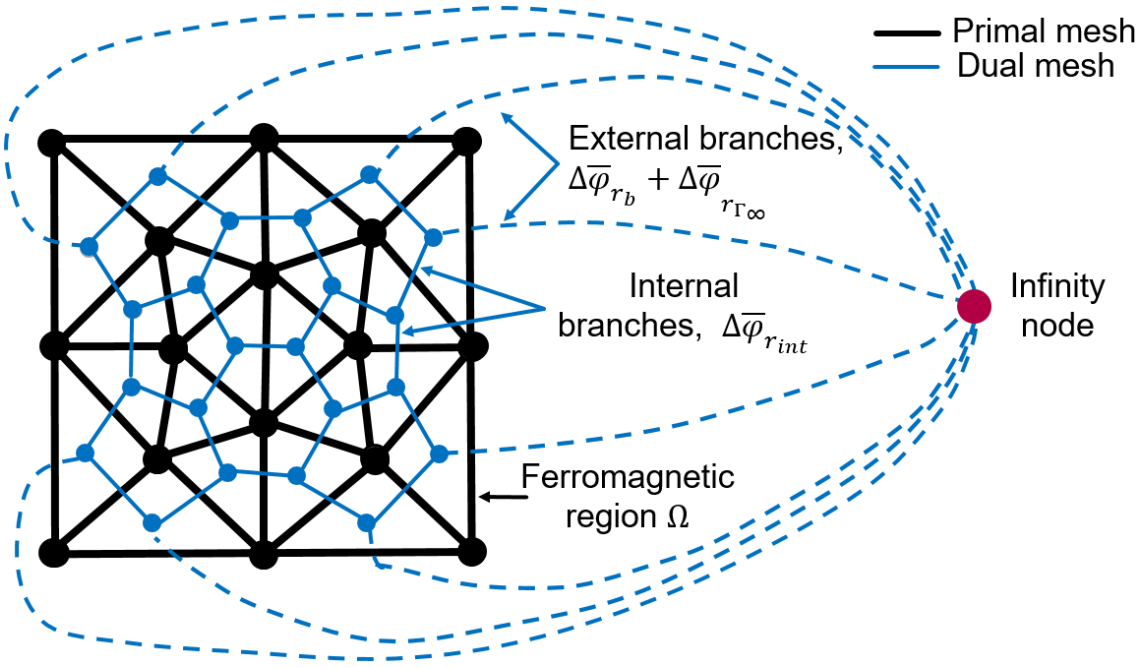

Figure III.9: Primal and dual mesh representation.

The size of $\mathbf{R_m}$ and $\mathbf{P_m}$ matrices is represented in Figure III.10 for linear and nonlinear problems. If the problem is linear, $\mathbf{P_m}$ matrix will be null for all the internal branches because $\delta\nu_j$ is 0, being non null only for the external branches and the branches that go between regions of a different reluctivity. For nonlinear problems $\mathbf{P_m}$ matrix is fully populated and rectangular. We remind that N_f the number of all the branches, and we call N_{fINT} the number of internal branches of the ferromagnetic regions, N_{fEXT} the number of external branches, which are going to the infinity point and N_{fBET} the number of branches that are between two regions of different reluctivity.

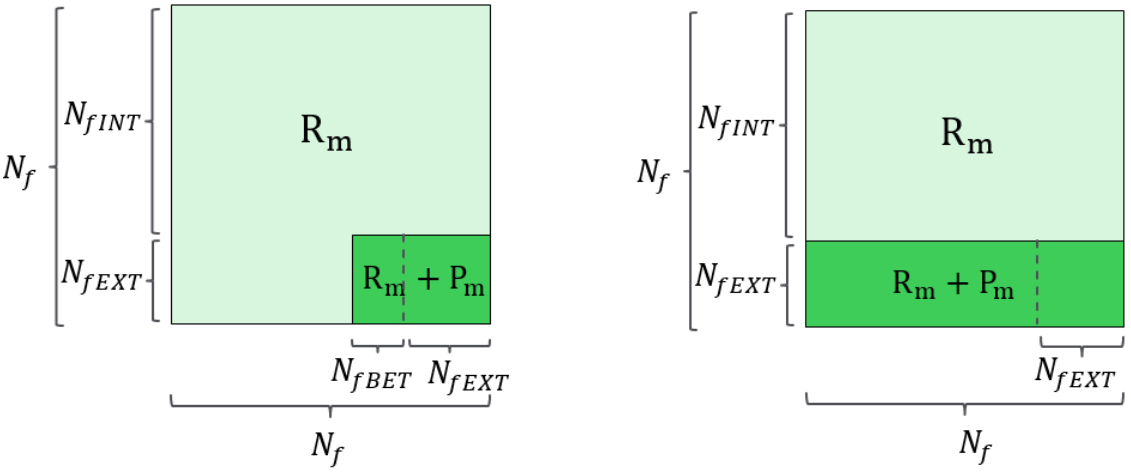

Figure III.10: Size of matrices $\mathbf{R_m}$ and $\mathbf{P_m}$ for linear (left) and nonlinear (right) problems.

System (III.40) provides the magnetic contribution for internal and external branches of the magnetic region, which is the first contribution of the field-circuit coupling. Let us

now explain the circuit contribution.

III.4.a-ii Electric circuit contribution

For the electric circuit contribution, a circuit relation for each coil k is needed, linking the voltage, the resistance, the current and the magnetic flux [64]:

$$\Delta \mathrm{V}_{\mathrm{c}_k} = \mathbf{R}_{\mathbf{c}_k} \mathbf{I}_{\mathbf{c}_k} + \frac{\mathrm{d}\Phi_{\mathrm{c}_k}}{\mathrm{d}t} \tag{III.43}$$

where $\Delta \mathrm{V}_{\mathrm{c}_k}$ is the voltage of coil k, $\mathbf{R}_{\mathbf{c}_k}$ is the resistance of coil k and Φ_{c_k} is the flux through coil k. The latter flux can be computed by

$$\Phi_{\mathrm{c}_k} = \int_{\Omega_{\mathrm{c}_k}} \mathbf{j}_{\mathbf{c}_k} \cdot \mathbf{A} \mathrm{d}\Omega_{\mathrm{c}_k} \tag{III.44}$$

where $\mathbf{j}_{\mathbf{c}_k}$ is the current density imposed on coil k and $\mathbf{A}$ is the magnetic vector potential, defined by $\mathbf{B} = \nabla \times \mathbf{A}$. The magnetic vector potential $\mathbf{A}$ can be split in two terms, the contribution of the coils in vacuum $\mathbf{A_0}$ and the contribution of the magnetic regions $\mathbf{A_m}$, with $\mathbf{A} = \mathbf{A_0} + \mathbf{A_m}$, then $\Phi_{\mathrm{c}_k} = \Phi_{0_k} + \Phi_{\mathrm{m}_k}$ where

$$\Phi_{0_k} = \int_{\Omega_{\mathrm{c}_k}} \mathbf{j}_{\mathbf{c}_k} \cdot \mathbf{A_0} \mathrm{d}\Omega_{\mathrm{c}_k} \quad \text{and} \quad \Phi_{\mathrm{m}_k} = \int_{\Omega_{\mathrm{c}_k}} \mathbf{j}_{\mathbf{c}_k} \cdot \mathbf{A_m} \mathrm{d}\Omega_{\mathrm{c}_k}. \tag{III.45}$$

$\mathbf{A_0}$ can be expressed as

$$\mathbf{A_0} = \frac{\mu_0}{4\pi} \sum_l \left(\int_{\Omega_{\mathrm{c}_l}} \frac{\mathbf{j}_{\mathbf{c}_l}}{r} \mathrm{d}\Omega_{\mathrm{c}_l} \right) \mathrm{I}_l \tag{III.46}$$

where I_l is the current of coil l and r is the distance between the integration point of the coils and the point where the vector potential is calculated. Then, the flux contribution coming from the coils in vacuum writes:

$$\Phi_{0_k} = \frac{\mu_0}{4\pi} \int_{\Omega_{\mathrm{c}_k}} \mathbf{j}_{\mathbf{c}_k} \cdot \left(\sum_l \mathrm{I}_l \int_{\Omega_{\mathrm{c}_l}} \frac{\mathbf{j}_{\mathbf{c}_l}}{r} \mathrm{d}\Omega_{\mathrm{c}_l} \right) \mathrm{d}\Omega_{\mathrm{c}_k}. \tag{III.47}$$

The inner integral can be computed with analytical expressions on the coil as explained in section II.2.f, whereas the external integral can be approximated with Gauss points. For the contribution of the magnetic region to the flux, following [42], the integration over the coil can be transformed in an integration over the magnetic region with:

$$\Phi_{\mathrm{m}_k} = \int_{\Omega_{\mathrm{c}_k}} \mathbf{j}_{\mathbf{c}_k} \cdot \mathbf{A_m} \mathrm{d}\Omega_{\mathrm{c}_k} = \mu_0 \int_{\Omega_{\mathrm{m}}} \mathbf{h}_{\mathbf{c}_k} \cdot \mathbf{M} \mathrm{d}\Omega_{\mathrm{m}} \tag{III.48}$$

where $\mathbf{h}_{\mathbf{c}_k}$ is the magnetic field generated by coil k with 1 A. Then, considering $\mathbf{M} = (\nu_0 - \nu(\mathbf{B}))\mathbf{B} + \mathbf{H_c}$ and the discretization of $\mathbf{B}$, the contribution to the flux of the magnetic regions can be written as:

$$\begin{gathered} \Phi_{\mathrm{m}_k} = \mu_0 \int_{\Omega_{\mathrm{m}}} \mathbf{h}_{\mathbf{c}_k} \cdot \left[(\nu_0 - \nu(\mathbf{B}))\mathbf{B} + \mathbf{H_c} \right] \mathrm{d}\Omega_{\mathrm{m}} = \\ \int_{\Omega_{\mathrm{m}}} \mathbf{h}_{\mathbf{c}_\mathrm{k}} \cdot (\nu_0 - \nu(\mathbf{B})) \mathbf{w}_j \mathrm{d}\Omega_{\mathrm{m}} \Phi_j + \int_{\Omega_{\mathrm{m}}} \mathbf{h}_{\mathbf{c}_\mathrm{k}} \cdot \mathbf{H_c} \mathrm{d}\Omega_{\mathrm{m}}. \end{gathered} \tag{III.49}$$

Coming back to equation (III.43), when applying the derivative with respect to time of Φ_{m_k}, the second term, which depends on the coercive field will vanish, being the first time the only one remaining. Then, equation (III.43) for a coil k can be written as:

$$\begin{aligned}\Delta \mathrm{V}_{\mathrm{c}_k} = \mathbf{R}_{\mathbf{c}_k}\mathbf{I}_{\mathbf{c}_k} + \frac{\mathrm{d}}{\mathrm{d}t}\left[\frac{\mu_0}{4\pi}\int_{\Omega_{\mathrm{c}_k}} \mathbf{j}_{\mathbf{c}_k}\cdot\left(\sum_l \mathrm{I}_l \int_{\Omega_{\mathrm{c}_l}} \frac{\mathbf{j}_{\mathbf{c}_l}}{r}\mathrm{d}\Omega_{\mathrm{c}_l}\right)\mathrm{d}\Omega_{\mathrm{c}_k}\right] + \\ \frac{\mathrm{d}}{\mathrm{d}t}\left[\int_{\Omega_{\mathrm{m}}} \mathbf{h}_{\mathbf{c}_{\mathrm{k}}}\cdot(\nu_0-\nu(\mathbf{B}))\mathbf{w}_j \mathrm{d}\Omega_{\mathrm{m}}\Phi_j\right].\end{aligned} \tag{III.50}$$

This equation can be extended to a matrix system that considers all the circuit coils with the following expression:

$$\boxed{\frac{\mathrm{d}}{\mathrm{d}t}(\mathbf{L_{cm}}\Phi) + \mathbf{R_c}\mathbf{I_c} + \frac{\mathrm{d}}{\mathrm{d}t}(\mathbf{L_c}\mathbf{I_c}) = \Delta \mathrm{V_c}} \tag{III.51}$$

where $\mathbf{R_c}$ is a diagonal matrix that contains the resistance of the coils, $\mathbf{L_{cm}}$ is the contribution of the magnetic region to the flux of the coils, with

$$\mathrm{L}_{\mathrm{cm}_{kj}} = \int_{\Omega_{\mathrm{m}}} \mathbf{h}_{\mathbf{c}_k}\cdot(\nu_0-\nu(\mathbf{B}))\mathbf{w}_j \mathrm{d}\Omega_{\mathrm{m}} \tag{III.52}$$

and $\mathbf{L_c}$ is the self and mutual inductance of the coils

$$\mathrm{L}_{\mathrm{c}_{kl}} = \frac{\mu_0}{4\pi}\int_{\Omega_{\mathrm{c}_k}} \mathbf{j}_{\mathbf{c}_k}\left(\int_{\Omega_{\mathrm{c}_l}} \frac{\mathbf{j}_{\mathbf{c}_l}}{r}\mathrm{d}\Omega_{\mathrm{c}_l}\right)\mathrm{d}\Omega_{\mathrm{c}_k} \tag{III.53}$$

which is computed between coils k and l.

System III.51 provides the electric circuit coils equations for the field-circuit coupling formulation. Let us gather it with the magnetic field contribution to obtain the general system.

III.4.a-iii Assembly of the magnetic field and circuit contributions

Finally, assembling the magnetic field and the circuit coils, therefore systems (III.40) and (III.51), the coupling system of the magnetic field and the electric circuit contributions with the volume integral formulation reads:

$$\boxed{\begin{cases}\mathbf{R_m}\Phi + \mathbf{P_m}\Phi + \mathbf{L_{mc}}\mathbf{I_c} = \Delta\overline{\varphi}_{\mathrm{r}} + \mathbf{U_m} \\ \frac{\mathrm{d}}{\mathrm{d}t}(\mathbf{L_{cm}}\Phi) + \mathbf{R_c}\mathbf{I_c} + \frac{\mathrm{d}}{\mathrm{d}t}(\mathbf{L_c}\mathbf{I_c}) = \Delta \mathrm{V_c}\end{cases}} \tag{III.54}$$

We will approach this system with a circuit form in order to solve it with a circuit solver.

III.4.b Circuit formulation

We aim at obtaining an expression of the time stepping formulation in a generic circuit form that looks like the following equation:

$$\mathbf{S}(\mathbf{X})\mathbf{X} + \frac{\mathrm{d}}{\mathrm{d}t}(\mathbf{T}(\mathbf{X})\mathbf{X}) = \mathbf{Q}(\mathbf{X}) \tag{III.55}$$

In our situation, this generic form is constituted of a primal mesh of the ferromagnetic region with nodes and branches (Figure III.8) and a dual mesh, which allows to link the quantities of type flux associated to potential differences. The generic circuit structure adapted to our case reads:

$$\mathbf{R}(\mathrm{I})\mathrm{I} + \frac{\mathrm{d}}{\mathrm{d}t}(\mathbf{L}(\mathrm{I})\mathrm{I}) = \Delta\mathrm{V} + \mathbf{U}_{\mathrm{sc}} \tag{III.56}$$

where

- I is composed of two parts: the electric currents, which are given in the coils and external circuit sources, and the magnetic flux of an equivalent circuit given a discretization of the magnetic regions. In practice, the latter flux is the one flowing through each branch of the dual mesh as explained in the magnetostatic case.
- ΔV is the electric or magnetic potential difference between the branches of the electric and magnetic circuit respectively.
- **R** and **L** matrices come from the magnetic circuit and they are obtained integrating on the primal mesh. These two matrices also contain the information of the coils resistance, the coupling terms between magnetic regions and coils and the external circuit components.
- Finally, $\mathbf{U}_{sc}$ is a term coming from the sources, such as the coils with current imposed.

The formulation system III.54 can be written in the circuit form (III.56) with

$$\begin{gathered}\mathbf{R} = \begin{bmatrix} \mathbf{R_m} + \mathbf{P_m} & \mathbf{L_{mc}} & \mathbf{0} \\ \mathbf{0} & \mathbf{R_c} & \mathbf{0} \\ \mathbf{0} & \mathbf{0} & \mathbf{R_{ex}} \end{bmatrix}, \quad \mathbf{L} = \begin{bmatrix} \mathbf{0} & \mathbf{0} & \mathbf{0} \\ \mathbf{L_{cm}} & \mathbf{L_c} & \mathbf{0} \\ \mathbf{0} & \mathbf{0} & \mathbf{L_{ex}} \end{bmatrix}, \quad \mathbf{I} = \begin{Bmatrix} \Phi \\ \mathbf{I_c} \\ \mathbf{I_{ex}} \end{Bmatrix}, \\ \mathbf{\Delta V} = \begin{Bmatrix} \Delta\overline{\boldsymbol{\varphi}}_{\mathrm{r}} \\ \Delta\mathrm{V_c} \\ \Delta\mathrm{V_{ex}} \end{Bmatrix} \text{ and } \mathbf{U_{sc}} = \begin{Bmatrix} \mathbf{U_m} \\ \mathbf{0} \\ \mathbf{0} \end{Bmatrix}.\end{gathered} \tag{III.57}$$

where subscript ex refers to the external circuit, being $\mathbf{R_{ex}}$ and $\mathbf{L_{ex}}$ the resistance and inductance components of the external circuit, $\mathbf{I_{ex}}$ the current of the external circuit and $\Delta\mathrm{V_{ex}}$ the potential difference of the external circuit. The remaining matrices come from system III.54.

Given that the circuit representation takes into account the physical regions, the coils and the external circuits, the couplings between these elements is made with a topological description of the circuits, where the eventual connections between them are executed with common electric nodes. We distinguish two types of components regarding the implementation convenience:

1. Ferromagnetic regions, coils, resistance and inductance components, which are treated directly as shown in (III.57).
2. Current sources, voltage sources and capacitors of external circuits whose contributions will be explained one by one in the next section III.4.b-i.

III.4.b-i Circuit solver

The circuit form in which system (III.54) is written allows to solve it with a circuit solver using either Kirchhoff's voltage law or Kirchhoff's current rule, which automatically ensures the free divergence of $\mathbf{B}$ (Maxwell's equation III.3).
For instance, Kirchhoff's voltage law can be defined with an incidence matrix of independent loops $\mathbf{M_I}$ such that $\mathbf{M_I}\Delta \mathrm{V} = 0$. An example of independent loops of the mesh was shown in the magnetosatic case in Figure II.9. When the incidence matrix is applied to the circuit formulation, the system to solve reads:

$$\mathbf{M_I R(I) M_I}^{\mathrm{T}}\mathbf{I_M} + \frac{\mathrm{d}}{\mathrm{d}t}\left(\mathbf{M_I L(I) M_I}^{\mathrm{T}}\mathbf{I_M}\right) = \mathbf{M_I U}_{\mathrm{sc}} \tag{III.58}$$

where $\mathbf{I_M}$ represents the flux on the independent loops, with $\mathbf{M_I^T I_M} = \mathbf{I}$.

Let us explain how to include the current sources, voltage sources and capacitors of external circuits at this stage of the solving process.

Voltage sources
The electric branches in which the voltage is imposed are placed on the right-hand side of the system (where the sources are located). We then consider the following partition of the incidence matrix:

$$\mathbf{M_I} = [\mathbf{M_{RL}}\ \ \mathbf{M_{US}}] \tag{III.59}$$

where $\mathbf{M_{RL}}$ is the partial incidence matrix corresponding to the branches coming from ferromagnetic regions, coils and external circuit components and $\mathbf{M_{US}}$ are the branches of the external circuits where the voltage is imposed. We can then write:

$$\mathbf{M_I}\Delta \mathrm{V} = \mathbf{M_{RL}U_{sc}} + \mathbf{M_{US}U_s} \tag{III.60}$$

Then, system (III.58) can be written taking into account the voltage sources as:

$$\mathbf{M_{RL}R(I)M_{RL}^T I_M} + \frac{\mathrm{d}}{\mathrm{d}t}\left(\mathbf{M_{RL}L(I)M_{RL}^T I_M}\right) = \mathbf{M_{RL}U_{sc}} + \mathbf{M_{US}U_s} \tag{III.61}$$

where $\mathbf{U_s}$ is the potential difference of the branches with voltage imposed.

Current sources
For current sources the incidence matrix is split in three blocks, detaching the circuit branches of the current sources $\mathbf{M_{IS}}$, such that:

$$\mathbf{M_I} = [\mathbf{M_{RL}}\ \ \mathbf{M_{IS}}\ \ \mathbf{M_{US}}]. \tag{III.62}$$

Then, the unknowns of the system remain the voltage difference on the current source branches and the currents of the mesh loops. Let us remark that

$$\mathbf{M_{IS}^T} \cdot \mathbf{I_M} = \mathbf{I_{IS}} \tag{III.63}$$

where $\mathrm{I_{IS}}$ are the currents on the branches of the current source. Then, system of equations (III.58) including the voltage and current sources writes:

$$\begin{cases} \mathbf{M_{RL}R(I)M_{RL}^T I_M} + \frac{\mathrm{d}}{\mathrm{d}t}\left(\mathbf{M_{RL}L(I)M_{RL}^T I_M}\right) + \mathbf{M_{IS}}\Delta \mathrm{V_{IS}} = \mathbf{M_{RL}U_{sc}} + \mathbf{M_{US}U_s} \\ \mathbf{M_{IS}^T I_M} = \mathbf{I_{IS}} \end{cases} \tag{III.64}$$

Capacitors of external circuits

For an external circuit, a capacitance branch verifies the following equation:

$$\mathbf{C_{ex}}\frac{\mathrm{d}}{\mathrm{d}t}\Delta \mathrm{V_c} = \mathbf{I_c} \tag{III.65}$$

where $\mathbf{C_{ex}}$ is the capacitance of the external circuit, $\mathrm{I_c}$ is the current of the capacitance branch and $\Delta \mathrm{V_c}$ are the voltage difference on the capacitance branches. This equation cannot be included in the system with the mesh currents, therefore $\Delta \mathrm{V_c}$ are included as additional unknowns.

A new partition of the incidence matrix is introduced:

$$\mathbf{M_I} = [\mathbf{M_{RL}}\ \ \mathbf{M_{IC}}\ \ \mathbf{M_{IS}}\ \ \mathbf{M_{US}}] \tag{III.66}$$

where $\mathbf{M_{IC}}$ refers to the capacitance branches of the circuit.

Let us remark that $\mathbf{M_{IC}^T} \cdot \mathbf{I_M} = \mathbf{I_c}$. Then, system of equations (III.58) including the voltage sources, current sources and capacitors of external circuits writes:

$$\begin{cases} \mathbf{M_{RL}R(I)M_{RL}^T I_M} + \frac{\mathrm{d}}{\mathrm{d}t}(\mathbf{M_{RL}L(I)M_{RL}^T I_M}) + \mathbf{M_{IC}}\Delta \mathrm{V_c} + \mathbf{M_{IS}}\Delta \mathrm{V_{IS}} = \mathbf{M_{RL}U_{sc}} + \mathbf{M_{US}U_s} \\ \mathbf{M_{IC}^T I_M} - \mathbf{C_{ex}}\frac{\mathrm{d}}{\mathrm{d}t}\Delta \mathrm{V_c} = 0 \\ \mathbf{M_{IS}^T I_M} = \mathbf{I_{IS}} \end{cases} \tag{III.67}$$

This system can be written in the circuit explained before:

$$\mathbf{S(X)X} + \frac{\mathrm{d}}{\mathrm{d}t}(\mathbf{T(X)X}) = \mathbf{Q(X)}$$

where

$$\begin{gathered} \mathbf{S} = \begin{bmatrix} \mathbf{M_{RL}RM_{RL}^T} & \mathbf{M_{IC}} & \mathbf{M_{IS}} \\ \mathbf{M_{IC}} & \mathbf{0} & \mathbf{0} \\ \mathbf{M_{IS}^T} & \mathbf{0} & \mathbf{0} \end{bmatrix}, \quad \mathbf{X} = \begin{Bmatrix} \mathbf{I_M} \\ \Delta \mathrm{V_c} \\ \Delta \mathrm{V_{IS}} \end{Bmatrix}, \\ \mathbf{T} = \begin{bmatrix} \mathbf{M_{RL}LM_{RL}^T} & \mathbf{0} & \mathbf{0} \\ \mathbf{0} & -\mathbf{C_{ex}} & \mathbf{0} \\ \mathbf{0} & \mathbf{0} & \mathbf{0} \end{bmatrix}, \quad \mathbf{Q} = \begin{Bmatrix} \mathbf{M_{RL}U_{sc}} + \mathbf{M_{US}U_s} \\ \mathbf{0} \\ \mathbf{I_{IS}} \end{Bmatrix}. \end{gathered} \tag{III.68}$$

This is the final system describing the field-circuit coupling formulation written in circuit form with its incidence matrix and that includes all the possible elements of the external circuit: current sources, voltage sources and capacitors.

Once this system has been defined, its resolution is carried out with a θ scheme time stepping method with a nested Newton-Raphson (NR) loop to solve the nonlinear term, which uses the jacobian matrices that have been explained previously in section III.4.b-ii. Let us explain the nonlinear resolution and the time scheme more in detail.

III.4.b-ii Nonlinear resolution

In order to deal with nonlinear materials, we will use the Newton-Raphson method to solve the obtained system, which defines a residual Res of the problem and then computes:

$$\frac{\partial \mathrm{Res}(\mathrm{I_n})}{\partial \mathrm{I}}(\mathrm{I_{n+1}} - \mathrm{I_n}) = -\mathrm{Res}(\mathrm{I_n}) \tag{III.69}$$

Then, derivative of the residual Res with respect to the unknowns is needed, and more precisely, the one of matrices $\mathbf{R_m\Phi}, \mathbf{P_m\Phi}$, and $\mathbf{L_{cm}\Phi}$ given that the other matrices of system (III.54) don't depend on the unknown I. As explained in the magnetostatic case, for the contribution of matrix $\mathbf{R_m}$ to the jacobian matrix, the reluctivity is changed by the differential reluctivity tensor $\left[\frac{\partial \mathbf{H}}{\partial \mathbf{B}}\right]$:

$$J(\mathrm{R_{m_{i,j}}}) = \int_{\Omega_\mathrm{m}} \mathbf{w}_i \cdot \left[\frac{\partial \mathbf{H}}{\partial \mathbf{B}}\right] \cdot \mathbf{w}_j \mathrm{d}\Omega_\mathrm{m}, \tag{III.70}$$

where J is the contribution to the jacobian matrix. For the contribution to the jacobian of $\mathbf{P_m}$ and $\mathbf{L_{mb}}$ matrices, in order to speed up the computations, and knowing that for both matrices the reluctivity ν has significant less weight than ν_0 in its expression (III.79) then $(\nu_0 - \nu)$ is approximated by ν_0, which is constant at each NR iterations, therefore we approximate their influence to the jacobian matrices by themselves, without deriving the reluctivity tensor:

$$J(\mathbf{P_m}) \approx \mathbf{P_m} \quad \text{and} \quad J(\mathbf{L_{mb}}) \approx \mathbf{L_{mb}}. \tag{III.71}$$

Let us remark that these approximations don't deteriorate the accuracy of the solution because the equation of Newton-Raphson method is defined by a residual. Nevertheless, they can affect to the convergence speed of the resolution.

We then have all the elements to carry out the nonlinear resolution. Let us explain the theta time stepping method used to obtain a solution in time of system (III.54).

III.4.b-iii Theta scheme time stepping method

We have considered a theta scheme time stepping method to solve system (III.58). However, many others time schemes could have been selected to achieve the time stepping resolution such as Runge-Kutta family of methods or predictor-corrector strategies. There exist examples of other methods applied to FEM formulations, such as the Newmark-beta time stepping strategy [60] or a predictor-corrector method that divides over two the time step if the difference between the predictor and the corrector is higher than a certain error [59]. As a first choice, we have decided to implement the theta scheme given that it is the most well-known temporal discretization method, whose convergence is proven [50] and because of its simplicity.

We then start with the time dependent circuit form that has been already described:

$$\mathbf{S}(\mathbf{X}, t)\mathbf{X} + \frac{\mathrm{d}}{\mathrm{d}t}(\mathbf{T}(\mathbf{X}, t)\mathbf{X}) = \mathbf{Q}(\mathbf{X}, t) \tag{III.72}$$

where t is the time variable and $t \in [0, T]$. Sorting the terms, it can also be written as:

$$\frac{\mathrm{d}}{\mathrm{d}t}(\mathbf{T}(\mathbf{X}, t)\mathbf{X}) = -\mathbf{S}(\mathbf{X}, t)\mathbf{X} + \mathbf{Q}(\mathbf{X}, t) \tag{III.73}$$

Let us group the terms on the right hand side with $\mathbf{F}(\mathbf{X}, t) = -\mathbf{S}(\mathbf{X}, t)\mathbf{X} + \mathrm{Q}(\mathbf{X}, t)$, then:

$$\frac{\mathrm{d}}{\mathrm{d}t}(\mathbf{T}(\mathbf{X}, t)\mathbf{X}) = \mathbf{F}(\mathbf{X}, t). \tag{III.74}$$

We discretize the time t with a fixed time step Δt such that $t = [0, \Delta t, 2\Delta t, ..., N\Delta t] = [t_0, t_1, ..., t_N]$. We approximate the derivative of $\mathbf{T}(\mathbf{X}, t)\mathbf{X}$ with respect to time as:

$$\frac{\mathrm{d}}{\mathrm{d}t}(\mathbf{T}(\mathbf{X}, t)\mathbf{X}) \approx \frac{\mathbf{T}(\mathbf{X}_{n+1}, t_{n+1})\mathbf{X}_{n+1} - \mathbf{T}(\mathbf{X}_n, t_n)\mathbf{X}_n}{\Delta t} \tag{III.75}$$

where $\mathbf{X}_n$ refers to the value of $\mathbf{X}$ at time t_n, that is to say, $\mathbf{X}(t_n)$ and $t_{n+1} = t_n + \Delta t$. The theta schema for equation (III.74) using (III.75) writes:

$$\frac{\mathbf{T}(\mathbf{X}_{n+1}, t_{n+1})\mathbf{X}_{n+1} - \mathbf{T}(\mathbf{X}_n, t_n)\mathbf{X}_n}{\Delta t} = \theta\mathbf{F}(\mathbf{X}_{n+1}, t_{n+1}) + (1-\theta)\mathbf{F}(\mathbf{X}_n, t_n) \tag{III.76}$$

which can be developed using the definition of $\mathrm{F}(\mathbf{X}, t)$:

$$\begin{gathered}\left[\frac{\mathbf{T}(\mathbf{X}_{n+1}, t_{n+1})}{\Delta t} + \theta\mathbf{S}(\mathbf{X}_{n+1}, t_{n+1})\right]\mathbf{X}_{n+1} = \\ \frac{\mathbf{T}(\mathbf{X}_n, t_n)\mathbf{X}_n}{\Delta t} + \theta\mathbf{Q}_{n+1} + (1-\theta)\left[-\mathbf{S}(\mathbf{X}_n, t_n)\mathbf{X}_n + \mathbf{Q}_n\right]\end{gathered} \tag{III.77}$$

We notice that $\mathbf{Q}_{n+1}$ is written on the right hand side of the equation because it is known at every time step.

θ is a fixed parameter $\theta \in [0, 1]$ that is chosen depending on the nature of the equation, the most common choices are:

- $\theta = 0$, then the only explicit scheme is found, known by the name Euler explicit or forward method.
- $\theta = 1$ holds the Euler implicit or backward scheme, which is very stable for stiff problems.
- $\theta = \frac{1}{2}$ obtaining the Crank-Nicolson method [49], which is the only θ scheme of accuracy order 2, contrary to Euler explicit or Euler implicit that have accuracy order 1. Therefore, it is interesting to use it in terms of precision of the solution.

Let us note that any value of θ belonging to the internal $[0, 1]$ can be considered.

We now have all the elements needed to solve the field-circuit coupling formulation. The next section provides several strategies to improve the computation time.

III.4.c Considerations on the resolution strategy

To summarize, given a generic problem of the form that Figure III.2 shows, we have obtained the system that assembles the magnetic field and the circuit contribution in a circuit form. We applied either Kirchhoff's voltage law or Kirchhoff's current law, which automatically ensures the free divergence of $\mathbf{B}$ and that makes use of an incidende matrix to obtain system (III.58), in this case with Kirchhoff's voltage rule. We then took into

account separately some circuit elements: current sources, voltage sources and capacitors explaining the obtained matrices. We have also explained how the resolution is performed, using a time stepping θ-method with a nested Newton-Raphson loop to solve nonlinear problems for which we have obtained the jacobian matrices.

Let us finish with some additional considerations in the resolution stage to improve the computation time:

1. For the computation of $\mathbf{P_m}$ matrix, that we remind:

$$\mathrm{P_m}_{ij} = \frac{1}{4\pi} \int_{\Gamma_{ext_i}} \frac{1}{S_i} \left(\int_{\Gamma_j} \frac{1}{S_j} \frac{\delta\nu_j}{r} \mathrm{d}\Gamma_j \right) \mathrm{d}\Gamma_i, \tag{III.78}$$

   we consider a decomposition in two factors such that:

$$\mathrm{P_m}_{i,j} = \delta\nu_j \mathrm{Q}_{ij}, \quad \text{where} \quad \mathrm{Q}_{ij} = \frac{1}{4\pi} \frac{1}{S_i} \frac{1}{S_j} \int_{\Gamma_{ext_i}} \left(\int_{\Gamma_j} \frac{1}{r} \mathrm{d}\Gamma_j \right) \mathrm{d}\Gamma_i \tag{III.79}$$

   being $\mathbf{Q}$ a matrix that only depends on the geometry of the problem. Then, $\mathbf{Q}$ can be computed one time in the whole resolution time and be multiplied by $\delta\nu_j$ for each time step.

2. In order to speed the computations, a matrix compression technique can be used, such as fast multipole method on matrix $\mathbf{P_m}$. A GMRES iterative solver is then considered.

3. Another technique to accelerate the computations is to use a LU type preconditioner. This preconditioner can be applied to matrices $\mathbf{R}$ and $\mathbf{L}$ that are described in system (III.68). Then, these two matrices will be approximated by $\mathbf{R^*}$ and $\mathbf{L^*}$, and the definition of $\mathbf{S}$ and $\mathbf{T}$ matrices of the system written in the circuit form (III.68) will be:

$$\mathbf{S} = \begin{bmatrix} \mathbf{M_{RL}} \mathbf{R}^* \mathbf{M_{RL}^T} & \mathbf{M_{IC}} & \mathbf{M_{IS}} \\ \mathbf{M_{IC}} & \mathbf{0} & \mathbf{0} \\ \mathbf{M_{IS}^T} & \mathbf{0} & \mathbf{0} \end{bmatrix}, \quad \mathbf{T} = \begin{bmatrix} \mathbf{M_{RL}} \mathbf{L}^* \mathbf{M_{RL}^T} & \mathbf{0} & \mathbf{0} \\ \mathbf{0} & -\mathbf{C_{ex}} & \mathbf{0} \\ \mathbf{0} & \mathbf{0} & \mathbf{0} \end{bmatrix} \tag{III.80}$$

   where the preconditioned matrices $\mathbf{R^*}$ and $\mathbf{L^*}$ are defined by:

$$\mathbf{R^*} = \begin{bmatrix} \mathbf{R_m} & \mathbf{0} & \mathbf{0} \\ \mathbf{0} & \mathbf{R_c} & \mathbf{0} \\ \mathbf{0} & \mathbf{0} & \mathbf{R_{ex}} \end{bmatrix}, \quad \mathbf{L^*} = \begin{bmatrix} \mathbf{0} & \mathbf{0} & \mathbf{0} \\ \mathbf{0} & \mathrm{diag}(\mathbf{L_c}) & \mathbf{0} \\ \mathbf{0} & \mathbf{0} & \mathbf{L_{ex}} \end{bmatrix} \tag{III.81}$$

   where $\mathrm{diag}(\mathbf{L_c})$ is a matrix of the same size as $\mathbf{L_c}$ that only contains its diagonal terms.

4. The time stepping method has been explained for a fixed time step. However, we have also implemented an adaptive time step strategy using a predictor-corrector method with the aim or reducing the computation time. This scheme works well but needs two resolutions for each time step (Heun's method), which is why we could not reduce the computation time with this scheme. Nevertheless, another predictor-corrector method that only needs one resolution per time step could be implemented to reduce the computation time.

These are all the remarks regarding the time stepping nonlinear volume integral formulation based on facet elements for magnetic non conductive regions. It is worth mentioning that we have also extended the thin air gap model explained in chapter 2 for the magnetostatic case to work in the strong field-circuit coupling time stepping formulation.

Given that the formulation has been explained, let us now show an application of it with NSX sensor.

III.4.d Application to NSX sensor

The explained formulation is applied to NSX sensor that we have previously explained. We only consider the current transformer. The secondary coil is linked to a resistance of 63 Ω, forming an external circuit where the field-circuit coupling appears.

The results of the strong coupling developed with the VIM are compared to the ones obtained with the commercial software Flux3D of Altair, which is based on the FEM.

The characteristics of the model are the same than for the weak coupling, let us recapitulate them:

- The ferromagnetic region will consist of a linear material that follows an isotropic model of permeability μ_r =1000 for the linear case and an isotropic analytic saturation of arc tangent type with two coefficients: μ_r =1000 and saturation magnetization = 1.2 T for the nonlinear case.

- The primary conductor will impose a current of $\mathrm{I_p} = 300\sin(2\pi f t)$, where f is the frequency, which is set to 50 Hz, and t is the time. This conductor is again defined as a closed loop of dimension 1 meter times 1 meter, which is large compared to the sensor size, in order to avoid to perceive the return of the conductor.

- The secondary coil has 980 turns and no imposed current. It is linked to an external circuit that has a resistance of 63 Ω, Figure III.11.

- The output is the current through the secondary coil.

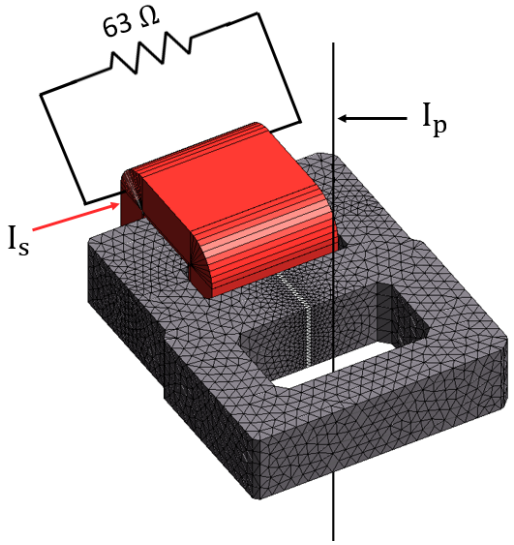

Figure III.11: Field-circuit coupling model for NSX, mesh of 46 000 elements.

For this implementation, a thinner mesh could be chosen given the computation time. We then consider the mesh of 46000 elements in the current transformer that was used in the magnetostatic case to obtain the mesh convergence (Figure II.13). Then, for the VIM method 46 000 is the total number of mesh elements whereas for the FEM there are 46 000 elements modeling the current transformer of second order and 308 000 modeling the air around it.

For the linear case, the results obtained for strong VIM field-circuit coupling (VIM str, green line) and the FEM (Ref, black line) are shown in Figure III.12 on the left y-axis. In blue the relative difference point by point over the maximum value of the reference is displayed on the right y-axis.

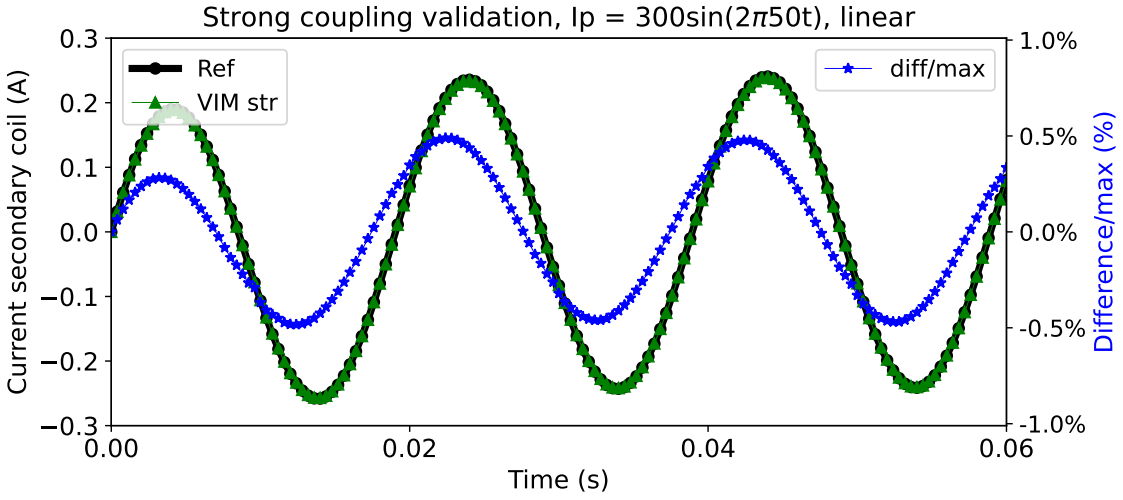

Figure III.12: Strong Field-circuit coupling model validation for NSX, linear case.

Let us notice that both methods, Ref and VIM str, have a similar initialization, since

the first period shows lower values that stabilise on the third period. The difference over the maximum of the reference is inferior to 0.5 %, which validates the strong VIM field-circuit coupling implementation for linear materials.
Regarding the computation time, the reference took 2 hours and 10 minutes whereas our VIM implementation took 1 hour and 18 minutes, being VIM faster.

For the nonlinear case, for which the only change is the material of the ferromagnetic region, the results are shown in Figure III.13. The difference over the maximum of the reference is always inferior to 0.6 %, which validates the strong field-circuit coupling implementation for nonlinear materials. Again, the computation time of the reference is improved with our method, taking 45 hours for the reference (Ref) and 26 hours for our VIM implemented method. This is mainly due to slow convergence using FEM, which does not occur with VIM.

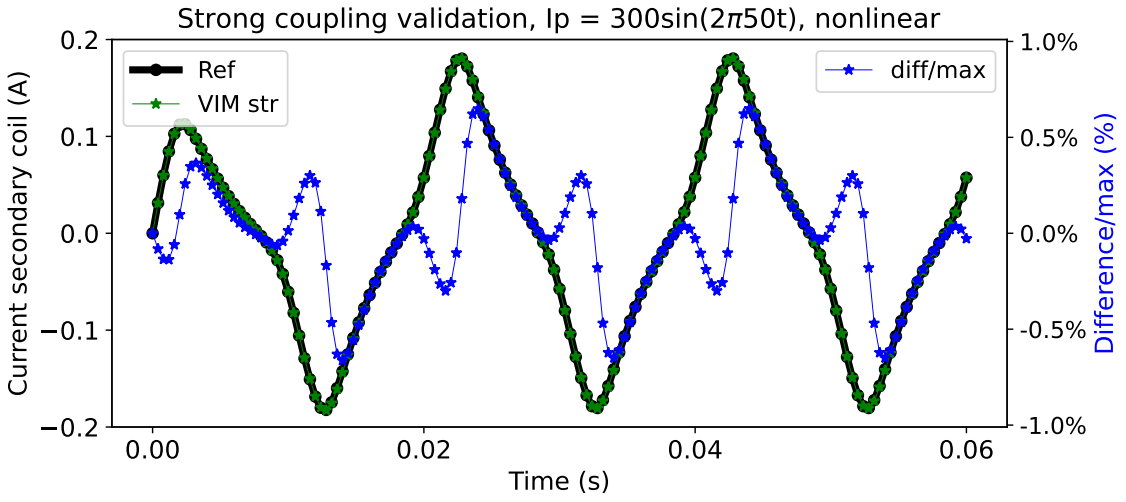

Figure III.13: Strong Field-circuit coupling model validation for NSX, nonlinear case.

III.5 Conclusion

An extension of the volume integral magnetostatic formulation of chapter 2 to a time stepping one has been developed. This advanced formulation takes into account the field-circuit coupling. The domain considered is composed of nonlinear non conductive magnetic regions and coils that are linked to external circuits. Two approaches were considered:

1. A first weak method which is restricted to current transformers with a simple circuit composed of a resistance on the secondary coil.

2. A strong formulation that is more general, it is not restricted to current transformers and it includes more elements on the external circuits linked to the coils, such as voltage sources or capacitors.

The weak method presents two algorithms, one for linear materials, which is very efficient in time, and another for nonlinear materials, which uses Newton-Raphson method and happens to be more time consuming than the reference taken. Both algorithms have

been validated with the current transformer of NSX sensor, showing very little difference in accuracy with the reference.

The strong coupling method is expressed in circuit form, and it is carefully developed to assemble the magnetic field equations with the external circuit equations in a final matrix system that can take into account external circuit elements such as voltage sources, current sources or capacitors. For the time discretization, it uses a θ scheme and for the non linearity of the materials, the Newton-Raphson method is considered. It is validated with the current transformer of NSX sensor comparing it with a reference resolution for a linear and a nonlinear material. For both materials, our implementation shows faster results than the reference.

The validation case of NSX has shown that these time stepping field-circuit coupling formulations based on the volume integral method allow to obtain accurate simulations of the sensors of interest, taking into account phenomena such as: nonlinear materials, field-circuit coupling or thin air gaps.

Both methods, the weak and the strong coupling, are based on the same equations and they provide similar results. Nevertheless, the weak coupling has been less developed, being restricted to current transformers with a resistance linked to the secondary coil. Then, if the problem that we are treating has this structure and it is linear, we encourage to use the weak field-circuit coupling, given that it is accurate and fast. However, if the problem is nonlinear, we promote the strong field-circuit coupling method, due to the computation time.

Next chapter uses the strong field-circuit coupling for the application of MTZ sensor, given that it is nonlinear, for which we don't only consider the current transformer but we also take into account the Rogowski metering coil, obtaining accurate results that we couldn't obtain with the FEM.

Chapter IV

Application case: self-powered sensor of MTZ Masterpact circuit breaker

Summary

This chapter shows an application case of the formulations developed in chapter 2 and chapter 3 to prove that they can accurately model the current sensors of interest. The sensor considered is part of the MTZ Masterpact circuit breaker and it is composed of a current transformer and a classic Rogowski coil. First, a validation of the current transformer model is shown, comparing simulation data with experimental data. Then, the robustness of the Rogowski metering coil is tested with simulations linked to the off-centre and the crosstalk. Further understanding of the Rogowski metering coil is examined by finding the distribution of the flux along it. Finally, an idea to homogenize this flux distribution is proposed with the use of a shielding technique.

IV.1 Introduction

The purpose of this thesis is to develop a volume integral formulation that allows to model with accuracy self-powered current sensors composed of a current transformer (power supply) and a metering coil, which ensure the protection and the metering function. To that aim, chapter 2 shows a magnetostatic volume integral formulation for nonlinear materials with thin air gaps and chapter 3 extends this formulation to a time stepping one that takes into account the field-circuit coupling if coils are connected to external circuits. In this chapter, we present an industrial application of the formulations previously explained, obtaining results that allow to model accurately a sensor of Schneider Electric taking into account its environment. They also show the validity of the developed formulations to model current sensors.

The current sensor chosen for this application is the one embedded in Masterpact MTZ circuit breaker, which has been developed by Schneider Electric and it is commercially available since 2016 (Figure IV.1).

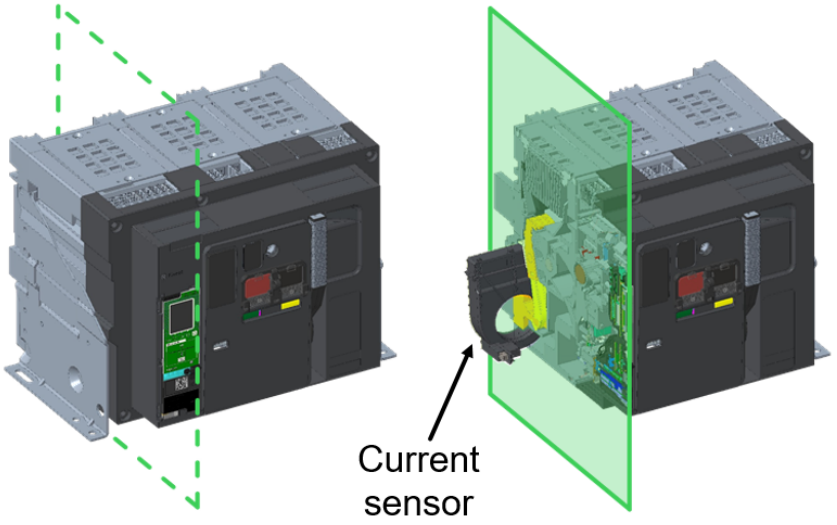

Figure IV.1: Masterpact MTZ circuit breaker.

This circuit breaker is known for its high accuracy in active power, reactive power, current and voltage. In general, a circuit breaker takes action in 3 steps:

1. Detection of a defect, that could be over currents or insulation defects. Over currents include overloads and short-circuits. This is perceived with a current sensor.

2. Opening the contacts to interrupt the circuit with an actuator. The contacts have to carry the load current without heating too much, moreover, they have to withstand the heat of the arc generated when opening the circuit.

3. Control the arc that has been produced. It has to be contained and cooled so that the contacts are closed again and the power is restored.

A self-powered current sensor is a crucial part of the circuit breaker, which has three functions: first, supply power to the electronic components to analyse the signal; second,

(a) Front view. (b) Profile view. (c) Lateral view.

Figure IV.2: Masterpact MTZ current sensor.

have a fast measuring of the instantaneous current; and third obtain an accurate value of the electric characteristic magnitudes. In Masterpact MTZ circuit breaker, the current sensor is composed of two parts that are assembled together: a current transformer and a Rogowski metering coil as Figure IV.2 shows. Let us explain each of the parts more in detail:

- The **Rogowski metering coil** is of classic type with circular shape and it has a plastic core that allows to wind the copper wire around it without interfering with the magnetic field. It is first winded in one direction and then a counter wound (as explained in section I.2.a-i) finishes the winding of 1600 turns, keeping a small space without any turns to connect the electronics to the Rogowski coil. To compensate this space that is not winded, compensation turns are added on the right and the left of this gap, as indicated in Figure IV.3, on the right image.

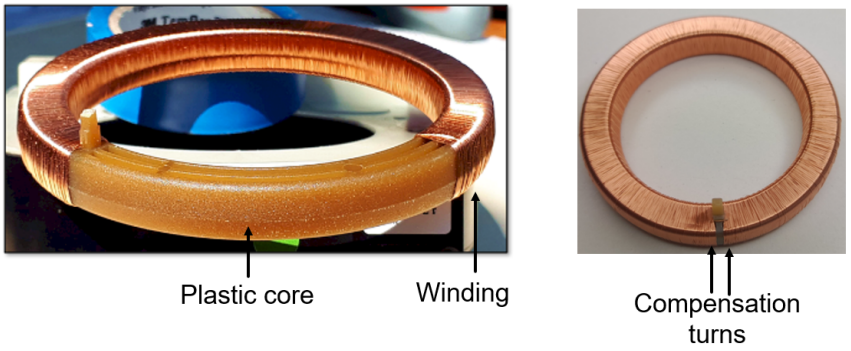

Figure IV.3: Rogowski metering coil of Masterpact MTZ current sensor.

- The **current transformer** is made out of sheets to avoid eddy currents. In this case, 23 sheets of 0.35 mm of thickness, which are made of is silicon steel. The secondary coil is winded along a straight segment with 2000 turns, as shown in Figure IV.4.

Figure IV.4: CT of Masterpact MTZ current sensor.

Inside Masterpact MTZ circuit breaker, each phase is measured using this current sensor, having three of them placed as in Figure IV.1 with a current phase shift of 120 degrees.

The aim of this chapter is to launch simulations with the previously developed formulations. The model will be useful to analyse certain characteristics of the sensor in order to increase its robustness. They will also be interesting to identify key design parameters that might arise in the development of future sensors.

There are indeed some aspects that are not easy to control in the manufacturing process. For instance, a uniform winding distribution of the Rogowski metering coil is not simple. This is partly due to the circular shape of the coil, for which the winding machine needs robotic arms to pass the wire through the center of the coil. Additionally, the inner and the outer radius are different and the tension of the wire has to be controlled at each moment, which is not easy. Moreover, some wire turns might slide on others, creating very small areas in which the density of turns is lower or higher than others. This might lead to a non uniform distribution of the turns along the coil. Finally, for the metering coil, the start and the end are placed at the same place due to the counter-wound and there is a small area next to it that is not winded. Then, compensation turns around the area that is not winded are considered to balance that portion where there are no turns, which creates a small region of the coil where the density of turns is higher.

Apart from manufacturing challenges, there are other design difficulties that have to be addressed, such as the fact that the current transformer and the Rogowski metering coil are next to each other, placed at a very low distance (0.4mm), which can perturb the metering function of the Rogowski coil. Indeed, the Rogowski metering coil is accurate when it is perfectly winded, nevertheless, if there is a small defect, the current transformer that is placed close to it will amplify the defects.

In this chapter we analyse three different aspects related to the robustness of Masterpact MTZ circuit breaker current sensor. Two of them are related to the effect of the

current transformer on the Rogowski metering coil, which is very important because current transformer is not perturbed by the Rogowski coil, but the Rogowski coil is indeed perturbed by the presence of the current transformer. We aim at modeling better this phenomenon and the possible manufacturing defects that might occur with the following inquiries:

1. The first one is a validation of the current transformer simulation model with experiments, which ensures that the simulation model is indeed realistic.

2. We then study the off-centre of the Rogowski coil, that is to say, what is the effect of having a small displacement on the Rogowski coil for the accuracy of the metering sensor. This is part of the requirements of a robust Rogowski sensor that is explained in section I.2.a-i.

3. Another requirement of a robust Rogowski sensor is having low crosstalk, we then study the crosstalk magnitude when there are three sensors placed next to each other that are out of phase. This is to make sure that the primary conductor of a sensor does not perturb the other two sensors.

Before getting into them, let us explain more details of the current sensor model.

IV.2 Further explanation of the current sensor model

There are some details of Masterpact MTZ current sensor that we haven't detailed before, more precisely:

- The current transformer has **two air gaps**, the first one is a thin one ($7 \cdot 10^{-6}$ m) at the bottom left of Figure IV.5 that arises when welding two magnetic parts in order to be able to introduce the secondary coil. The second air gap is thicker ($1.8 \cdot 10^{-3}$ m) and it is deliberately created by design for the right functioning of the sensor so that the secondary coil produces high voltage without getting burnt. Indeed, when a current flows through the primary conductor a magnetic field is created and it spreads along the magnetic core to produce a voltage in the secondary coil. If the thick air gap didn't exist, the magnetic flux would flow along loop B presented in Figure IV.5 and not much of it would reach the secondary coil. However, thanks to the thick air gap, the magnetic flux flows along the loop A of Figure IV.5, producing higher voltage in the secondary coil, which will power the electronic circuit connected to it. Moreover, when the material is saturated, the magnetic flux stops following along loop A (given the saturation) and flows along loop B, which is positive because the secondary coil will have enough voltage at that stage to power the electronic elements, and it avoids overpowering them, which could lead to burn the coil.

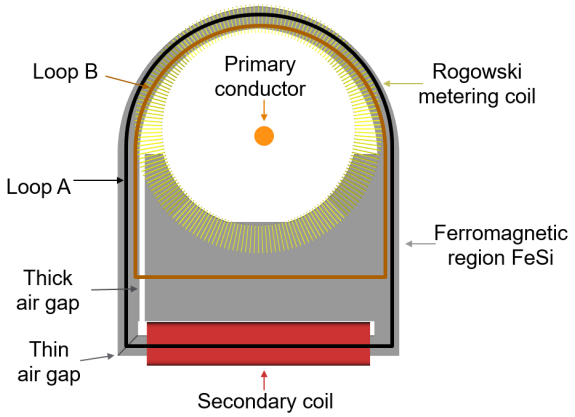

Figure IV.5: Geometry MTZ.

- The **primary conductor** of the current transformer is a straight bar, although in the simulations we will create a closed loop that is far enough to avoid that the return of the conductor affects to the measuring of the sensor, with a length of 1 meter as Figure IV.6a shows. The usual imposed currents on the primary conductor to test are $20\sqrt{2}$ A, $50\sqrt{2}$ A and $2000\sqrt{2}$ A. The general dimensions of the sensor are shown in Figure IV.6b.

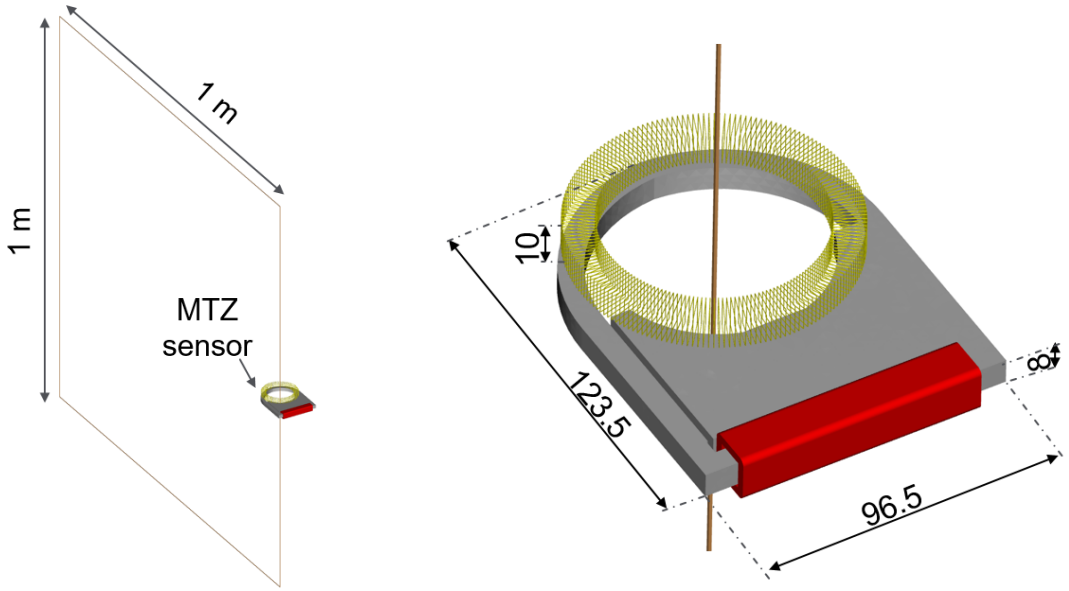

(a) Dimension of primary conductor.

(b) Dimension of MTZ, in millimeters.

Figure IV.6: Geometry of Masterpact MTZ sensor and dimension.

- The **magnetization curve** of the current transformer core made out of silicon steel (FeSi) will be simulated with the magnetization curve defined by splines that Figure IV.7 shows. This curve has been obtained with experimental measures on one of the material's sheet composing the magnetic core and they have been manually calibrated to make sure that the curve is monotonic and to have a slope similar to μ_0 for a very high value of H.

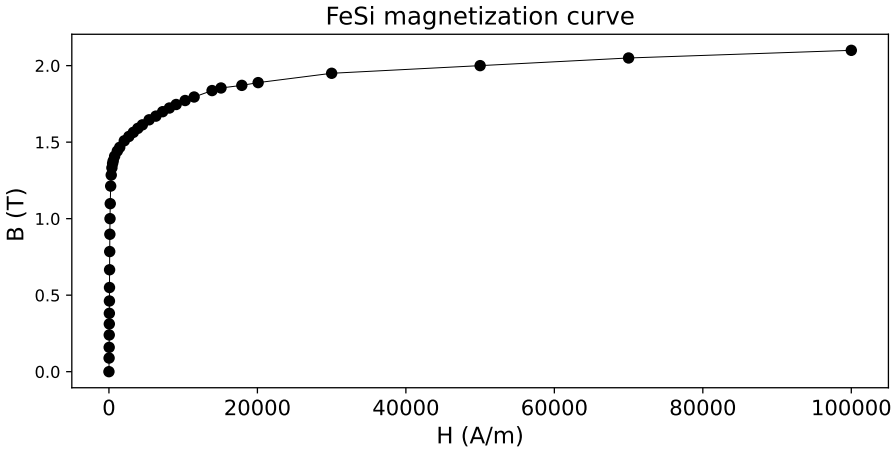

Figure IV.7: Magnetization curve of FeSi defined by splines.

- The Rogowski metering coil is placed 0.4 mm over the current transformer and it has 1600 turns. For the simulations, we will be interested in knowing the distribution of the flux along the coil. The way of simulating this distribution will be to create a coil with only one turn of rectangular shape every two degrees in order to be able to obtain the magnetic flux through each of these 180 small coils, then the flux through the Rogowski coil will be the flux sum of these coils. Figure IV.8 shows these 180 rectangular coils.

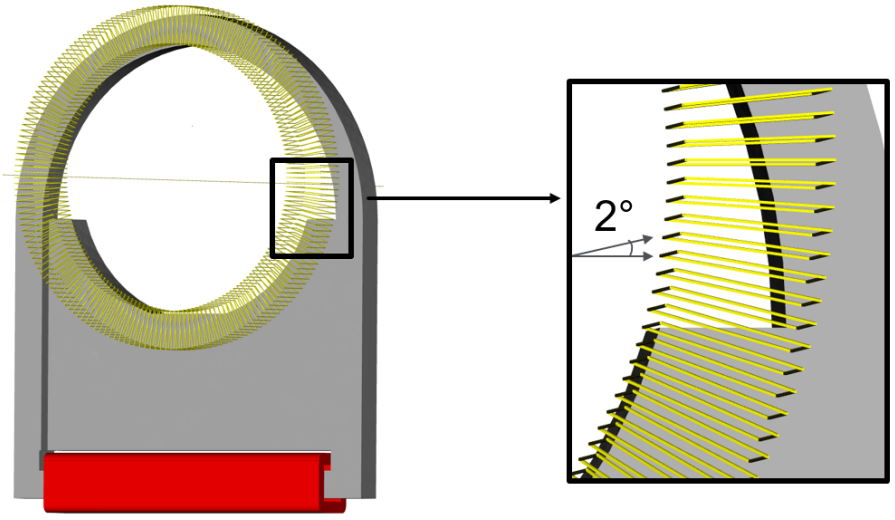

Figure IV.8: Rogowski metering coil modeling with 180 rectangular coils of 1 turn.

These are the main characteristics taken into account for the model of the current sensor. We can now start the simulations.

IV.3 Simulation model validation with experiments

The first simulation case takes into account the current transformer of the sensor. The aim is to run simulations and compare them with real data experiments to validate the

model, giving credibility to the remaining simulations of this chapter.

The simulations will use the strong coupling time stepping formulation of chapter 3 and the air gap model explained in chapter 2. The parameters considered are the following:

- There are three cases of current applied in the primary conductor: $A\sin(2\pi ft)$, for $A = 20\sqrt{2}$, $50\sqrt{2}$, $2000\sqrt{2}$ where t is the time and f is the frequency, chosen to be 55 Hz. The frequency is 55 Hz in this section instead of 50 Hz because the measuring devices provided more precision with 55 Hz than with 50 Hz in the experiments. The data will be obtained for 5 periods, therefore $t \in [0, 0.0909]$. For the simulation there will be 80 time steps per period.

- The secondary coil is linked to a resistance of 1 Ω where the field-circuit coupling will arise as shown in Figure IV.9.

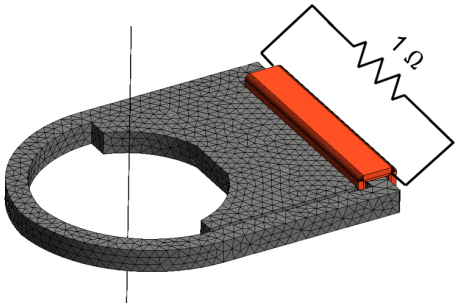

Figure IV.9: Masterpact MTZ sensor meshed with 9000 elements.

- The simulation model has a mesh of 9000 elements for the core of the current transformer, as shown in Figure IV.9. The geometry of the simulation model is simplified, skipping small details created for mechanical constraints, such as two holes created to keep the sensor in place. Simplified geometry elements are represented with blue circles in Figure IV.10.

Figure IV.10: Masterpact MTZ current transformer, geometry elements in blue that are simplified in the simulation model.

- Both air gaps are considered in the model. The thin air gap uses the model of chapter 2, meshing it as a surface element with a numerical treatment.

- The shape of the primary conductor is a straight bar for the experiments, as in Figure IV.11, and a thin conductor that forms a loop of 1 m for the simulations as shown before in Figure IV.6a, which ensures that the model doesn't perceive the return of the conductor because it is 1 meter far.

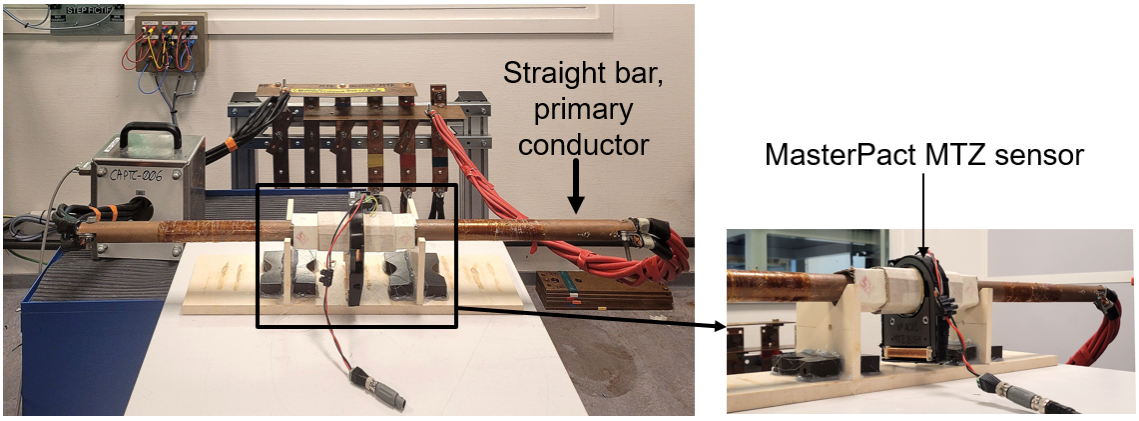

Figure IV.11: Experiments setting.

The results for an applied current in the primary conductor of $I_p = 20\sqrt{2}\sin(2\pi ft)$, $I_p = 50\sqrt{2}\sin(2\pi ft)$ and $I_p = 2000\sqrt{2}\sin(2\pi ft)$ are shown in Figures IV.15a, IV.15b and IV.14 respectively, where the black line refers to the experiments data and the green line to the simulation data.

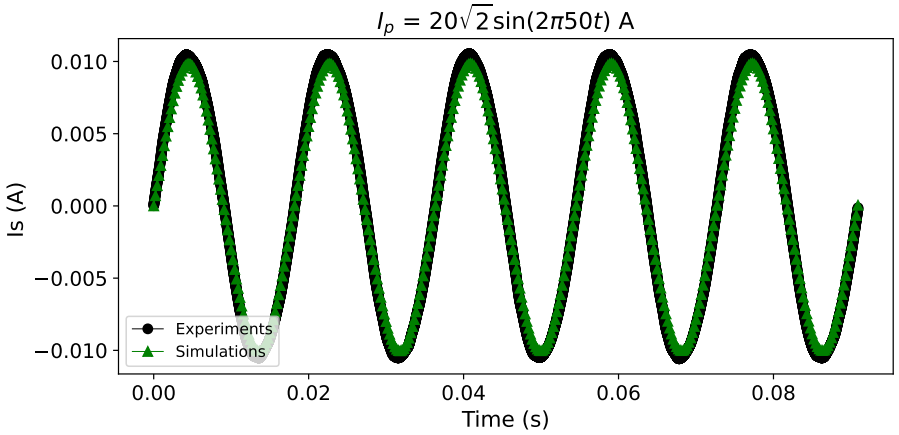

Figure IV.12: Current through the secondary coil for $I_p = 20\sqrt{2}\sin(2\pi 50t)$ A.

Let us remark that for the three cases, the first and second period show more difference between the experiments and the simulations, because the initialization of the simulations are not exact and they take two periods to stabilize. We also notice that the first two cases show linear behaviour of the material whereas the third case shows nonlinear behaviour. For the three cases, we see that the results obtained with the experiments and simulations are fairly close. To explain the low difference between experiments and simulations we can enumerate the model differences given by:

- The material is modeled with the curve shown in Figure IV.7. This curve has been

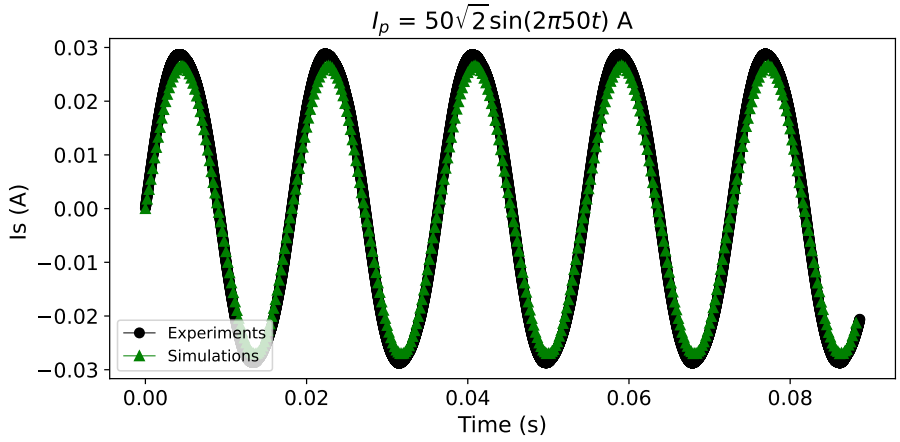

Figure IV.13: Current through the secondary coil for $I_p = 50\sqrt{2}\sin(2\pi 50t)$ A.

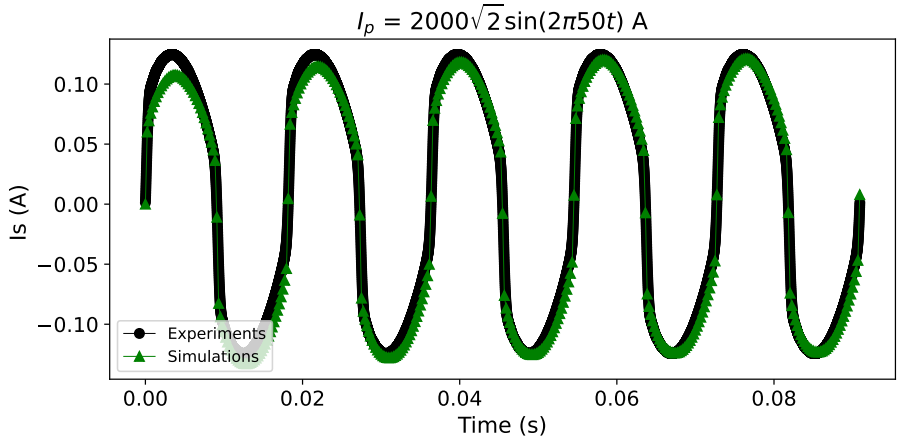

Figure IV.14: Current through the secondary coil for $I_p = 2000\sqrt{2}\sin(2\pi 50t)$ A.

obtained with measures on the material and a later manual calibration. The initial measures are not fully smooth and this curve probably does not fully describe the behaviour of the real material.

- The simulation model considers a massive material whereas experiments are made with sheets.
- The simulations geometry of the current transformer core is simplified, avoiding sharp edges and omitting some geometry details, as shown in Figure IV.10.
- The experiments use measuring devices that have errors: the current sensor that verifies the current in the primary conductor (I_p) might have an error up to 1%.

Given these differences and the results graphs, we conclude that the simulation model is validated.

Finally, in terms of computation time, the first two simulation cases take around 11 hours whereas the nonlinear case takes 15 days. Let us note that the simulation chosen is

challenging: time stepping regime, presence of air gaps, nonlinear behaviour of the material defined by splines and field-circuit coupling with the resistance linked to the secondary coil. These are the reasons why the simulation time is considerable.

IV.4 Rogowski metering coil: off-centre study

When the Rogowski metering coil principle was presented in chapter 1, there was a list of requirements needed to have a robust sensor. Two of them were the off-centre and the crosstalk. This section and the following one study these two aspects.

If we consider the ideal case when the Rogowski metering coil is alone and its manufacturing is perfect, without any defects, the off-centre of the primary conductor or of the Rogowski metering coil won't change the result. Nevertheless, given that it is placed next to the current transformer, the current transformer will amplify the possible manufacturing defects that occur in the Rogowski. It is in that case that it might become sensitive to the off-centre of the coil itself or of the primary conductor.

Then, we decided to study the effect of shifting the Rogowski metering coil in its flux computation. To do that, we suppose that the rest of the elements remain still (the current transformer, primary conductor, secondary coil) and only the Rogowski metering coil shifts a maximum of 1 mm, which is realistic from an industrial point of view. We suppose that the shift can only be given in the X and Y direction, omitting a Z shift. We define four different scenarios:

1. The shift is given in the X direction while Y is fixed.
2. The shift is given in the Y direction while X is fixed.
3. The shift is given in the X and Y direction simultaneously with the same value for each direction.
4. The shift is given in the X and Y direction simultaneously with opposite value for each direction.

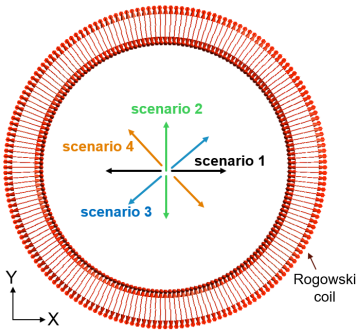

We define a shift interval of 0.2 mm, meaning that we will compute the cases $\{-1, -0.8, -0.6, -0.4, -0.2, 0, +0.2, +0.4, +0.6, +0.8, +1\}$ mm, for instance Figure IV.15 shows an off-centre in the X axis of $+1$ mm and an off-centre in the Y axis of $+1$ mm. The material considered is the nonlinear one defined with the magnetization curve of Figure IV.7.

The simulation model used for this section employs the magnetostatic formulation shown in chapter 2 with the thin air gap model. The geometry is modeled with a mesh of 8700 volume elements as in Figure IV.15. The current imposed on the primary conductor is $20\sqrt{2}$ and the output will be the flux through each of the 180 coils, being the total flux of the Rogowski coil the sum of the 180 coils. This computation is done for each off-centre position, comparing them with the value obtained without an off-centre, with the following expression:

$$\text{relative difference} = \text{abs}\left(\frac{\text{OffCentreValue} - \text{CentreValue}}{\text{CentreValue}}\right) \cdot 100,$$

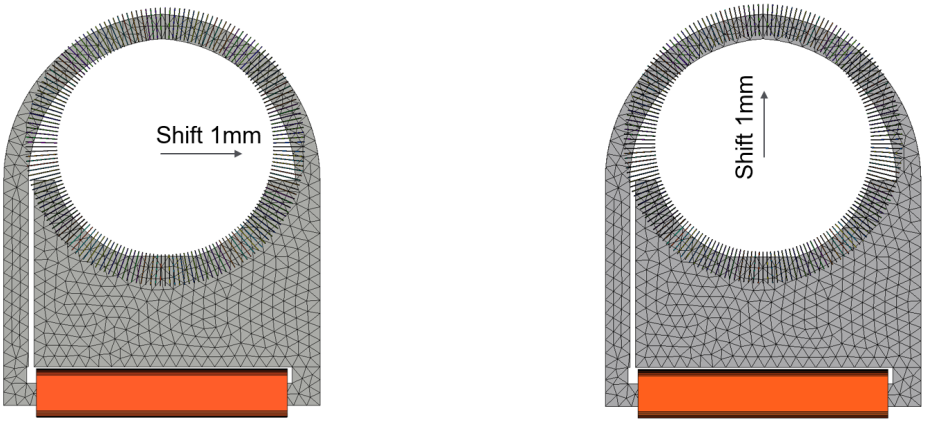

(a) Off-centre X direction 1mm. (b) Off-centre Y direction 1mm.

Figure IV.15: Off-centre of the Rogowski metering coil.

expressed in percentage value, where abs is the absolute value.

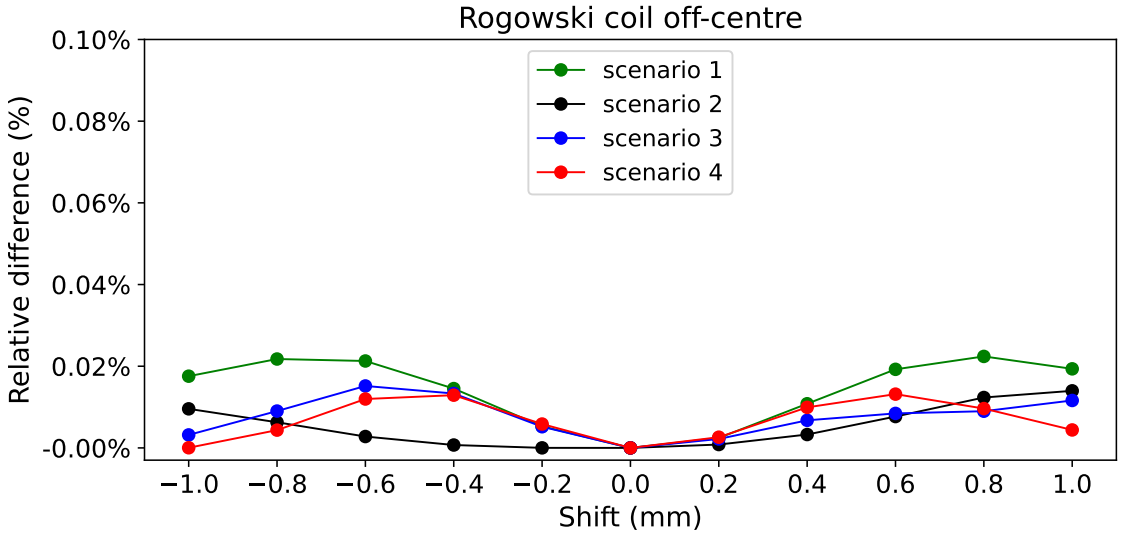

Figure IV.16: Rogowski coil off-centre results

The relative difference obtained for each scenario is given in Figure IV.16. First, we notice that the values are not fully symmetric (for instance scenario 3) because the geometry of the current transformer is not symmetric. We also notice that the highest values are given for scenario 1, in which there is an off-centre along the X axis. The highest relative difference is given for a shift of -0.8 and 0.8 mm. The lowest values are given for scenario 2. Scenarios 3 and 4 are quite similar and they follow the same pattern for negative values: the relative difference increases up to a shift of 0.6 mm and then it decreases, having a very low relative difference for an off-centre of -1 mm.

In any case, the relative difference is always inferior to 0.1 %, which is low with respect to the potential errors of the model.

The same procedure has been done for the nonlinear case, imposing on the primary conductor $2000\sqrt{2}$ A. In this case, the relative difference for each scenario is extremely low, always inferior to 0.001 %, which occurs because the current transformer is saturated.

We conclude that an off-centre along X axis has more decentering error than Y axis one, but for the four scenarios the values are very low, always inferior to 0.1 % for an off-centre lower than 1 mm. Then, the model of Rogowski metering coil of Masterpact MTZ circuit breaker is robust in terms of off-centre.

IV.5 Crosstalk study

Another requirement of a robust Rogowski metering coil is to have low crosstalk. In general, the crosstalk is defined as the presence of other undesired signals on a system. In our specific case, given that there are three current sensors out of phase with a shift of 120 degrees, the crosstalk is produced among the primary conductors of the three sensors. Then, given the three current sensors, the aim of this section is to study the effect of a primary conductor of a current sensor on the Rogowski metering coil of another sensor. Figure IV.17d shows the three sensors with the current transformer each and only one Rogowski metering coil on the current sensor that is placed at the center. Let us note that the distance between two current sensors is 11.5 cm.

We focus on analysing the effect of the primary conductor of the left disturber and the right disturber on the Rogowski coil placed in the middle sensor. To do that, we will consider four different scenarios, being each of them representative of an industrial case. The geometry of each scenario is the following:

1. The current sensor placed in the middle is complete, with the current transformer core, the primary conductor, the secondary coil and the Rogowski metering coil. The left and right disturber have the current transformer core and the secondary coil, but no primary conductor.

2. The current sensor placed in the middle is complete. The left and right disturber have the current transformer core and the secondary coil. The left disturber also has the primary conductor, which is out of phase 180 degrees with respect to the primary conductor of the middle current sensor.

3. Similar to the previous case but instead of considering the primary conductor of the left disturber we consider the primary conductor of the right disturber, also out of phase 180 degrees.

4. The current sensor placed in the middle is complete. The left and right disturber have the current transformer core, the primary conductor and the secondary coil. The three primary conductors are out of phase 120 degrees.

Figure IV.17 shows these four scenarios.

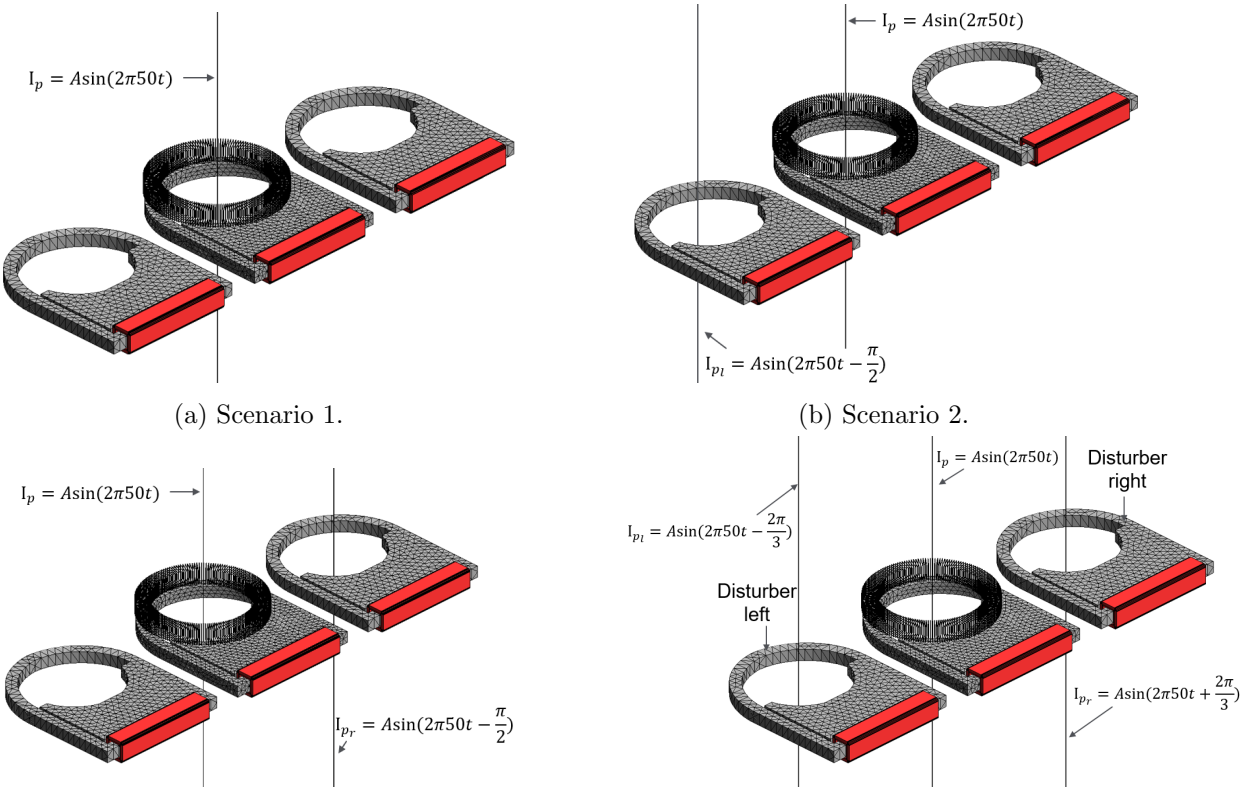

(a) Scenario 1. (b) Scenario 2.

(c) Scenario 3. (d) Scenario 4.

Figure IV.17: Scenarios to obtain the crosstalk.

The procedure to compute the crosstalk is the following:

- A time stepping simulation of scenario 1 is considered. We compute the flux through each of the 180 coils defining the Rogowski metering coil. Then, the discrete root mean square (rms) value of each coil with:

$$\Phi_{c_{rms}} = \sqrt{\frac{1}{T}\sum_{t}\Phi_{c_t}^2} \tag{IV.1}$$

  where T is the period, and Φ_{c_t} is the flux of coil c at time t. This root mean square value provides a good insight of the flux seen by a coil in transient case. We sum the rms value of the 180 coils to obtain the reference value.

- The same process is repeated for scenarios 2, 3 and 4, running a time stepping formulation considering the left, right or left and right disturber primary conductors respectively. Again, the computation of the flux through each of the 180 coils of the middle Rogowski coil is done and their rms value obtained. The addition of the 180 coils rms values provides a single flux value for each scenario, which is the flux of the whole Rogowski coil.

- Scenarios 2, 3 and 4 are compared with scenario 1 computing the relative difference as:

$$\frac{\text{valueScenario}_\text{i} - \text{valueScenario}_1}{\text{valueScenario}_1},$$

for $i = 2, 3, 4$ obtaining a value for each comparison, which we call crosstalk.

The time stepping formulation considered has three periods and frequency $f = 50$ Hz, therefore $t \in [0, 0.06]$, with 40 time steps per period. The rms value is computed with the data of the third period. We again consider three different currents that will be imposed on the primary conductors with $\mathrm{I}_p = A\sin(2\pi 50t)$ for $A = 20\sqrt{2}, 50\sqrt{2}$ and $2000\sqrt{2}$. We remind that the material is nonlinear following the magnetization curve of Figure IV.7.

The crosstalk values obtained for each scenario 2, 3 and 4 (that are compared with the referece value of scenario 1) and for each current are presented in Figure IV.18. The maximum value accepted to have a sensor with low crosstalk is 1 % and the scale is deliberately set to a maximum of 0.5 % (half of the maximum value accepted) to show that the results are very low.

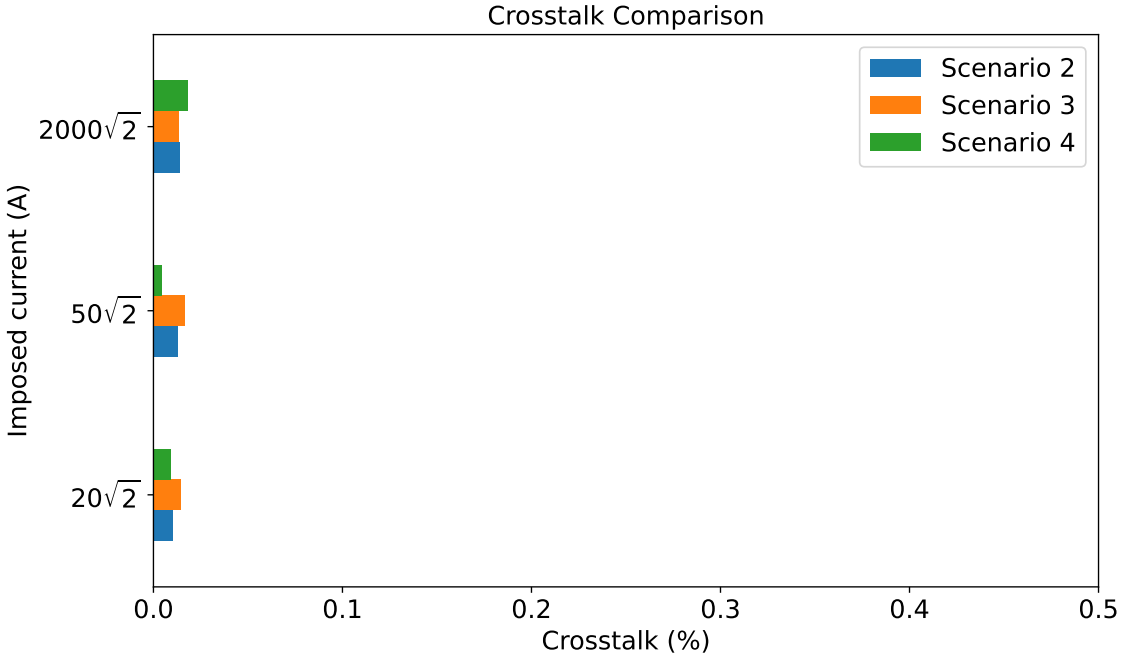

Figure IV.18: Crosstalk values.

Indeed, the results are not only inferior to 1 %, but also lower than 0.1 %, which ensures that the primary conductors of the three sensors don't interfere with each other. They show that the model is accurate, and it could be used in the future to provide the crosstalk that occurs if there is a defect in the coil, such as missing one turn of the coil at a given position, or having a different coil density on a given part of the coil.

Let us note that these results couldn't have been found using the FEM given the large air region that has to be modeled between the Rogowski coil and the CT of each sensor and also between the 3 sensors. This section corroborates the robustness of the Rogowski metering sensor in the presence of the current transformer that is inside Masterpact MTZ circuit breaker.

IV.6 Conclusion

In this chapter we have shown an application case of the current sensor of Masterpact MTZ circuit breaker, which is formed by a current transformer and a classic Rogowski metering coil. The aim is to have an accurate model to increase the robustness of the current sensor with simulations that use the formulations developed in chapter 2 and chapter 3. Moreover, we want to exhibit that these formulations are not just theoretical, but they can also be used to simulate real life sensors while obtaining accurate results.

We have explained the manufacturing challenges of this sensor, especially the ones regarding the winding process of the Rogowski metering coil and the fact that the current transformer might affect to its metering function. We then proposed to analyse three features, each of them constitutes a section.

The first one is a validation of the current transformer model with experiments, which ensures that the simulation model indeed represents the current sensor. The results are successful, showing that the model stands for the real sensor. There is a small difference between the simulations and the experiments, which is given by the simplification of the model, mainly due to the consideration of a massive core instead of sheets and the simplification of the geometry.

The second and third features are part of the Rogowski coil requirements to be robust. The simulations are done not only with the Rogowski coil but also with the current transformer next to it, which affects its behaviour. These features are the off-centre of the Rogowski coil and the crosstalk. Regarding the off-centre, we have studied a shift of up to 1 mm of the Rogowski coil, which is the maximum reasonable shift that could occur with these sensors. The results obtained show a relative difference inferior to 0.1 % comparing it with the neutral position, which is low. For the crosstalk, we have analysed different scenarios for three sensors that are placed next to each other, perceiving the effect of a primary conductor of one of these sensors on the others. The crosstalk value obtained is inferior to 0.1 % for all the cases, meaning that the results are in line with the 1 % threshold that we aim at having, and they show a very good immunity of the sensor. Now, further simulations could be done in the future to obtain the crosstalk is there are some defects that occur on the Rogowski metering coil, such as having different coil density in some specific areas.

Let us note that the latter two elements studied have been carried out with a model that represents the Rogowski metering coil with 180 turns and these turns are perfectly placed in ideal conditions (uniform winding density, no turns sliding over the others...). Nevertheless, in real life the winding is not perfect and an analysis of the possible defects could be done with this model, obtaining the off-centre and the crosstalk for a given defect. Some examples of realistic defects could be the effect of a turn missing in a specific region of the Rogowski coil, the misplacement of them or a different coil density in some parts of the coil. Quantifying these effects would allow to have more information of the Rogowski behaviour. We also remark that the simulation model has 180 turns as opposed

to 1600 turns of the real Rogowski coil, therefore a more complete simulation model could be considered, but it would definitely increase the computation time.

These simulations could not have been done without the volume integral method formulations, that allow to obtain accurate results on the Rogowski metering coil. Indeed, in the past some initiatives to model the sensor using the FEM conducted to vague results that had high numerical noise and weren't accurate. This is due to the very thin mesh that the finite element method needs to model all the air region around the Rogowski metering coil, which is not needed for the volume integral method.

Conclusion and perspectives

This thesis is focused on the development of modeling tools that allow to have simulations of current sensors. The current sensors targeted are placed in circuit breakers, and their aim is to ensure the metering function (high accuracy), the protection (fast response) and to provide energy for other components (self-powered).

The modeling tool contemplated in this thesis is the use of the volume integral method. This choice is made to have high accuracy in the computation of magnitudes through coils that are placed in the air, not surrounded by a magnetic material, given that this method does not need to mesh the air, and in particular, the air around these coils. Nevertheless, part of the difficulty of this thesis is to make sure that, apart from the expected improvement of this method with respect to others, the rest of the elements of the sensor can also be modeled. These elements are, among others: presence of thin air gaps, non linearity of the material, field-circuit coupling...

This thesis is divided in four chapters. The first one explains the context and the challenges of modeling current sensors. We start explaining the main functionalities of a current sensor and the different types that exist to after narrow them down to the current sensors that are placed inside circuit breakers. These sensors are formed of two parts: a current transformer, which will provide the power to the circuit breaker and a Rogowski coil that will ensure the metering and protection functions. Once the current sensors are introduced, we explain the interest in having simulation tools that allow to model these current sensors on the computer. The classic method, the Finite Element Method is mentioned as it is very powerful in many cases, but the thin mesh needed around the Rogowski metering coil makes us choose a different method to model the desired current sensors: the Volume Integral Method. The latter method does not need to mesh the air, being the active regions the only ones that are discretized, which is the reason why it is a good competitor to provide more accurate results that the FEM. Finally, a list of objectives of the thesis is given, that can be summarised as: develop a volume integral formulation that allows to model current sensors with high accuracy in the computation of the magnetic flux, taking into account nonlinear materials, thin air gaps and the field-circuit coupling with a circuit that has lumped elements.

The second chapter explains a nonlinear magnetostatic volume integral formulation based on the discretization of induction $\mathbf{B}$ using facet-shape functions and a Galerkin projection to obtain a matrix system defining the problem [1]. The formulation is written

in an equivalent circuit approach to be able to solve the matrix system with a circuit solver. Furthermore, the extraction of the value of the induction at each point, including the points that are placed in the air, is explained, as well as the strategy used to compute the magnetic flux through coils. The second part of this chapter focuses on modeling thin air gaps, which are common features that appear when welding two parts of the current transformer core. The thin air gap region is considered as a surface region with a specific numerical treatment instead of a volume region. This allows to obtain accurate results avoiding imprecision in the computation of certain integrals and skipping a thin mesh of the air gap volume that could lead to very large matrix systems. An application of the formulation and the thin air gap model to NSX sensor is shown, obtaining accurate results and validating them.

The third chapter describes two time stepping volume integral formulations for field-circuit coupled problems, which are developed for nonlinear non conductive materials. They are an extension of the magnetostatic regime shown in chapter 2. The first one is a weak formulation, which treats the magnetic field and the circuit as separate systems in the time stepping process. Two algorithms, one for linear and another one for nonlinear materials are explained, and they are restricted to the topology of the problem explained (external circuit composed of a coil connected to a resistance). The second formulation presented is called strong field-circuit coupling, and it writes the equations describing the magnetic field and the circuit together to create a matrix system. This matrix system is again written in an equivalent circuit form to obtain a solution with a circuit solver. Two important characteristics are that the time stepping method uses a theta scheme and nonlinear materials are treated with the Newton-Raphson method. In this case, the topology of the problem considered is more flexible, being able to introduce more elements in the external circuit, such as current sources, voltage sources or capacitors. Both formulations, the weak and the strong coupling are validated with NSX sensor, comparing the results to the ones obtained with FEM. We found that the two formulations have similar accuracy, therefore, if the problem that we are treating has the topology considered in the weak field-circuit case and it is linear, we encourage to use it, given that it provides faster results. Otherwise, the strong field-circuit coupling should be chosen.
In the future, the weak field-circuit coupling formulation could be developed further to include more elements in the external circuit. Regarding the strong field-circuit coupling, the time stepping technique could be done with a different scheme to reduce the computation time. For instance, an adaptive time step could be considered with a predictor corrector method. Model order reduction techniques could also be developed in order to speed up the computation time. However, the treatment of the non-linearity would certainly be challenging.
Furthermore, the formulations could be extended to deal with conductive materials. This would allow to quantify eddy currents that occur on the current transformer. Initially it could be done for massive materials and then it could be adjusted to model sheets, as it is the case of the current transformer cores that we usually consider.

Finally, the fourth chapter is a true industrial application of the formulations developed in chapter 2 and chapter 3 to evidence that they are able provide a model that corrob-

orates the robustness of the sensors. The sensor chosen for this application is placed in Masterpact MTZ circuit breaker and it is composed of a current transformer and a classic Rogowski metering coil. The most sensitive part is the Rogowski metering coil, because it can be perturbed by the presence of the current transformer, whereas the current transformer is not perturbed by the Rogowski. For the robustness of the Rogowski metering coil, we study the off-centre and the crosstalk, obtaining very low results that corroborate the reliability of the sensor. Furthermore, to show that the simulation model reflects well the real one, we have compared experimental data of the current transformer with simulation data to demonstrate that the simulations done are an accurate representation of the current sensor. Nevertheless, the model of the Rogowski metering coil is made with 180 turns, which is different to the 1600 turns of the real one. In the future, the model could be refined to consider all the turns, which will be more time consuming but also more accurate for features such as the crosstalk. Moreover, the simulations shown in chapter 4 are in ideal conditions in which the Rogowski metering coil does not have any defect and the turns are perfectly placed. In order to further information about the behaviour of the Rogowski metering coil, other situations could be simulated, considering defects on the coil, such as a non uniform winding density.

We conclude that the volume integral formulations developed allow to model the current sensors of interest that are embedded in a circuit breaker and composed of a current transformer and a Rogowski metering coil, taking into account thin air gaps, nonlinear materials and field-circuit coupling.

Bibliography

[1] Le-Van, V., Meunier, G., Chadebec, O., & Guichon, J. M. (2015). A volume integral formulation based on facet elements for nonlinear magnetostatic problems. *IEEE Transactions on Magnetics, 51*(7), 1-6.

[2] Xiao, C., Zhao, L., Asada, T., Odendaal, W. G., & van Wyk, J. D. (2003). An overview of integratable current sensor technologies. *38th IAS Annual Meeting on Conference Record of the Industry Applications Conference Salt Lake City, UT, USA, 2*, 1251-1258.

[3] Ripka, P. (2010). Electric current sensors: a review. *Measurement Science and Technology, 21*(11), 112001.

[4] Samimi, M. H., Mahari, A., Farahnakian, M. A., & Mohseni, H. (2015). The Rogowski Coil Principles and Applications: A Review. *IEEE Sensors Journal, 15,* (2), 651-658.

[5] Ziegler, S., Woodward, R., Iu, H., & Borle, L. (2009). Current Sensing Techniques: A Review. *IEEE Sensors Journal, 9*(4), 354-376.

[6] Ramboz, J. D. (1996). Machinable Rogowski coil, design, and calibration. *IEEE Transactions on Instrumentation and Measurement, 45*,(2), 511-515.

[7] Wu, W., Xu, Y., Yang, S., Lu, S., & Xia, X. (2016). Research on Proximity Magnetic Field Influence in Measuring Error of Active Electronic Current Transformers. *MATEC Web of Conferences, 59,* 01010.

[8] Hrennikoff, A. (1941). Solution of problems of elasticity by the framework method.

[9] Courant, R. (1943). Variational methods for the solution of problems of equilibrium and vibrations. *Bulletin of the American Mathematical Society, 49*(1), 1-23.

[10] Harrington, R. F. (1993). Field Computations by Mount Methods.

[11] Newman, M. J., Trowbridge, C. W., & Turner, L. R. (1972). GFUN: An interactive program as an aid to magnet design.

[12] Elleaume, P., Chubar, O., & Chavanne, J. (1997). Computing 3D magnetic fields from insertion devices. *Proceedings of the 1997 Particle Accelerator Conference, 3,* 3509-3511.

[13] Liang, J., & Subramaniam, S. (1997). Computation of molecular electrostatics with boundary element methods. *Biophysical journal, 73*(4), 1830-1841.

[14] Nguyen, T. -T. , Meunier, G., Guichon, J. -M., Chadebec, O., & Nguyen, T. -S. (2014). An integral formulation for the computation of 3-D eddy current using facet elements. *IEEE Transactions on Magnetics, 50*(2), 549-552.

[15] Greengard, L., & Rokhlin, V. (1987). A fast algorithm for particle simulations. *Journal of computational physics, 73*(2), 325-348.

[16] Le-Van, V., Bannwarth, B., Carpentier, A., Chadebec, O., Guichon, J. M., & Meunier, G. (2014). The adaptive cross approximation technique for a volume integral equation method applied to nonlinear magnetostatic problems. *IEEE transactions on magnetics, 50*(2), 445-448.

[17] Bebendorf, M., & Rjasanow, S. (2003). Adaptive low-rank approximation of collocation matrices. *Computing*, 70, 1-24.

[18] Borm, S., & Grasedyck, L. (2005). Hybrid cross approximation of integral operators. *Numerische Mathematik, 101,* 221-249.

[19] Carpentier, A., Chadebec, O., Galopin, N., Meunier G., & Bannwarth, B. (2013). Resolution of nonlinear magnetostatic problems with a volume integral method using the magnetic scalar potential. *IEEE transactions on magnetics, 49*(5), 1685–1688.

[20] Canova, A., & Repetto, M. (2001). Integral solution of nonlinear magnetostatic field problems. *IEEE transactions on magnetics, 37*(3), 1070-1077.

[21] Le Van, V. (2015). *Développement de formulations intégrales de volume en magnétostatique* [Doctoral dissertation, Université Grenoble Alpes].

[22] Le-Van, V., Meunier, G. , Chadebec, O., & Guichon, J. -M. (2016). A Magnetic Vector Potential Volume Integral Formulation for Nonlinear Magnetostatic Problems. *IEEE Transactions on Magnetics, 52* (3), 1-4.

[23] Chadebec, O., Coulomb, J. -L., & F. Janet. (2006). A review of magnetostatic moment method, *IEEE Transactions on Magnetics, 42*(4), 515-520.

[24] Neagoe, C., & Ossart, F. (1994). Analysis of convergence in nonlinear magnetostatic finite elements problems. *IEEE Transactions on Magnetics, 30*(5), 2865-2868.

[25] Y. Gabi. (2012). *Modélisation FEM du système de contrôle non destructif 3MA en ligne de production des aciers dual phase.* [Doctoral dissertation, Université Grenoble Alpes], 105-106.

[26] Canova, A., & Repetto, M. (2001). Integral solution of nonlinear magnetostatic field problems. *IEEE Transactions on Magnetics, 37*(3), 1070-1077.

[27] Han, L., Tong, L.-S., & Yang, J. (1994). Integral equation method using total scalar potential for the simulation of linear or nonlinear 3D magnetostatic field with open boundary. *IEEE Transactions on Magnetics, 30*(5), 2897-2900.

[28] Vuillermet, Y., Chadebec, O., Coulomb, J. L., Rouve, L. L., Cauffet, G., Bongiraud, J. P., & Demilier, L. (2008). Scalar potential formulation and inverse problem applied to thin magnetic sheets. *IEEE transactions on magnetics, 44*(6), 1054-1057.

[29] Balasubramanian, S., Lalgudi, S. N., & Shanker, B. (2002). Fast-integral-equation scheme for computing magnetostatic fields in nonlinear media. *IEEE transactions on magnetics, 38*(5), 3426-3432.

[30] Altair Engineering, "Altair Flux^{TM}", 2021. [Online]. Available on: https://www.altair.com/flux/

[31] Nakata, T., Takahashi, N., Fujiwara, K., & Shiraki, Y. (1990). 3D magnetic field analysis using special elements. *IEEE Transactions on Magnetics, 26*(5), 2379-2381.

[32] Guerin, C., Tanneau, G., Meunier, G., Brunotte, X., & Albertini, J. B. (1994). Three dimensional magnetostatic finite elements for gaps and iron shells using magnetic scalar potentials. *IEEE transactions on magnetics, 30*(5), 2885-2888.

[33] Ospina, A., Santandrea, L., Le Bihan, Y., & Marchand, C. (2010). Modeling of thin structures in eddy current testing with shell elements. *The European Physical Journal-Applied Physics, 52*(2), 23308.

[34] Bossavit, A. (1988). Whitney forms: A class of finite elements for three-dimensional computations in electromagnetism. *IEE Proceedings A (Physical Science, Measurement and Instrumentation, Management and Education, Reviews), 135*(8), 493-500.

[35] Morandi, A. , Fabbri, M., & Ribani, P. L. (2010). A Modified Formulation of the Volume Integral Equations Method for 3-D Magnetostatics. *IEEE Transactions on Magnetics, 46*(11), 3848-3859.

[36] Meunier, G., Chadebec, O., Guichon, J.-M., Le-Van, V., Siau, J., Bannwarth, B., & Sirois, F. (2016). A-T Volume Integral Formulations for Solving Electromagnetic Problems in the Frequency Domain. *IEEE Transactions on Magnetics, 52*(3), 1-4.

[37] Mumps Technologies SAS. (2023) MUMPS. [Online]. Available: https://mumps-solver.org/index.php

[38] Nguyen, T-S, Guichon, J. M., Chadebec, O., Meunier, G., & Vincent B. (2012). An Independent Loops Search Algorithm for Solving Inductive Peec Large Problems. *Progress In Electromagnetics Research M* (23), 53-63.

[39] Trung Son Nguyen. (2012). *Réduction de modèles issus de la méthode PEEC pour la modélisation électromagnétique des interconnexions électriques.* [Doctoral dissertation, Université Grenoble Alpes], 20-30.

[40] Fabbri, M. (2008). Magnetic Flux Density and Vector Potential of Uniform Polyhedral Sources. *IEEE Transactions on Magnetics, 44*(1), 32-36.

[41] Fabbri, M. (2009). Magnetic flux density and vector potential of linear polyhedral sources, COMPEL. *The international journal for computation and mathematics in electrical and electronic engineering, 28*(6), 1688-1700.

[42] Huang, L., Meunier, G., Chadebec, O., Guichon, J. M., Li, Y., & He, Z. (2017). General integral formulation of magnetic flux computation and its application to inductive power transfer system. *IEEE Transactions on Magnetics, 53*(6), 1-4.

[43] Urankar, L. (1980). Vector potential and magnetic field of current-carrying finite arc segment in analytical form, Part I: Filament approximation. *IEEE Transactions on Magnetics, 16*(5), 1283-1288.

[44] Urankar, L. (1982). Vector potential and magnetic field of current-carrying finite arc segment in analytical form, Part II: Thin sheet approximation. *IEEE Transactions on Magnetics, 18*(3), 911-917.

[45] Urankar, L. (1982). Vector potential and magnetic field of current-carrying finite arc segment in analytical form, Part III: Exact computation for rectangular cross. *IEEE Transactions on Magnetics, 18*(6), 1860-1867.

[46] Nguyen, T. T., Meunier, G., Guichon, J. M., Chadebec, O., & Nguyen, T. S. (2014). An integral formulation for the computation of 3-D eddy current using facet elements. *IEEE transactions on magnetics, 50*(2), 549-552.

[47] Kettunen, L., & Turner, L. R. (1992). A volume integral formulation for nonlinear magnetostatics and eddy currents using edge elements. *IEEE transactions on magnetics, 28*(2), 1639-1642.

[48] Alayeto, M. H., Meunier, G., Rondot, L., Chadebec, L., Favre, M., & Guichon, J.-M. (2023). An Air Gap Model for Magnetostatic Volume Integral Formulation. *IEEE Transactions on Magnetics, 59*(5), 1-4.

[49] Crank, J., & Nicolson, P. (1947). A practical method for numerical evaluation of solutions of partial differential equations of the heat-conduction type. *Mathematical Proceedings of the Cambridge Philosophical Society, 43*(1), 50-67.

[50] Farago, I. (2013). Convergence and stability constant of the theta-method. *Applications of Mathematics 2013*, 42-51.

[51] Ruehli, A. E. (1972). Inductance Calculations in a Complex Integrated Circuit Environment. *IBM Journal of Research and Development, 16*(5), 470-481.

[52] Meunier, G. , Chadebec, O., & Guichon, J. -M. (2015). A Magnetic Flux–Electric Current Volume Integral Formulation Based on Facet Elements for Solving Electromagnetic Problems. *IEEE Transactions on Magnetics, 51*(3), 1-4.

[53] De Grève, Z., Siau, J., Meunier, G., Guichon, J. -M., & Chadebec, O. (2016). A Mixed Surface Volume Integral Formulation for the Modeling of High-Frequency Coreless Inductors. *IEEE Transactions on Magnetics, 52*(3), 1-4.

[54] Nguyen, T. -T., Meunier, G., Guichon, J. -M., & Chadebec, O. (2015). 3-D Integral Formulation Using Facet Elements for Thin Conductive Shells Coupled With an External Circuit. *IEEE Transactions on Magnetics, 51*(3), 1-4.

[55] Alotto, P., Desideri, D., Freschi, F., Maschio, A., & Repetto, M. (2011). Dual-PEEC Modeling of a Two-Port TEM Cell for VHF Applications. *IEEE Transactions on Magnetics, 47*(5), 1486-1489.

[56] Siau, J. , Meunier, G., Chadebec, O., Guichon, J. -M., & Perrin-Bit, R. (2016). Volume integral formulation using face elements for electromagnetic problem considering conductors and dielectrics. *IEEE Trans. Electromagn. Compat., 58*(5), 1587–1594.

[57] Torchio, R. , Moro, F., Meunier, G., Guichon, J. -M., & Chadebec, O. (2019). An extension of unstructured-PEEC method to magnetic media. *IEEE Trans. Magn., 55*(6), 1–4.

[58] Blattner Martinho, L., Siau, J., Bannwarth, B., Guichon, J. -M., Chadebec, O., Meunier, G., & Silva, V. C. (2016). Generalized PEEC analysis of inductive coupling phenomena in a transmission line right-of-way. *IEEE Transactions on Magnetics, 52*(3), pp. 1-4, 9401004.

[59] Vassent, E., Meunier, G., Foggia, A., & Reyne, G. (1991). Simulation of induction machine operation using a step by step finite element method coupled with circuits and mechanical equations. *IEEE Transactions on Magnetics, 27*(6), 5232-5234.

[60] Yan, S., & Jin ,J.-M. (2015). Theoretical formulation of a time-domain finite element method for nonlinear magnetic problems in three dimensions (Invited Paper). *Progress In Electromagnetics Research, 153*, 33-55.

[61] Tsukerman, I. A., Konrad, A., & Lavers, J. D. (1992). A method for circuit connections in time-dependent eddy current problems. *IEEE Transactions on Magnetics, vol. 28*(2), 1299-1302.

[62] Shen, D., Meunier, G., Coulomb, J., & Sabonnadiere, J. (1985). Solution of magnetic fields and electrical circuits combined problems. *IEEE Transactions on Magnetics, 21*(6), 2288-2291.

[63] Nocedal, J., & Wright, S. J. (1999). Line Search Methods. *Numerical Optimization. New York: Springer,* pp. 34-63.

[64] Meunier, G. (Ed.). (2010). The finite element method for electromagnetic modeling.

Publications

International articles

IEEE transactions on Magnetics	*An Air Gap Model for Magnetostatic Volume Integral Formulation* M. H. Alayeto, G. Meunier, L. Rondot, O. Chadebec, M. Favre and J. -M. Guichon - Vol. 59, no. 5, pp. 1-4. **May 2023**.

Abstract: *The presence of air gaps in magnetic modeling problems is well known. When the air gap is thin, its numerical treatment is complex because the integrals arising on the model lead to inaccuracy. This article presents an air gap model for thin air gaps using the magnetostatic volume integral method (VIM) for linear and nonlinear problems. The thin air gap is considered as a face region with a numerical treatment to improve the accuracy. An application to an academic case and a current transformer is reported to validate the model*

TO BE PUBLISHED

IEEE transactions on Magnetics	*A Time-Stepping Volume Integral Formulation for Nonlinear Field-Circuit Coupled Problems* M. H. Alayeto, G. Meunier, L. Rondot, O. Chadebec, M. Favre and J. -M. Guichon - **August 2023**.

Abstract: *A B-conforming time-stepping Volume Integral Method (VIM) formulation for nonlinear 3D field-circuit coupled problems is presented in this paper. The advantage of the VIM with respect to the Finite Element Method (FEM) is that only the ferromagnetic regions have to be discretized, thus avoiding to mesh the air. It is an appealing approach given that it avoids numerical errors that can arise from meshing the air. A direct formulation is explained, assembling in a system the magnetic field and the circuit contributions when coils are present. An application to a current transformer is shown, comparing it to the FEM to validate its accuracy.*

Méthode integral de volume pour la modelisation électromagnetique des capteurs de courant autonomes.

Résumé Cette thèse présente le développement de la méthode intégrale de volume pour modéliser les capteurs de courant de Schneider Electric contenus dans un disjoncteur. Ces capteurs sont composés de deux parties : un transformateur de courant (auto-alimentation) et une bobine de mesure Rogowski (précision). La conception de ces capteurs de courant n'est pas simple, et l'utilisation de la modélisation comme outil qui aide à leur développement et robustesse est avantageuse.
Le transformateur de courant seul peut être modélisé avec la méthode des éléments finis (FEM). Néanmoins, la modélisation de la bobine de mesure Rogowski isolée a besoin d'un maillage très fin de l'ait autours. Également, lorsque les deux capteurs sont ensemble un maillage très fin de l'air autours le Rogowsi et entre le transformateur de courant et le Rogowski est nécessaire, étant donné que le transformateur de courant perturbe la bobine de Rogowski. Pour cette raison, nous avons choisi la méthode intégrale de volume (VIM), qui contrairement à FEM, n'a pas besoin d'une discrétisation de l'air.
Cette thèse présente une formulation magnétostatique et deux formulations transitoires avec la présence des entrefers fins en utilisant VIM. Une application au capteur de courant du disjoncteur MTZ Masterpact est exposé, montrant la précision des formulations développées.

Mots clés *Méthode integral de volume, couplage champ magnétique-circuit, entrefer fin, capteurs de courant, mesure, autonome, formulation, magnetostatique, magnetotransitoire.*

Volume integral method for electromagnetic modeling of self-powered current sensors.

Abstract This thesis presents the development of volume integral formulations to model Schneider Electric current sensors that are embedded in a circuit breaker. These current sensors are composed of two parts: a current transformer (self-power) and a Rogowski metering coil (accuracy). The design of these current sensors is not straightforward, and simulation models are useful tools to help to their conception and robustness.
The current transformer alone can be modeled with the Finite Element Method (FEM). Nevertheless, the Rogowski metering coil isolated needs a very thin mesh to be modelled. Similarly, when both parts of the sensor are together, a thin mesh of the air around the Rogowski coil and between them is needed, given that the current transformer perturbs the Rogowski coil. For this reason, we choose the Volume Integral Method (VIM) to model these sensors, which does not need to mesh the air.
This thesis presents a magnetostatic formulation and two time-stepping formulations with the presence of thin air gaps using the VIM. An application to the current sensor of MTZ Masterpact circuit breaker is exhibited, showing their accuracy.

Keywords *Volume integral method, modeling, magnetic field-circuit coupling, thin air gap, current sensors, metering, self-powered, Rogowski, current transformer, magnetostatic, time-stepping formulation.*